A NOVEL ANALYTICAL TEMPERATURE MODEL DEVELOPMENT FOR TURNING IN ORTHOGONAL AND OBLIQUE CONDITIONS INCLUDING THE EFFECTS OF ALL DEFORMATION ZONES AND TOOL WEAR

by

ZAHRA BARZEGAR OSGOUEI

Submitted to the Graduate School of Engineering and Natural Sciences
in partial fulfillment of
the requirements for the degree of Doctor of Philosophy

Sabancı University

July 2021

A Novel Analytical Temperature Model Development for Turning in Orthogonal and Oblique Conditions Including the Effects of All Deformation Zones and Tool Wear

APPROVED BY:

Approval Date: 13-July-2021

ABSTRACT

Modelling the temperature during machining and examining its effect on the workpiece and cutting tool is an important subject that has been researched for many years. The main purpose of modelling the temperature is to achieve increased tool life and surface quality. The tool wear which can affect the tool life and surface quality of the workpiece is significantly depended on the cutting temperature. Modeling the heat generation during the cutting processes such as orthogonal cutting, oblique cutting, and turning can be helpful for predicting the tool wear. This study introduces a novel model for the prediction of temperature in the cutting tool while the effects of all three deformation zones are considered. The proposed model considers the effect of cutting-edge radius and the third deformation zone for the first time in the literature in terms of temperature prediction using thermo-mechanical approach with dual-zone friction model. The material behavior is defined by the Johnson-Cook constitutive model. For the calculation of heat flux on the rake and flank faces, a dual-zone model was used. The temperature distributions at the tool-chip and tool-workpiece boundaries were determined analytically, and the temperature distribution inside the tool was calculated using the Finite Difference Method. The developed model was modified to include the effect of flank wear on the cutting temperature. The proposed models are verified experimentally and a good agreement is observed between the model predictions and the test results. This study also examined the effects of cutting-edge geometry and cutting conditions on cutting temperature, which can be used in optimized selection of cutting parameters and tool geometry in industrial applications.

Keywords: Machining, Cutting Process Modelling, Finite Difference Method, Temperature.

ÖZET

Talaşlı imalat sırasında sıcaklığın modellenmesi ile iş parçası ve kesici takım üzerindeki etkilerinin incelenmesi akademide uzun yıllardır araştırılan önemli bir konudur. Sıcaklığın ölçülmesinin temel amacı takım ömrünü ve yüzey kalitesini arttırmaktır. Takım ömrünü ve iş parçasının yüzey kalitesini etkileyebilecek takım aşınması, kesme sıcaklığına bağlıdır. Dik kesme, eğik kesme ve tornalama gibi talaşlı imalat operasyonları sırasında ortaya çıkan ısının modellenmesi, hem takım aşınmasının tahmininde hem de talaş davranışının hesaplanmasında yardımcı olabilir. Bu çalışmada sunulan analitik model sıcaklık dağılımı hesabında her üç deformasyon bölgesinin de etkilerini içermektedir.. Önerilen model literatürde ilk kez çift bölgeli sürtünme modeli ile termo-mekanik yaklaşım kullanarak kesici kenar yarıçapı ve üçüncü deformasyon bölgesinin etkisini sıcaklık tahmininde dikkate almaktadır. Çalışmada, malzeme davranışı Johnson-Cook malzeme modeli ile temsil edilmiştir. Takım serbest ve talaş yüzeylerindeki ısı akısının hesaplanması için çift sürtünme bölgeli bir model kullanılmıştır. Takım-talaş ve takım-iş parçası sınırlarındaki sıcaklık dağılımları analitik olarak belirlenmiş ve takım içi sıcaklık dağılımı Sonlu Farklar Metodu kullanılarak hesaplanmıştır. Geliştirilen model, aşınmanın kesme sıcaklığı üzerindeki etkisini de içerecek şekilde aşınmış takımlara da uyarlanmıştır. Önerilen model deneysel olarak doğrulanmıştır ve simülasyon ile test sonuçlarının uyumlu olduğu gözlemlenmiştir. Bu çalışmada, ayrıca kesme kenarı geometrisi ve kesme koşullarının kesme sıcaklığı üzerindeki etkileri incelenmiştir. Bu model kullanılarak kesme parametreleri ve takım geometrisinin en iyilenmesi sağlanabilir.

Anahtar Kelimeler: Talaşlı İmalat, Kesme Süreci Modellenmesi, Sonlu Farklar Metodu, Sıcaklık

ACKNOWLEDGEMENTS

I would like to express my deep gratitude to my research supervisor, Dr. Erhan Budak, for giving me the opportunity to do research and providing invaluable guidance not only throughout the research but also in my life. I would also like to thank Dr. Emre Özlü for his continued support and participation in this study. Without his encouragement in my hard times, doubtlessly, this thesis may have not been possible. I would also like to thank the members of my committee: Dr. Ali Koşar, Dr. Mustafa Bakkal, and Dr. Umut Karagüzel for their comments.

I owe my appreciation to a very special person, my best friend, my colleague, and my husband, Faraz, for his love, support, and understanding during my Ph.D. journey, which enabled me to complete my thesis. He were always there for me when I felt like I couldn't go on. I am grateful for his support and belief in me.

I was very lucky to join the MRL, and know the people there: Kaveh, Arash, Milad, Yaser, Esra, Hamid, Amin, Hayri, Mert, Mehmet, Samet, Gozde, Turgut, Mahzad and Saltuk. We had a great time with Faraz, Kaveh and Arash drinking coffee and discussing the technical, social, and political issues. Thanks Kaveh for offering chocolates and biscuits making it possible to continue working in the evenings.

I would like to thank the technicians of the MRL and Maxima people, Süleyman Tutkun, Ertuğrul Sadıkoğlu, Veli Nakşiler, Ahmet Ergen, and Dilara Albayrak. My especial thanks to Tayfun Kalender, who was always available for the quick preparations of the experimental setup. I learned a lot from Esma Baytok and we had funny times in micro-machining room of MRL, measuring hone radii with nano-focus microscope.

Having good friends around, made it easier to overcome the difficulties of Ph.D. journey. In the first days in Sabanci, I and Faraz had the opportunity to know Sina. I will always remember the good memories we made in the off-town festival and New Year eve. I cannot express how happy I was when Naeimeh and Arash joined us in Sabanci. I will never forget the taste of Lavangies and “expensive” Mahi-Sefids we ate with Amin. We watched many Bayern Munchen matches with Ali but the special and unforgettable one was the Bayern-Beşiktaş. I will miss all the good days we had together with Sahand, Vahid, Mohammadreza, Pegah, Navid, Mahsa, Meysam, Deniz, Yigit, Mehri and Ali. Thanks Sahar for being the “old but gold” friend. Getting her calls on Istanbul’s cloudy days made my days sunny. Although I am far from Roya, Parisa and Neda, I always have

them next to me, motivating and helping me. Thanks Mitra, Farshad, and Nastaran for their care and moral support during my hard days. Their home became a place we could play OK for hours and forget all the difficulties of those days. I am very lucky to have them.

At last but not the least, I am extremely grateful to my parents for their love and sacrifices throughout my life. My father, Jalil Barzegar, always supported me and respected my decisions. I wish he could have been here and I hope I have made him proud. My mother, Akram Talebi, always motivated me to continue my academic life. Her emotional supports and patience during my life especially in the last year helped me to overcome the difficulties. Her presence in Istanbul at a crucial time of my life, helped me find the strength to continue my work. My brother and my partner in crime, Ali, who is always there to help, encourage, support and make me laugh. Our discussions about academic issues and life always made me motivated and strong. I can't imagine anyone who would make a better best friend than him, and I'm so happy to have him in my life.

I also appreciate the kindness and support of Khosro Tehranizadeh and Asiyeh Amjadi who became my second family. They always believed in me and this was a great motivation for me. Our long conversations about any aspect of life and their positive energy and recommendations encouraged me for passing different steps of life. Aysan, my little sister, helped me to make the hard times easier and the easy times more fun. Aysan and Farzin were always the reason for my loud laughter. Their supports, especially during the last days of my study, is very valuable for me.

To Baba

TABLE OF CONTENTS

LIST OF TABLES

LIST OF FIGURES

LIST OF SYMBOLS

a	Thermal diffusivity
a_p	Depth of cut
a', b', c'	Coefficients of normal pressure equation on flank face
A, B, n, m, υ	Material constants for JC equation
$B_{tool}, B_{chip}, \Delta B, e$	Parameters of non-uniform heat partitioning equation
$B_{i,chip}$	Local heat partition for chip side
$B_{i,tool}$	Local heat partition for tool side
c	Heat capacity
d	Workpiece diameter
f	Feed rate
h_0	Uncut chip thickness
h	Heat convection coefficient
h_s	Thickness of shear band
i	Inclination angle
J	Jacobian of transformation
k	Thermal conductivity
l_1, l_2, l_3	Lengths of different segments on flank face
l_{p2}	Sticking contact length on rake face
l_{c2}	Total contact length on rake face
l_{p3}	Sticking contact length on flank face
l_{c3}	Total contact length on flank face
l_{cw}	Total contact length on flank face of a worn tool
P	Normal pressure on the rake face
P_0	Normal pressure at the tool-tip
P_3	Normal pressure on the flank face
P_{avg}	Normal pressure on the worn area of the tool
q_2	Heat flux on the rake face
q_3	Heat flux on the flank face

$Q_{(s)}$	Laplace transform of heat flux equation
r	Cutting-edge radius
r_n	Nose Radius
t	Time
T	Temperature
$\overline{\mathrm{T}}$	Laplace transform of temperature equation
T_1	Temperature at the exit of shear band
T_m	Melting temperature of the workpiece
T_r	Reference temperature
T_w	Initial workpiece temperature
T_∞	Room temperature
V_i	Local velocity along flank contact
V_c	Cutting speed
V_{ch}	Chip velocity
VB	Flank wear
VN	Depth of cut line in a worn tool
x, y, z	Orthogonal coordinate system
x_2, y_2	Coordinate system at the rake face
x_3, y_3	Coordinate system at the flank face
w	Depth of cut
w_c	Depth of cut in oblique cutting
α	Rake angle
α_n	Normal rake angle
α', β', γ'	Geometrical coefficients in mesh generation
β	Friction angle
β_n	Normal friction angle
γ	Shear strain
γ_1	Shear strain at the exit of shear band
$\dot{\gamma}$	Shear strain rate
$\dot{\gamma}_0$	Reference shear strain rate
ζ	Pressure distribution exponent
κ	Approach angle

θ	Stagnation angle
θ_{w1}, θ_{w2}	Angles of a worn tool
λ	Clearance angle
μ_a	Apparent friction coefficient
μ_{sl}	Sliding friction coefficient
ξ, η, ϑ	Computational coordinates for tool
η_c	Chip flow angle
η_s	Shear flow angle
ρ	Density of the workpiece
τ	Shear stress
τ_0	Shear stress at the entry of shear band
τ_1	Shear stress at the exit of shear band
ϕ	Shear angle
ϕ_n	Shear angle in the normal plane
χ	Fraction of the work converted into heat

1. INTRODUCTION

1.1. Introduction and Literature Survey

Measuring the temperature during machining and examining its effect on the workpiece and tool is an important subject that has been researched for many years. The main purpose of measuring the temperature is to extend tool life and, in turn, improve surface quality. Modeling the heat generation during cutting or measuring the temperature can be helpful for predicting the tool wear and developing software. The cutting temperature has a significant effect on the dimensional accuracy, sub-surface damage, residual stress, as well as part quality. In addition, a common method or system that can accurately measure the temperature for all the cutting processes has not been developed yet.

The performance and efficiency of machining operations are inversely affected by the temperature. Tool wear and material expansion are affected by even small changes in local temperatures. The increase of wear is a result of exponentially activated mechanisms, as temperatures at the tool-workpiece interface increase with increasing the cutting speed [1].

Heat generation occurs in three regions during the machining process. The first is the primary deformation zone where chip formation takes place. In this region, the workpiece entering the shear plane undergoes plastic deformation due to shear stresses and forms the chip. More than 90% of the energy consumed for plastic deformation in this region is converted to heat [2]. After chip formation, heat generation occurs in the second deformation zone, which is formed due to the friction between the tool rake face and chip [2]. The presence of a cutting-edge radius and the ploughing effect results in frictional contact between the tool flank face and the newly machined surface of the workpiece. This region can be considered the third heat generation zone. [2].

Since the second half of the 19th century, the role of temperature in metalworking has been studied. If the cutting temperature is too high, tool wear will increase, the workpiece may be damaged, and residual stresses remain in the finished part. In addition, surface roughness and machining tolerances are directly affected by the temperature [3]. Cutting speed and feed rate are also cutting parameters that significantly affect the cutting

temperature. Although increasing the cutting speed cutting forces are not affected much, it results in the increase of energy loss. This causes the rate of heat generation to increase in the cutting zone. If the heat transfer coefficient and heat capacity of the material is higher, the heat generated will pass to the workpiece more quickly and cause thermal expansion. The dimensional and shape errors caused by this phenomenon can be reduced by designing the appropriate production method. In order to be able to choose the appropriate cutting parameters, tool geometry, and process sequence, the heat transfer occurring during machining should be well understood [4].

During machining, most of the energy is spent for the plastic deformation of the workpiece and frictions on the rake and flank faces of the tool. This causes the workpiece and tool temperatures to increase. The temperature distribution depends on the thermal properties of the tool and workpiece, the heat loss due to radiation and convection.

Research on cutting temperature study was initiated by Taylor's experimental work in 1907 [1]. According to his work, increasing the cutting speed decreases the tool life. He developed an empirical formula for tool temperature, which is still used today, representing the relation between cutting speed and tool life. However, the studies that are considered as the basis for the modeling of heat generation in machining processes started after Merchant's [5] basic study on the mechanics of chip formation.

In machining, the deformation happens in a very small region and the heat generated in this region affects the tool and the workpiece. High cutting temperatures significantly affect tool wear, tool life, surface quality, chip formation, and thermal deformation of the cutting tool, which is the biggest source of errors in machining. In the first region, the increase in the temperature of the workpiece causes the material to soften, which reduces the required cutting forces and the energy for happening the shear. The temperature variation at the tool-chip interface affects the friction condition, the location of the primary, second, and third deformation zone, the location of the maximum temperature, and the heat partition ratio.

Measurement of temperature and estimation of heat dissipation during machining is difficult due to the small dimensions of the shear zone, chip movement, and the physics of the contact at tool-chip and tool-workpiece interfaces, which are in constant contact and in motion. The tool tries to overcome the shear strength of the workpiece. This causes a large amount of heat generation in the workpiece, creating thermo-mechanical deformation in the shear region. The stress-strain relationship and material flow are

affected by the temperature in the cutting zone. In general, when the temperature rises, the strength of workpiece reduces, increasing the ductility. It can be assumed that almost all the energy input during the cutting process is converted into heat [6-7]. In machining, the consumed power and generated heat depend on the material properties of the workpiece and tool, cutting parameters, and tool geometry. According to Trent's [8] study, for continuous chip formation and average cutting speed, the heat generated in the primary deformation zone accounts for 20-35 percent of the total heat generation due to plastic deformation and friction in the secondary region. As a result, it is important to consider the first region when calculating the temperature of the tool.

Modeling studies to date can be categorized in two different groups: analytical and numerical models. Blok's [9] energy partition ratio is used in the majority of analytical models for temperature prediction. Blok's approach [9] is only applicable for two parts, one stationary and the other moving. Therefore, it is used for the distribution of heat at the tool-chip interface.

One of the earliest analytical investigations on the calculation of the cutting temperature was done by Trigger and Chao [10]. They developed a time-independent two-dimensional model for the calculation of the average temperature during the cutting process. The average temperature at the tool-chip interface was calculated by considering the heat generation mechanism during the metal cutting process. They assumed that the heat generated in the shear plane only affects the chip and defined the tool-chip interface as adiabatic. In this study, 90% of the heat generated is considered to be transferred to the chip and 10% to the tool.

Loewen and Shaw [11] explained that the effect of some variables on the cutting temperature cannot be obtained experimentally. They developed an analytical model in which the tool-chip interface temperature is calculated. In this model, it is assumed that the heat flow rate in the chip is constant along the rake face at the tool-chip contact area. Loewen and Shaw modeled the cutting temperature by modeling the shear plane as a moving heat source that moves with shear velocity. In their analysis, they assumed that all the power consumed for deformation is converted into heat. They derive a useful expression for the mean temperatures in the shear plane and at the tool-chip interface. Their approach makes it possible to understand the effect of process parameters on the cutting temperature. They used Blok's energy partition ratio. They considered the tool-chip interface adiabatic and assumed that only the chip side is affected by the heat in the

shear plane.

Weiner [12] proposed an analytical model for estimating temperature distribution on the shear plane during orthogonal cutting. In his study, the shear plane speed is considered to be equal to the cutting speed. In addition, conductional heat transfer in the direction of chip and workpiece motion is ignored. As a result, the temperature distribution for the shear plane was obtained in detail. In this study, the chip outer surface and the tool flank were considered adiabatic, and the heat caused by friction at the chip-tool interface was calculated using the average coefficient of friction.

Boothroyd [13] and Wright [14] developed similar models using Weiner's energy dissipation ratio analysis. The thermal characteristics of the part are considered to be temperature-independent. Boothroyd also neglected the heat conduction in the chip velocity direction, assuming that the heat partition ratio in the contact area is not varying. In addition, the heat transferred to the tool is constant. Wright [14], on the other hand, assumed that 80% of the heat caused by friction in the contact area is transferred to the chip, considering the sticking and sliding friction conditions.

Venuvinod and Lau [15] introduced an oblique cutting model and assumed the tool and workpiece to be semi-infinite domains. The moving heat source solution was applied to the moving tool with an oblique angle. The effect of the shear plane was modeled by developing analyzes of Loewen and Shaw [11]. In addition, the ratio of heat flow into the tool and chip at the tool-chip interface was calculated according to the energy partition ratio of Blok.

Berliner and Krainov [16] developed a model for the temperature distribution in the tool and chip. They modeled the heat generated at the tool-chip interface as a parabolic heat source. They also considered the effect of cooling in their analysis. The deformation energy is taken into account in the analysis as an exponential function. They also included the friction between the tool and the workpiece at the flank face.

Young and Chou [17] obtained the temperatures at the tool-chip interface independent of time under orthogonal cutting conditions. They assumed a constant heat flux distribution at the shear plane and tool-chip contact and ignored heat conduction in the direction of motion. They concluded that the rake face reaches its maximum temperature at the end of tool-chip interface.

Redulescu and Kapoor [18] investigated the temperature at the tool-chip interface by applying a mechanistic force model to solve the heat conduction problem. The results

showed that the temperature at the tool-chip interface increased with increasing the cutting speed in both interrupted and continuous cutting. The analysis was performed in three dimensions for semi-stationary conditions. Then, the temperature values for the tool and chip were obtained according to the heat fluxes calculated in the previous step. They also took into account heat loss by convection in the tool and chip formation regions. They developed an important model to understand the behavior of the time-dependent heating and cooling cycles in milling.

McFeron and Chao [19] developed a model for the analytical calculation of the mean temperature at the tool-chip interface. For the calculation of tool temperatures, Stephenson et al. [20] proposed a time-dependent model. The separation of variables approach was used to solve the heat transfer problem for the tool. In order to decrease calculation time, the adiabatic boundary condition is applied to the surfaces in contact with the air. Piecewise-constant heat flux was considered to be applied to a rectangular insert. In another study considering orthogonal cutting, Moufki et al. [21] demonstrated the friction coefficient in the tool-chip contact region with a temperature-dependent model. For heat calculations, they took into account the energy generated in the primary and second deformation zones. They assumed that 90% of the energy used for plastic deformation in the primary deformation zone turned into heat. In the second deformation zone, they calculated only the heat and temperature distribution in the tool-chip contact area, and they did not include the temperature distribution inside the tool and workpiece in the model.

Levy et al. [22] presented a two-dimensional, time-dependent analytical thermal model for the temperature distributions in the tool and chip for orthogonal cutting. The frictional heat source is introduced to the model with a heat flux at the boundary and is assumed to be variable along the contact interface. In addition, the heat generation of the shear plane was added to the model as an internal heat source.

Komanduri and Hou developed a model for orthogonal cutting, which includes the heat generation due to friction at the tool-chip interface and deformation in the shear plane. The study is based on Hahn's [23] oblique band heat source model for the shear plane, Chao and Trigger's [24] friction model for the tool-chip interface, and Jaeger's [25] oblique band heat source in a semi-infinite medium. The temperature increase in the chip and in the shear plane, which is due to the heat generation in the primary deformation zone, constitutes the first part of their study [26]. In the second phase of their research,

they calculated the temperature rise in the tool and temperature depending on the frictional heat source [27]. The combined effect of the shear plane and frictional heat sources on the temperature increasement of the tool-chip contact area is studied in the final section of their research [27]. According to the result of their study, the heat generated in the shear plane can increase the temperature at the rake contact by 200 °C. In a similar study, Karpat and Özel [28] analytically modeled the temperature distribution in orthogonal cutting operations. These researchers used the Johnson-Cook equation to model the primary deformation zone and modified Oxley's [29] parallel shear zone theory. In the second deformation zone, they applied the non-uniform moving band heat source and complex friction condition, and calculated the heat partition ratio between the tool and chip using the equation developed by Komanduri and Hou [30].

Considering analytical modeling studies, it is seen that most of them are concentrated on orthogonal cutting operations. There are few studies on analytical modeling of temperature distribution in oblique cutting and turning operations. As an example, Lazoglu and Islam [31] proposed a model for the tool and chip temperature distribution in oblique cutting and turning using the 3D heat equation and finite difference method. In this study, experimental verification was not performed. Also, the effect of the third deformation zone and the complex friction condition in the rake contact were not taken into account.

Rapier [32] was the pioneer of using the finite difference method and analytical model together in the calculation of the temperature distribution. In this study, the tool, chip, and workpiece are considered separate parts. The shear plane was assumed to be a linear heat source. He also assumed that the total frictional heat is transferred to the chip. In their analysis, chip temperatures are analytically modeled by ignoring heat conduction in the chip velocity direction. This study showed that the point with the highest temperature in the second region is located at the end of the tool-chip contact length. The finite difference method was used to calculate the temperature distributions in the tool and workpiece. In a later study, Ulutan et al. [33] proposed a 3D model for the temperature distribution in the tool and workpiece in orthogonal cutting considering the conduction and convection effects. They solved the heat transfer equation analytically in three dimensions, calculated the temperature distribution using the finite difference method, and then verified the model experimentally.

The most commonly used method in numerical studies is the Finite Element Method

(FEM). An early investigation on cutting temperature using FEM was conducted by Stevenson and Wright [34]. They calculated the maximum cutting temperature and verified the predictions experimentally. In a similar study, El-Wardany et al. [35] experimentally validated the tool temperature distribution calculated with FEM.

In another numerical study, Ostafiev et al. [36] took the tool as a semi-infinite medium and obtained the tool temperatures in orthogonal cutting, independent of time. The tool temperatures at the tool-chip interface were calculated by the superposition effect of many rectangular heat sources with constant flux.

Grzesik et al. [37] developed a numerical model using the finite difference method. The model they developed can be used for coated and uncoated tools. Models developed prior to their work were developed only for uncoated tools. In their study, the temperature distribution in the tool-chip interface and in the tool was modeled. In addition, they considered the variation of the thermal properties with the change of temperature. Heat conduction in the chip flow direction is neglected.

In a recent study, Mane et al. [38] used a 2-D finite element model to investigate the effect of variable friction coefficient and heat partition ratio on cutting forces and temperature of orthogonal cutting. They concluded that with the increase of feed rate, the location of maximum temperature along the chip-tool interface moves toward the tool-tip. In addition, using the variable friction coefficient reduces the maximum tool temperature significantly.

Huang and Liang [39] modeled the heat generated during orthogonal cutting. They included the heat generation from wear and varying heat flux of the tool-chip interface in their model. It was observed that increasing flank wear had no apparent effect on the average rake face temperature. However, increase of flank wear length and cutting speed resulted in higher average temperatures on the flank and rake faces. After this study, Li and Liang enhanced this model by adding the effect of cooling [40]. The finite element method was successfully applied for orthogonal cutting conditions. This method requires a significant amount of experimental work to determine the mechanical properties since so many input parameters are needed in finite element simulations.

Dutt and Brewer [41] calculated the temperature distribution using the finite difference method. Tool, chip, and workpiece are considered as separate parts interacting only at the interfaces. In their studies, the heat distribution for tool, chip, and workpiece was determined by solving the linear equations written in the form of finite differences for the

shear plane and tool-chip interface boundaries. The problem is considered to be steady-state. Contrary to Rapier's work [32], it is assumed that all of the heat caused by friction is transferred to the tool.

Smith and Armarego [42] modeled the tool and chip temperature distribution for orthogonal cutting in three dimensions using the finite difference method. Their analysis is based on a thin shear zone model. It is assumed that the frictional heat source does not change along the tool-chip interface. In their work, they took the temperature of the tool back surfaces constant and showed that the temperature on this surface had no effect on the temperatures at the interface. Using the finite difference method, Lazoğlu and Altıntaş [43] calculated the change in the tool and chip temperature for the transient and steady-state temperatures in continuous cutting and milling operations. They developed the heat model using partial differential equations for the chip and tool in Cartesian and cylindrical coordinates, respectively. The variation of chip thickness with time is neglected to obtain the transient temperature distribution in the interrupted cutting process like milling. The heat generation in the shear plane is defined by Oxley's [29] energy partition function, and the frictional heat source is assumed to be constant.

Tay et al. [44] were the first to model the temperatures of orthogonal cutting in the tool, chip, and workpiece using the finite element method. The formulations were developed for two-dimensional analysis. The strain, strain rate, and velocity distributions were obtained by Stevenson and Oxley [45] using quick-stop experiments. In addition, experimental data were used to obtain velocity distributions and frictional stresses in the second deformation zone. Although they achieve good results of temperature distribution, a large number of experiments are required to estimate the temperature by this method. After this study, Tay et al. [46] developed a model which reduced the dependence on the experiments. The expression of the heat source in the primary deformation zone was simplified, and the elastic behavior between the tool and the chip was neglected.

Muraka et al. [47] developed a model in which they examined the cutting speed, wear in the third deformation zone, and the coolant effect with the finite element method. The major problem with their approach is that a large number of experiments are required to obtain the strain in the primary and second deformation zones. Using the finite difference method, Usui et al. [48] and Tlusty et al. [49] developed an approach for steady-state temperature distribution in continuous machining. It was observed that the numerically calculated temperatures were lower than the experimentally measured values at the

cutting edge and chip separation point. Shi and Attia [50] proposed a friction model based on Usui's empirical approach of tribological interaction for tool-chip interface. The thermal constriction resistance model developed by Attia and Kops [51] is used to describe the thermal interaction between the chip and the uncoated tool. For orthogonal cutting condition, the two models are merged in the FEM simulation. Cutting force, thrust force, and chip thickness were calculated and compared to experimental data in the literature. In addition, the proposed method estimates the maximum tool temperature and residual stresses in the workpiece.

In a new study, Avevor et al. [52] analytically and numerically modeled the heat calculation in the second deformation zone. In this study, a numerical solution was used to calculate the heat partition between the tool and chip over time. Experimental verification was not performed in this study.

In another study, Islam et al. [53] enhanced the finite difference method for transient thermal analysis in the machining process. The proposed model was verified using available experimental results in the literature for interrupted machining. In a recent study, Shan et al. [54-55] proposed an improved analytical model of the cutting temperature in orthogonal cutting of titanium alloys, based on the Komanduri-Hou model. The study includes the clearance angle in the model. However, the tool is considered to be sharp, and the effect of tool-workpiece contact is neglected.

Although temperature distribution has been clearly presented by FEM models, especially in 3D, due to the high number of inputs for the numerical analysis, model predictions have generally been inconsistent with the experiments [2]. Another reason for errors in both 2D and 3D FEM studies is that the third deformation zone has not been considered in the analysis properly [2-56]. In such studies, the researchers have experimentally entered the results of temperature and force measurement into the FEM models to calculate and analyze parameters such as heat conduction coefficient and heat partition ratio [57-58]. The purpose of these studies is to achieve the desired coefficients from various solutions through iterative analysis. In an exemplary study, Umbrello et al. [59] calculated the heat conduction coefficient with the simultaneous use of 2D FEM analysis and experimental results. Then, using commercial FEM software, they calculated the temperature distribution for the turning operation.

Another important issue in machining is temperature measurement. Since the chip formation occurs in a very small area, the available methods for temperature measurement

are not efficient enough. The thermocouple, pyrometer, thermal camera, and metallographic techniques have been widely used for temperature measurement in previous researches. Studies on this subject were presented in two important review articles [60-61]. Grzesik [62] carried out average temperature measurements by means of thermocouples, connecting the workpiece and the tool electrically. In another study, Korkut et al. [63] performed temperature measurements by embedding a K-type thermocouple into the tool. The main problem of temperature measurement by embedding thermocouples in the tool is the limited number of points at which temperature measurement can be made since holes are needed to attach thermocouples to the cutting tool. Moreover, the thermocouple can be located at a certain distance from the desired point. This necessitates the calculation of temperature at the measured point with heat conduction equations or FEM methods [64-65]. The advantage of using a thermocouple is that its measured temperature is not affected by chip, coolant, and other factors during the machining operation. In another study, Mzad [66] measured temperature using an infrared laser. However, the used system was highly affected by vibration. Therefore, it may only be suitable for use in a highly controlled laboratory environment. Thermal camera has also been widely used for temperature measurements in machining [2-64-65]. The advantage of the thermal camera is a direct measurement of the temperature distribution in the workpiece and tool. There are also several problems with thermal camera measurements. The first is the calibration of emissivity value. Since the surface color of the workpiece or tool changes with temperature or oxidation, a detailed calibration of emissivity is required [64-65]. Another problem is that the chip and coolant generated during operation can easily enter the camera's imaging area and prevent measurement. Therefore, coolant cannot be used during thermal camera measurements. In addition, 3D temperature measurement with a thermal camera is not practical and does not provide real values. When the studies on temperature measurement are evaluated, it can be concluded that there is still no method that can measure the local temperature values in the cutting-edge and chip removal area practically and directly. This increases the importance of temperature models in machining.

Soler et al. [67] proposed a new method for the calibration of the emissivity value for the thermal camera. Although it is not an easy test setup, it was claimed that the proposed method achieves a more accurate emissivity value. Denkena et al. [68] calibrated their developed model for temperature by performing experiments in which they placed

thermocouples at various points on the workpiece. They developed a model that can calculate the temperature change during the entire machining process. However, for any tool path and part, the model needs to be recalibrated.

Kryzhanivskyy et al. [69] proposed an approach based on the inverse heat conduction technique, and a time-dependent heat flux model was developed by utilizing force-temperature measurements. Since this method is extremely sensitive to measurement errors, they designed a special experimental setup to minimize temperature measurement inaccuracy. The study has two steps: The value of the heat flux that is constant over time, as well as specific tool heating energy, are derived in the first step. The measured energy over time is redistributed in the second phase by parametrizing and comparing predefined heat flux characteristics. The results demonstrate that a reducing power function may be used to explain the time-dependent heat flux.

Using temperatures obtained at some sensor-accessible points, Haung et al. [70] developed an online inverse approach to estimate the temperature distribution at the tool-chip interface of a turning tool. An inverse heat conduction problem is used to calculate the transient heat flux induced at the tool-chip contact. The temperature distribution is then calculated using a three-dimensional non-linear thermal model. The study is verified experimentally and numerically.

In a recent study, Chen et al. [71] developed a 3D FEM thermal model using the inverse heat transfer method to predict the machined surface temperature near the cutting zone. They performed two sets of experimental measurements to verify their model. As the first method, a metal foil is embedded in the workpiece to measure the tool tip temperature. The second method uses a thermocouple embedded in the tool with its tip continuously sliding on the machined surface behind the cutting edge during hard turning.

Biermann et al. [72] designed an in-process monitoring system for temperature measurements during the turning process. In this work, a novel tool sensor system with a Nickel PVD coating and a Nickel-Chromium layer on the rake face of cutting inserts is introduced. Three thermocouples were deposited on the junction points of this layer structure.

Saoubi [73] studied the technique of mapping isotherms on the lateral face of the tool in single-point turning using dedicated infrared CCD sensors. This work discusses the role of calibration and associated errors in the accuracy of temperature measurement.

Harzallah et al. [74] used a novel bi-spectral imaging device that can simultaneously

measure the kinematic and thermal fields in the orthogonal cutting experiment. The apparatus is used to image small-scale areas at small to moderate cutting speeds. A complex post-processing procedure is used based on the finite strains framework to obtain strain, strain rate, temperature, and dissipation fields from raw data.

The measurement of temperature during the milling operation is more challenging when compared to the turning operation. Karaguzel and Budak [75] proposed a novel approach to model and measure the variations of cutting tool temperature during milling. The study provides a relationship between tool temperature and radial depth of cut. In addition, the study investigates the effect of coolant on cutting temperature based on proposed model predictions.

Mohring et al. [76] calculated the orthogonal cutting temperature analytically by considering the dependence of the heat flow density on the temperature. In addition, the accumulation and plastic contact region are considered in the model. In the experimental part of the study, the temperature was measured at the exterior surface of the chip using high-speed pyrometers as well as on the flank face using the set-up proposed by Heisel et al. [77]. The maximum temperatures on the chip were compared with the model results for which low error rates were obtained. Navarro-Devia et al. [78] conducted a study based on experimental temperature measurement. They measured the temperature of the tools with an infrared sensor during the turning operation. In this study, the cutting temperatures for coated and uncoated HSS tools were compared, and the relationship between wear characteristics and the temperature was discussed.

In a recent investigation, Saelzer et al. [79] developed a new experimental setup for the high-speed measurement of the rake face temperature in orthogonal cutting. The study examines the influence of different rake face preparation methods and cutting parameters on the temperature of the rake face.

Using coated tools prevents direct contact between the workpiece and tool faces. This can significantly decrease the tool temperature in comparison to uncoated tools. Recently, Zhao et al. [80] have reviewed the effect of geometric parameters, thermal physical characteristics, coated tool-chip interface properties, and the coating-substrate diffusion layer on the cutting temperature. Furthermore, analytical and experimental studies regarding coated tools are reviewed and analyzed. Zhao and Liu [81] investigated the cutting temperature when using PVD coated carbide tools in dry cutting of Inconel. They examined the effect of coting thickness on the cutting temperature of worn tools in the

initial stages. The cutting temperature was measured with the two-color thermometer [82], which is a contactless measurement. The eliminated emissivity effect in this method can improve the accuracy of the measured maximum cutting temperature.

List et al. [83] conducted a FE analyses using Abaqus to predict the interface cutting temperature and its relation with the crater wear mechanism during high-speed machining. A method based on some analytical preliminary calculations was proposed to determine the friction shear stress and the heat partitioning factor between the tool and the chip. A CCD camera was used in the experiments to measure the temperature field inside the chip. Attanasio et al [84] developed a 3D numerical model to predict the tool wear in metal cutting. They used an analytical model as a subroutine to include the wear in their numerical model. They considered a heat transfer coefficient as a function of cutting speed and feed rate in their calculations and FEM results were compared with some experimental data. Karpat and Ozel [85] introduced a predictive modeling technique to predict cutting forces and temperature while considering the influence of flank wear They also examined the heat partition ratio on the tool-chip and tool-workpiece interfaces. The model predictions were verified experimentally.

According to the provided literature review, including the effects of all deformation zones, cutting-edge radius, and complex friction conditions on the rake and flank faces, convection effect and tool wear in a single model is a need in the field of cutting temperature modeling. The present study aims to develop a comprehensive model that considers all the above-mentioned factors and can predict the cutting tool temperature for orthogonal, oblique and turning operations, having the cutting parameters and tool geometry.

1.2. Objective

As discussed above, heat formation in machining is one of the most important physical factors that affects the cutting process, cutting tool health, workpiece behavior, final surface quality, and ultimately machining cost.

As can be concluded from the literature, many studies have been performed on machining temperature modeling and measurement. However, there are some assumptions in these studies that can affect the results significantly. For instance, in most of the previous

studies, the tool tip has been considered to be sharp, and the effect of cutting-edge radius has been neglected. However, the existence of this region results in contact between the flank face of tool and machined surface of the workpiece. Flank wear that significantly reduces tool life is a result of flank contact, and its rate increases with the increase of flank temperature. Another important factor in machining processes that is highly affected by temperature of the third deformation zone is the part quality and surface integrity of the machined workpiece. All of these demonstrate the importance of modeling heat generation in the third deformation zone that can affect the maximum flank temperature, location of maximum temperature and temperature distribution inside the tool and workpiece. Another important issue in temperature modeling, is the type of contact on rake and flank faces. In some of studies it is assumed that this contact is purely sliding or sticking. However, in reality the frictional behavior on the tool-chip and tool-workpiece contact is a complex sliding-sticking type. FEM based models which are widely used for temperature prediction, have long solution times and there are problems with the prediction accuracy of these models. Consequently, an accurate model with low solution time is a necessity in the field. Having a comprehensive model, that reduces the number of simplifications will result in more realistic results and can be used to predict the cutting temperature for different processes.

The proposed model in this study is one-step ahead from the previous ones as it includes for the first time in a single model the effects of all deformation zones[86], cutting-edge radius, dual friction conditions in rake and flank faces [87], and the convection effect. In this study, the temperatures at the tool-chip and tool-workpiece boundaries are calculated analytically. In addition, for non-contact regions of rake and flank faces, the convective boundary condition is considered. After applying the boundary conditions, the temperature distribution inside the tool is calculated using the Finite Difference Method. The model is first developed for the orthogonal cutting. Although modeling of the orthogonal cutting can be considered as the base of study, due to the geometry of the cutting tool and process, having a 3D model provides a more realistic approach to predict the cutting temperature. Once the orthogonal cutting model is developed, oblique cutting and turning processes can modeled using geometrical and kinematical transformations [88-89] for the force and heat flux calculations. The proposed model is also modified for the calculation of cutting temperature in tools with flank wear. As the final step, experimental study is performed to verify the proposed model.

1.3. Layout of the Thesis

The thesis is organized as follows:

In Chapter 2 the proposed models for the simulation of cutting temperature in orthogonal cutting, oblique cutting and turning operations are presented. The finite difference method is provided and the detailed formulation regarding the derivation of the equations is shown. The solution method are also described for each operation. In addition, the model is modified for predicting the temperature for worn tools.

In Chapter 3, the experimental study for the verifications of the proposed orthogonal, oblique, and turning models are presented. Also the effect of tool wear on the cutting temperature in different conditions are examined and compared to model predictions.

In Chapter 4, the effect of cutting conditions and tool geometry on the cutting temperature of rake and flank faces are investigated using the results of proposed model. The effect of cutting speed, rake angle, clearance angle, stagnation angle, inclination angle, cutting edge radius, nose radius, and flank wear on the cutting temperature is presented and discussed.

In Chapter 5, the suggestions for the further research are presented.

In Chapter 6, the contributions of the thesis to the literature and the conclusions are provided.

2. TEMPERATURE DISTRIBUTION MODELING

2.1. Temperature Distribution in Orthogonal Cutting

2.1.1. Heat Generation in the Primary Shear Zone

In this study, the primary shear zone is modeled as a thin band. This model is based on the work of Molinari and Dudzinski [90-91], and Johnson-Cook was chosen as the constitutive equation for presenting the material behavior [92]:

$$\tau = \frac{1}{\sqrt{3}}\left[A + B\left(\frac{\gamma}{\sqrt{3}}\right)^{n}\right]\left[1 + \ln\left(\frac{\dot{\gamma}}{\dot{\gamma}_0}\right)^{m}\right]\left[1 - \left(\frac{T_w - T_r}{T_m - T_r}\right)^{\upsilon}\right] \quad (1)$$

where τ is the shear stress; γ is the shear strain; $\dot{\gamma}$ is the shear strain rate; $\dot{\gamma}_0$ is the reference shear strain rate; T_w is the absolute temperature of workpiece; T_r is the reference temperature; T_m is the melting temperature of workpiece; and $A, B, n, m,$ and υ represent the material constants. In the modeling of this region, the following assumptions were made (Figure 1):

- The primary shear zone is a band of thickness h_s.
- No deformation occurs in the workpiece outside of the shear zone.
- The workpiece enters the shear band with initial shear stress, τ_0, and exists this region with τ_1.
- A uniform pressure distribution exists in the primary shear zone.
- The heat generated by the secondary and third deformation zones do not substantially affect the hypothesis of one-dimensional distribution of the shear strain and of the temperature in the primary shear zone [91].

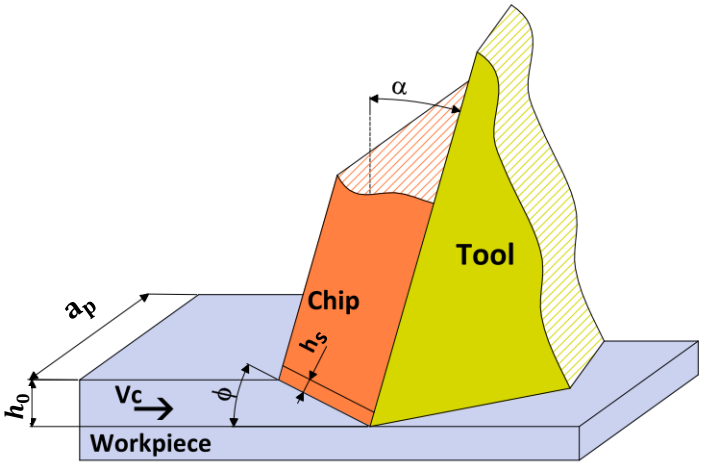

Figure 1. Primary deformation zone in orthogonal cutting

From the conservation of momentum, τ_0 and τ_1 were calculated iteratively using the following equation [21]:

$$\tau_1 = \rho(V_c \sin\phi)^2\gamma_1 + \tau_0 \tag{2}$$

where τ_0 is the shear stress at the entry of shear band; τ_1 is the shear stress at the exit of shear band; γ_1 is the shear strain at the exit of shear band; ρ is the workpiece density; V_c is the cutting speed; and ϕ is the shear angle. Considering the conservation of energy in the adiabatic condition, the temperature at the exit of the shear band can be calculated as [21]:

$$T_1 = T_w + \frac{\chi}{\rho c}\left(\rho V_c^2 \sin^2\phi \frac{\gamma^2}{2} + \tau_0\gamma\right) \tag{3}$$

where T_1 is the temperature at the exit of shear band; χ is the fraction of the work converted into heat; and c is the heat capacity. In previous experimental studies, χ has been found to be 0.9 for metals [93]. The shear stress at the start of the shear band, τ_0 , can be calculated iteratively by using below equation:

$$\frac{d\gamma}{dy} = \frac{d\gamma}{dt}\frac{dt}{dy} = \frac{\dot{\gamma}}{V_c \sin\phi} \tag{4}$$

The boundary conditions for Equation (4) are [92]:

$$T = T_w \qquad @\ y = 0 \tag{5}$$

$$\gamma = 0 \qquad @ y = 0 \tag{6}$$

$$\gamma = \gamma_1 = tan(\phi - \alpha) + \frac{1}{tan\,\phi} \qquad @y = h_s \tag{7}$$

where α is the rake angle. After determining τ_0, the shear stress and temperature at the exit of the primary deformation zone, τ_1 and T_1, can be calculated using Equations (2) and (3), respectively [21].

2.1.2. Heat Generation in the Second Deformation Zone

The second deformation zone is the friction zone where the tool and formed chip are in contact. In the modeling of the second deformation zone, the following assumptions were made:

- The heat transfer in the chip flow direction does not need to be included in the heat calculation, as it is negligible due to the high speed of the chip [21].
- Rake face contact is represented by the dual-zone model [94].
- Steady-state and time-independent conditions are considered in the model.

In this study, the rake face contact was modeled considering two different friction regions by using the dual-zone model [94]. At the area close to the tool tip, sticking friction exists due to the high normal pressure. The reduced normal pressure converts the contact state to sliding friction (Coulomb friction) along the rake contact. The described friction state can be expressed as follows [94]:

$$\tau = \begin{cases} \tau_1 & x_2 \le l_{p2} \\ \mu_{sl} P & l_{p2} \le x_2 \le l_{c2} \end{cases} \tag{8}$$

where τ is the shear stress; τ_1 is the shear stress at the exit of the shear band; μ is the sliding friction coefficient; P is normal stress; x_2 is the distance from the tool-tip on the rake face; l_{c2} is the rake contact length; and l_{p2} is the sticking contact length. The normal stress distribution can be described as [92]:

$$P(x_2) = P_0 \left(1 - \frac{x_2}{l_{c2}}\right)^{\zeta} \tag{9}$$

where P_0 is the normal stress at the tool-tip; and ζ is the pressure distribution exponent, which has been calculated experimentally to be equal to 3 [95-96]. By considering the momentum equilibrium on the chip, the chip tool contact length and the length of the sticking zone can be calculated by using the following equations [94]:

$$l_{c2} = h_0 \frac{\zeta + 2}{2} \frac{sin(\phi + \beta - \lambda)}{sin\phi cos\beta} \tag{10}$$

$$l_{p2} = l_{c2}\left(1 - \left(\frac{\tau_1}{P_0 \mu_{sl}}\right)^{\frac{1}{\zeta}}\right) \tag{11}$$

where β is the friction angle; h_0 is the uncut chip thickness; and λ is the clearance angle. In this study, the two-dimensional heat equation was solved in order to calculate the heat generated in the secondary deformation region [21]:

$$a\frac{\partial^2 T(x_2, y_2)}{\partial y_2^2} = \frac{V_{ch}\partial T(x_2, y_2)}{\partial x_2} \tag{12}$$

where $a = k/\rho c$ is the thermal diffusivity; k is the thermal conductivity; ρ is density; and c is specific heat capacity. x_2, y_2 are coordinates used for second deformation zone that are shown in Figure 2. V_{ch} is the chip velocity:

$$V_{ch} = \frac{V_c sin\phi}{cos(\phi - \lambda)} \tag{13}$$

As can be seen from Figure 2, the temperature at the end of the primary deformation zone, T_1, can be used as a boundary condition in solving the heat equation. Furthermore, in the developed model, the temperature of the free surface of the chip is accepted as T_1.

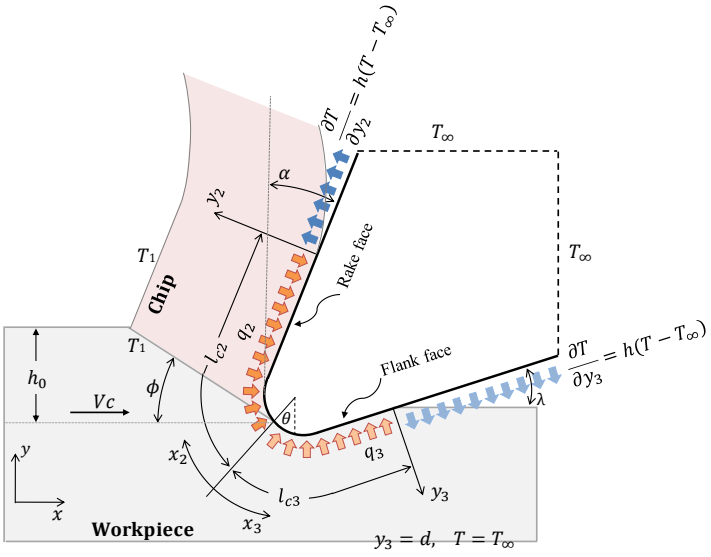

Figure 2. Heat generation and boundary conditions in orthogonal cutting.

In order to solve Equation (12), the boundary conditions are:

$$\begin{aligned} &T(0, y_2) = T_1 \qquad x_2 = 0\,,\ y_2 \geq 0 \\ &\lim_{y_2 \to \infty} T(x_2, y_2) = T_1 \qquad x_2 \geq 0 \end{aligned} \tag{14}$$

$$-k\frac{\partial T(x_2,0)}{\partial y_2} = q_2(x_2) \qquad x_2 \geq 0$$

where q_2 is the frictional heat flux in second deformation zone. In order to solve these equations analytically, the Laplace transformation was used [97]. Equations (14) can be written as follows [21]:

$$\bar{T}(s,y_2) = \int_0^{\infty} T(x_2,y_2)e^{-sx_2}dx_2$$

$$\bar{T}(s,\infty) = \frac{T_1}{s} \tag{15}$$

$$-k\frac{d\bar{T}(s,y_2)}{dy_2} = Q(s)$$

Here, $Q(s)$ is the representation of $q_2(x_2)$ after Laplace transformation. Applying the Laplace transformation on Equation (12), it can be written as:

$$a\frac{d^2\bar{T}(s,y_2)}{dy_2{}^2} = V_{ch}(s\bar{T}(s,y_2) - T_1) \tag{16}$$

Using the Reverse Laplace Transform and convolution property, the temperature distribution inside the chip can be obtained as [21]:

$$T(x_2,y_2) = \frac{1}{k}\sqrt{\frac{a}{V_{ch}}}\int_0^{x_2} q_2(x_2-u)\frac{1}{\sqrt{\pi u}}e^{\left(-\frac{V_{ch}y_2^2}{4au}\right)}du + T_1 \tag{17}$$

Based on the dual-zone model, the heat flux at the tool-chip interface can be described as:

$$q_2(x_2) = \begin{cases} \tau_1 V_{ch} & x_2 \leq l_{p2} \\ \mu_{sl}V_{ch}P_0\left(1-\frac{x_2}{l_{c2}}\right)^{\zeta} & l_{p2} \leq x_2 \leq l_{c2} \\ 0 & x_2 \geq l_{c2} \end{cases} \tag{18}$$

Therefore, the temperature at the tool-chip interface ($y_2 = 0$) can be written as:

$$T(x_2,0) = \frac{1}{k}\sqrt{\frac{a}{V_{ch}}}\left(\int_0^{l_{p2}} \tau_1 V_{ch}\frac{1}{\sqrt{\pi u}}du + \int_{l_{p2}}^{l_{c2}} \mu_{sl}V_{ch}P_0\left(1-\frac{x_2-u}{l_{c2}}\right)^{\zeta}\frac{1}{\sqrt{\pi u}}du\right) + T_1 \tag{19}$$

The heat partition fraction along the contact length is an important issue in the modeling of cutting temperature. In this study, a non-uniform distribution of the heat partition ratio, which was suggested by Komanduri and Hou [27], was used for the tool-chip interface. The function for tool and chip side can be described as [27]:

$$B_{i,chip} = \left(B_{chip} - \Delta B\right) + 2\Delta B\left(\frac{l_{c2}-x_2}{l_{c2}}\right)^e$$

$$B_{i,tool} = \left(B_{tool} + \Delta B\right) - 2\Delta B\left(\frac{l_{c2}-x_2}{l_{c2}}\right)^e \tag{20}$$

where $B_{i,chip} + B_{i,tool} = 1$ for any point on the tool-chip interface. B_{chip}, B_{tool}, ΔB and e are the coefficients, which are calibrated considering equal temperature at the tool-chip interface. These coefficients are obtained experimentally.

2.1.3. Heat Generation in the Third Deformation Zone

In orthogonal cutting, as the workpiece moves towards the tool, the material above the stagnation point (Figure 3) contributes to chip formation, and the material below this point undergoes ploughing and recovery [86]. Therefore, a friction zone exists which involves the newly machined surface and flank face of the tool.

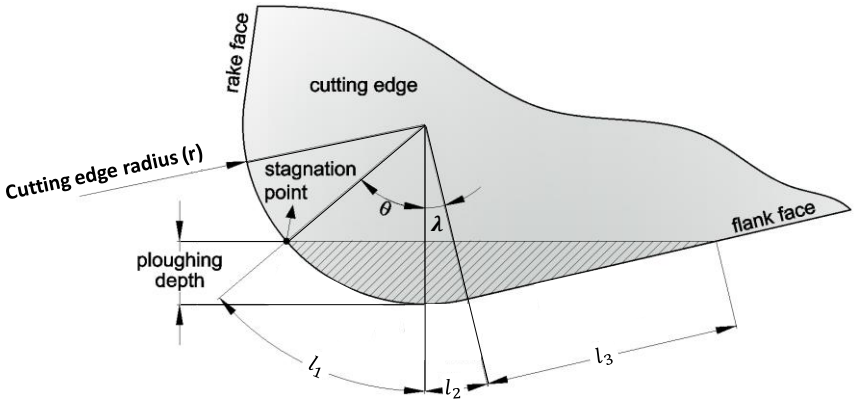

Figure 3. The geometry of the third deformation zone [86].

In the modeling of the third deformation zone, the following assumptions were made:

- Fully elastic recovery is considered for the workpiece in the third deformation zone [86]
- Sticking and sliding friction regions are used to represent the complex friction behavior at the flank face. [86].
- Due to the high cutting speed, the heat transfer in the workpiece movement direction is assumed negligible.
- The normal pressure on the flank face is modeled by an increasing-decreasing trend [86].
- A steady state and time-independent condition is considered in the model.

Considering a fully elastic recovery for the workpiece after the third deformation zone, the total contact length of the flank contact can be calculated as [86]:

$$l_{c3} = l_1 + l_2 + l_3$$

$$l_1 = \theta . r$$

$$l_2 = \lambda . r \tag{21}$$

$$l_3 = r\frac{(cos\,\lambda - cos\,\theta)}{sin\,\lambda}$$

where θ is the stagnation angle; and r is the cutting-edge radius. Stagnation angle is determined based on the experimental procedure proposed by Budak et al. [86]. The normal pressure distribution on the flank face is described as:

$$P_3(x_3) = P_0(a'x_3^2 + b'x_3 + c')$$

$$a' = \frac{1}{2l_{c3}l_3 - l_{c3}^2}$$

$$b' = -2al_1 \tag{22}$$

$$c' = 1$$

where P_0 is the normal pressure at the stagnation point; and x_3 is the distance from tool tip on the flank face. An increasing normal pressure is applied on the material during the contact on l_1 , and then there is a relaxation stage while the material passes from l_2 and l_3, (Equation (22)). Due to the existence of sticking and sliding friction regions on the flank contact, the third deformation zone is represented by a dual-zone contact model. The tool-workpiece contact is modeled to be sticking as the result of high normal pressure and sliding when the normal pressure begins to decrease.

Applying the Coulomb friction law along the sliding zone on the flank face, the following is obtained:

$$\tau_{(x_3)} = \mu_{sl}P_0(a'x_3^2 + b'x_3 + c') \tag{23}$$

where P_0 is the normal pressure at the tool tip. Here μ is considered equal to the sliding friction coefficient on the rake face. At the end of the sticking zone, the tangential stress is equal to the shear yield stress. Therefore, the length of the sticking contact zone can be determined as:

$$l_{p3} = \frac{-b' + \sqrt{b'^2 - 4a'(c' - \frac{\tau_1}{\mu P_0})}}{2a'} \tag{24}$$

In the calculation of the heat generated in the third deformation zone, the 2D heat equation was used, similar to the calculation of the second deformation zone:

$$a\frac{\partial^2 T(x_3,y_3)}{\partial y_3^2}=\frac{V_c \partial T(x_3,y_3)}{\partial x_3} \tag{25}$$

The boundary conditions for solving Equation (25) can be written as:

$$\begin{aligned} &T(0,y_3)=T_1 && x_3=0,\ y_3\geq 0\\ &\lim_{y_3\to d} T(x_3,y_3)=T_\infty && x_3\geq 0\\ &-k\frac{\partial T(x_3,0)}{\partial y_3}=q_3(x_3) && x_3\geq 0 \end{aligned} \tag{26}$$

where T_∞ is the room temperature; and d is the workpiece diameter. The Laplace transformation is used to solve Equation (25) considering the boundary conditions in Equations (26). After applying the Laplace transformation, Equations (25)- (26) can be rewritten as:

$$a\frac{d^2\bar{T}(s,y_3)}{dy_3{}^2}=V_c(s\bar{T}(s,y_3)-T_1) \tag{27}$$

$$\begin{aligned} &\bar{T}(s,y_3)=\int_0^\infty T(x_3,y_3)e^{-sx_3}dx_3\\ &\bar{T}(s,\infty)=\frac{T_1}{s}\\ &-k\frac{d\bar{T}(s,y_3)}{dy_3}=Q(s) \end{aligned} \tag{28}$$

where $Q(s)$ is the Laplace transform of the heat flux q_3. Using the boundary conditions, and Reverse Laplace Transform, the equation for expressing the temperature distribution in the workpiece can be written as:

$$T(x_3,y_3)=\frac{1}{k}\sqrt{\frac{a}{V_c}}\int_0^{x_3} q_3(x_3-u)\frac{1}{\sqrt{\pi u}}e^{\left(-\frac{V_c y_3^2}{4au}\right)}du+\left(\frac{T_\infty-T_1}{d}\right)(y_3)+T_1 \tag{29}$$

Shear stress due to friction conditions in the third deformation zone can be expressed as follows:

$$\tau(x_3)=\begin{cases}\tau_1 & x_3\leq l_{p3}\\ \mu_{sl}P_3 & l_{p3}\leq x_3\leq l_{c3}\\ 0 & x_3\geq l_{c3}\end{cases} \tag{30}$$

Then the heat flux can be described as:

$$q_3(x_3)=\begin{cases}\tau_1 V_i & x_3\leq l_{p3}\\ \mu_{sl}P_0(a'x_3^2+b'x_3+c')V_i & l_{p3}\leq x_3\leq l_{c3}\\ 0 & x_3\geq l_{c3}\end{cases} \tag{31}$$

where V_i is the local velocity along the flank contact. By applying Equation (31) to Equation (29), the temperature distribution in the tool-workpiece interface ($y_3=0$) can

be determined as:

$$T(x_3,0)=\frac{1}{k}\sqrt{\frac{a}{V_c}}\left(\int_0^{l_{p3}}\tau_1 V_i\frac{1}{\sqrt{\pi u}}du+\int_{l_{p3}}^{l_{c3}}\mu_{sl}P_0(a'x_3^2+b'x_3+c')V_i\frac{1}{\sqrt{\pi u}}du\right) \quad (32)$$

The heat partition ratio should also be considered for the tool-workpiece interface. In this study, 20% of the heat generated at the flank face is assumed to stay on the tool side, whereas 80% of the heat is transferred to the workpiece. This ratio was found by experimental results.

2.1.4. Temperature Distribution in the Cutting Tool

In this study, the temperature distribution in the tool was calculated by using the Finite Difference Method. The temperatures on the rake and flank surface of the tool were analytically calculated using Equations (19) and (32), respectively. These temperatures were used as a boundary condition in the calculation of temperature inside the tool.

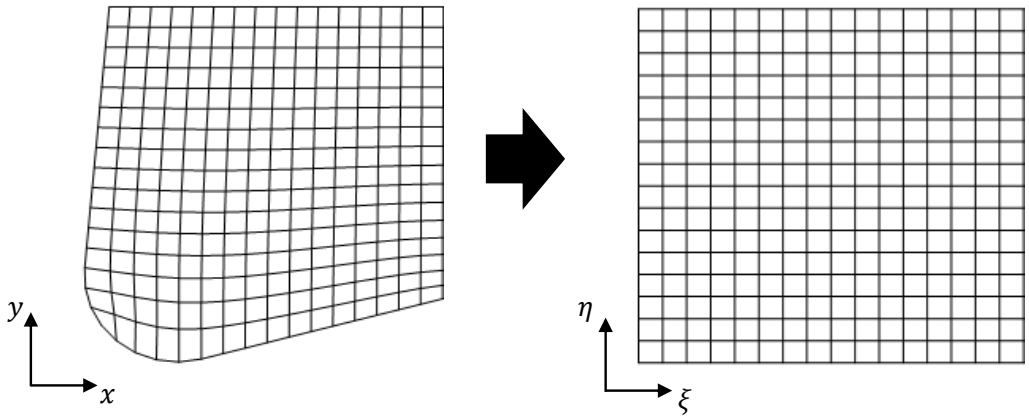

(a) (b)

Figure 4. (a) Physical and (b) computational domains.

The temperature distribution in the tool was obtained by solving the 2D steady state heat Equation below [98]:

$$\frac{\partial^2 T(x,y)}{\partial x^2}+\frac{\partial^2 T(x,y)}{\partial y^2}=0 \quad (33)$$

Due to the existence of a cutting-edge radius, the area to be considered in the calculations has a complex geometry. Therefore, unlike classical Finite Difference Methods, a structured grid generation method was used for the solution of this equation [98]. The

first step is determining the location of grid points inside the tool. An elliptic mesh generation method was used to generate a 2D grid in $x-y$ plane. The solution of a partial differential equation was used to relate the physical and computational domain. The transformation from the physical x, y coordinates to the computational ξ, η coordinates can be expressed as [98]:

$$\begin{aligned} \xi &\equiv \xi(x,y) \\ \eta &\equiv \eta(x,y) \end{aligned} \tag{34}$$

Transformation relations between x, y and ξ, η planes were determined with the numerical solution of elliptic partial differential equations below [98]:

$$\begin{aligned} \nabla^2\xi &= \frac{\partial^2\xi}{\partial x^2} + \frac{\partial^2\xi}{\partial y^2} = 0\,, \\ \nabla^2\eta &= \frac{\partial^2\eta}{\partial x^2} + \frac{\partial^2\eta}{\partial y^2} = 0 \end{aligned} \tag{35}$$

Using the chain rule of differentiation, the transformation relations can be obtained as [98]:

$$\begin{aligned} \frac{\partial^2}{\partial x^2} &= \frac{\partial^2}{\partial \xi^2}.\left(\frac{\partial \xi}{\partial x}\right)^2 + 2\frac{\partial^2}{\partial \xi \partial \eta}\left(\frac{\partial \xi}{\partial x}.\frac{\partial \eta}{\partial x}\right) + \frac{\partial^2}{\partial \eta^2}.\left(\frac{\partial \eta}{\partial x}\right)^2 \\ \frac{\partial^2}{\partial y^2} &= \frac{\partial^2}{\partial \xi^2}.\left(\frac{\partial \xi}{\partial y}\right)^2 + 2\frac{\partial^2}{\partial \xi\, \partial \eta}\left(\frac{\partial \xi}{\partial y}.\frac{\partial \eta}{\partial y}\right) + \frac{\partial^2}{\partial \eta^2}.\left(\frac{\partial \eta}{\partial y}\right)^2 \end{aligned} \tag{36}$$

where the subscripts show differentiation with respect to the considered variable. Then, the Laplace operator can be written as [98]:

$$\nabla^2 = \frac{\partial^2}{\partial \xi^2}\left(\left(\frac{\partial \xi}{\partial x}\right)^2 + \left(\frac{\partial \xi}{\partial y}\right)^2\right) + \frac{\partial^2}{\partial \eta^2}\left(\left(\frac{\partial \eta}{\partial x}\right)^2 + \left(\frac{\partial \eta}{\partial y}\right)^2\right) + 2\,\frac{\partial^2}{\partial \xi\, \partial \eta}\left(\frac{\partial \xi}{\partial x}.\frac{\partial \eta}{\partial x} + \frac{\partial \xi}{\partial y}.\frac{\partial \eta}{\partial y}\right) \tag{37}$$

Using Cramer's rule, the Laplace operator can be determined as [98]:

$$\begin{aligned} \nabla^2 = \frac{\partial^2}{\partial \xi^2}\left(\left(\frac{\partial \xi}{\partial x}\right)^2 + \left(\frac{\partial \xi}{\partial y}\right)^2\right) + 2\,\frac{\partial^2}{\partial \xi\, \partial \eta}\left(\frac{\partial \xi}{\partial x}.\frac{\partial \eta}{\partial x} + \frac{\partial \xi}{\partial y}.\frac{\partial \eta}{\partial y}\right) + \frac{\partial^2}{\partial \eta^2}\left(\left(\frac{\partial \eta}{\partial x}\right)^2 + \left(\frac{\partial \eta}{\partial y}\right)^2\right) \\ = J^2\left(\alpha\frac{\partial^2}{\partial \xi^2} - 2\beta\frac{\partial^2}{\partial \xi \partial \eta} + \gamma\frac{\partial^2}{\partial \eta^2}\right) \end{aligned} \tag{38}$$

where J is the Jacobian of transformation. Then, Equation (35) becomes:

$$\begin{aligned} \alpha'\frac{\partial^2 x}{\partial \xi^2} - 2\beta'\frac{\partial^2 x}{\partial \xi \partial \eta} + \gamma'\frac{\partial^2 x}{\partial \eta^2} = 0 \\ \alpha'\frac{\partial^2 y}{\partial \xi^2} - 2\beta'\frac{\partial^2 y}{\partial \xi \partial \eta} + \gamma'\frac{\partial^2 x}{\partial \eta^2} = 0 \end{aligned} \tag{39}$$

where the geometric coefficients α', β', and γ' can be expressed as:

$$\alpha' = \left(\frac{\partial x}{\partial \eta}\right)^2 + \left(\frac{\partial y}{\partial \eta}\right)^2$$
$$\beta' = \frac{\partial x}{\partial \xi}\frac{\partial x}{\partial \eta} + \frac{\partial y}{\partial \xi}\frac{\partial y}{\partial \eta} \tag{40}$$
$$\gamma' = \left(\frac{\partial x}{\partial \xi}\right)^2 + \left(\frac{\partial y}{\partial \xi}\right)^2$$

The location of the boundary points on the tool rake and flank faces were used as a boundary condition for solving Equation (39). The solution of this equation determines the values of the x, y coordinates at each ξ, η grid point in the computational domain. An iterative procedure is used in the solution of these equations. The iteration continues until the maximum difference between two successively calculated coordinates reaches a predefined tolerance value. After determining the correspondence between x, y and ξ, η coordinate values, the results can be transformed to the physical domain by:

$$x_{i,j} = \frac{1}{2(\alpha'_{i,j} + \gamma'_{i,j})}\Big[\alpha'_{i,j}(x_{i+1,j} + x_{i-1,j}) - \frac{\beta'_{i,j}}{2}(x_{i+1,j+1} - x_{i-1,j+1} - x_{i+1,j-1} + x_{i-1,j-1}) + \gamma'_{i,j}(x_{i,j+1} + x_{i,j-1})\Big] \tag{41}$$

$$y_{i,j} = \frac{1}{2(\alpha'_{i,j} + \gamma'_{i,j})}\Big[\alpha'_{i,j}(y_{i+1,j} + y_{i-1,j}) - \frac{\beta'_{i,j}}{2}(y_{i+1,j+1} - y_{i-1,j+1} - y_{i+1,j-1} + y_{i-1,j-1}) + \gamma'_{i,j}(y_{i,j+1} + y_{i,j-1})\Big] \tag{42}$$

Once the location of all grid points for the tool are known, the heat conduction Equation (33) should be also transformed from x, y to ξ, η coordinates of the computational domain as:

$$\alpha'\frac{\partial^2 T}{\partial \xi^2} - 2\beta'\frac{\partial^2 T}{\partial \xi \partial \eta} + \gamma'\frac{\partial^2 T}{\partial \eta^2} = 0 \tag{43}$$

The finite difference form of second order derivatives in Equation (43) for interior points can be written as:

$$\frac{\partial^2 T}{\partial \xi^2} = T_{i+1,j} - 2T_{i,j} + T_{i-1,j}$$

$$\frac{\partial^2 T}{\partial \eta^2} = T_{i,j+1} - 2T_{i,j} + T_{i,j-1} \tag{44}$$

$$\frac{\partial^2 T}{\partial \xi \partial \eta} = \frac{1}{4}\left(T_{i+1,j+1} - T_{i-1,j+1} - T_{i+1,j-1} + T_{i-1,j-1}\right)$$

Introducing Equations (44) into Equation (43), the following successive-substitution formula can be obtained as:

$$\begin{aligned}\alpha'_{i,j}\left(T_{i+1,j} - 2T_{i,j} + T_{i-1,j}\right) - \frac{\beta'_{i,j}}{2}\left(T_{i+1,j+1} - T_{i-1,j+1} - T_{i+1,j-1} + T_{i-1,j-1}\right) \\ + \gamma'_{i,j}\left(T_{i,j+1} - 2T_{i,j} + T_{i,j-1}\right) = 0\end{aligned} \tag{45}$$

Rearranging Equation (45) we will have:

$$\begin{aligned}T_{i,j} = \frac{1}{2\left(\alpha'_{i,j} + \gamma'_{i,j}\right)}\Bigg[\alpha'_{i,j}\left(T_{i+1,j} + T_{i-1,j}\right) \\ - \frac{\beta'_{i,j}}{2}\left(T_{i+1,j+1} - T_{i-1,j+1} - T_{i+1,j-1} + T_{i-1,j-1}\right) \\ + \gamma'_{i,j}\left(T_{i,j+1} + T_{i,j-1}\right)\Bigg]\end{aligned} \tag{46}$$

For the segments of rake and flank surfaces, which are not in contact with the chip or workpiece, the convection boundary condition is considered:

$$-k\frac{\partial T}{\partial n} = h(T - T_\infty) \tag{47}$$

where h is the heat convection coefficient. Hence, the finite difference form of the convection boundary condition can be derived as:

$$\frac{\alpha'_{i,j}}{2}\left(-3T_{i,j} + 4T_{i+1,j} - T_{i+2,j}\right) - \frac{\beta'_{i,j}}{2}\left(T_{i,j+1} - T_{i,j-1}\right) = \frac{h}{k}J_{i,j}\sqrt{\alpha'_{i,j}}\left(T_{i,j} - T_\infty\right) \tag{48}$$

$$\frac{\gamma'_{i,j}}{2}\left(T_{i+1,j} - T_{i-1,j}\right) - \frac{\beta'_{i,j}}{2}\left(-3T_{i,j} + 4T_{i,j+1} - T_{i,j+2}\right) = \frac{h}{k}J_{i,j}\sqrt{\gamma'_{i,j}}\left(T_{i,j} - T_\infty\right) \tag{49}$$

The faces, which are located far from the cutting area, are considered to have room temperature, T_∞.

2.1.5. Solution Procedure

The simulations starts with the calculation of the temperature and shear stress at the exit of the primary shear zone by Equations (2) and (7). Then the normal and shear stress distributions in the secondary and the third deformation zones should be determined by

Equations (8) and (9). After calculating the lengths of the sticking and sliding contacts with Equations (10), (11), (21) and (24), the heat generation can be obtained by Equations (19) and (32).

In order to calculate the temperature distribution within the tool, the number of elements and their locations at the tool boundaries must be determined. Then the interior grid points are set by an iterative calculation with the use of structured mesh generation method. A moderate mesh size of 30×30 mm is used during the analysis, which results in around 10,000 elements on a typical tool size. The solution time of such a simulation is around 2 minutes on a moderate Laptop. In the next step, boundary conditions should be applied to the tool model. Analytical relations are provided for the calculation of temperature in the chip and workpiece. Considering the steady-state condition, the temperature of tool and chip at their interface is equal for both sides. The same rule is applicable to the tool-workpiece interface in the third deformation zone. Therefore, the temperature of tool-chip and tool-workpiece interfaces can be used as boundary conditions for the rake and flank faces, respectively. For the boundary points of tool, which are not in contact area, the convection boundary condition should be applied. For the faces located far from the cutting area, room temperature is considered.

Using boundary conditions for corresponding points and Equation (46) for the internal points of tool, a system of equations is obtained which can be illustrated as:

$$[C_{tool}][T_{tool}] = [A_{tool}] \tag{50}$$

where C_{tool} is coefficient matrix; T_{tool} is the tool temperature array; and A_{tool} is the heat source array. The open form of these matrices can be written as:

$$\begin{bmatrix} [C_{11}]_{1\times mn} \\ [C_{12}]_{1\times mn} \\ [C_{13}]_{1\times mn} \\ \vdots \\ [C_{1n}]_{1\times mn} \\ [C_{21}]_{1\times mn} \\ \vdots \\ [C_{m,n-2}]_{1\times mn} \\ [C_{m,n-1}]_{1\times mn} \\ [C_{m,n}]_{1\times mn} \end{bmatrix}_{mn\times mn} \times \begin{bmatrix} T_{11} \\ T_{12} \\ T_{13} \\ \vdots \\ T_{1n} \\ T_{21} \\ \vdots \\ T_{m,n-2} \\ T_{m,n-1} \\ T_{mn} \end{bmatrix}_{mn\times 1} = \begin{bmatrix} A_{11} \\ A_{12} \\ A_{13} \\ \vdots \\ A_{1n} \\ A_{21} \\ \vdots \\ A_{m,n-2} \\ A_{m,n-1} \\ A_{mn} \end{bmatrix}_{mn\times 1} \tag{51}$$

where T_{ij} is the temperature of tool grid points. Solving Equation (50), the temperature distribution for all the grid points in the tool can be determined. Figure 6 shows solution

procedure in a flow chart.

In order to define the C_{ij} and A_{ij} matrices, for any point numbered with ij a term is introduced as:

$$ps = (i-1)n + j; \tag{52}$$

where i and j show the row and column number of any grid point which are shown in Figure 5; n is the total number of points on AC line; and ps is the grid point number allocated to any ij point. The total area is divided into different segments as AB, BC, AD, DE, EF, CF and internal points. C_{ij} and A_{ij} matrices for these segments are described with details in the following.

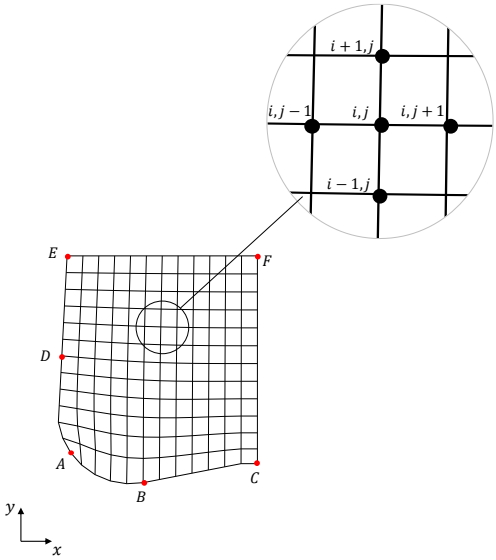

Figure 5. Critical points used for cutting tool in the finite difference calculations.

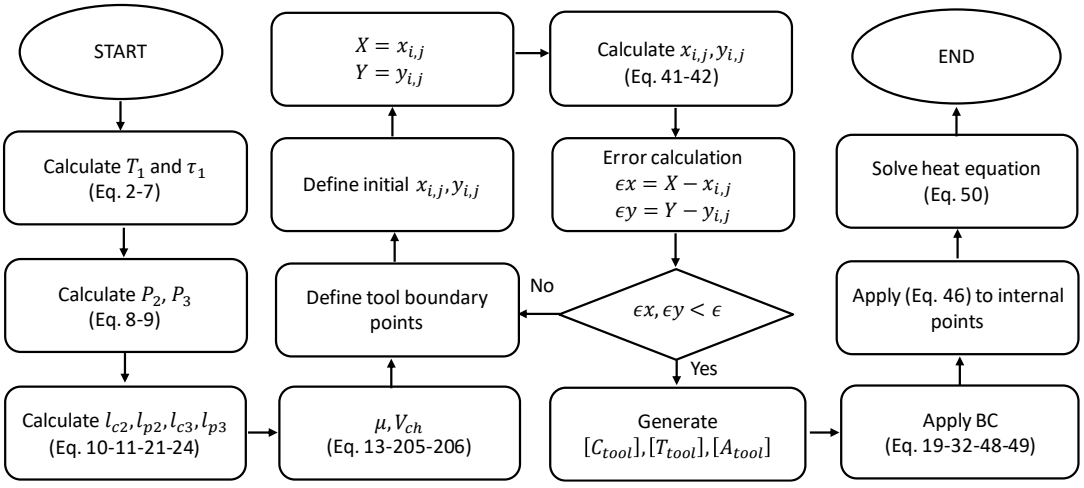

Figure 6. Flow chart of the proposed solution procedure.

2.1.5.1. Contact area on the rake face (AD)

The temperature of this area is calculated with Equations (19). The matrices are described as:

$$C_{ij} = [0 \quad \dots \quad \underset{\downarrow}{ps} \quad \dots \quad 0]_{1\times mn} \qquad (53)$$
$$A_{ij} = T_{ij} \ \ (calculated\ with\ equation\ (19))$$

2.1.5.2. Contact area on the flank face (AB)

The matrices for the flank contact area can be written as:

$$C_{ij} = [0 \quad \dots \quad \underset{\downarrow}{ps} \quad \dots \quad 0]_{1\times mn} \qquad (54)$$
$$A_{ij} = T_{ij} \ \ (calculated\ with\ equation (32))$$

2.1.5.3. Rake face points with the convection boundary condition (DE)

For the rake face points with the convection boundary condition, the matrices are formed as:

$$C_{ij} = [0 \quad \cdots \quad \underset{\downarrow}{(ps-n)} \quad \cdots \quad \underset{\downarrow}{(ps)} \quad \underset{\downarrow}{(ps+1)} \quad \underset{\downarrow}{(ps+2)} \quad \cdots \quad \underset{\downarrow}{(ps+n)} \quad \cdots \quad 0] \qquad (55)$$
$$C_{ij} = [0 \quad \cdots \quad -\frac{1}{2}\beta'_{ij} \quad \cdots \quad \frac{3}{2}\alpha'_{ij} + \frac{h}{k}J_{ij}\sqrt{\alpha'_{ij}} \quad -2\alpha_{ij} \quad \frac{1}{2}\alpha'_{ij} \quad \cdots \quad \frac{1}{2}\beta'_{ij} \quad \cdots \quad 0]$$
$$A_{ij} = \frac{h}{k}J_{ij}T_{room}\sqrt{\alpha'_{ij}}$$

2.1.5.4. Flank face points with the convection boundary condition (BC)

For the flank face points with the convection boundary condition, the corresponding matrices are formed as:

$$C_{ij} = [0 \quad \cdots \quad \underset{\downarrow}{(ps-1)} \quad \underset{\downarrow}{(ps)} \quad \underset{\downarrow}{(ps+1)} \quad \underset{\downarrow}{(ps+n)} \quad \underset{\downarrow}{(ps+2n)} \quad \cdots \quad 0] \qquad (56)$$
$$C_{ij} = [0 \quad \cdots \quad -\frac{1}{2}\beta'_{ij} \quad \frac{3}{2}\gamma'_{ij} + \frac{h}{k}J_{ij}\sqrt{\gamma'_{ij}} \quad \frac{1}{2}\beta'_{ij} \quad \cdots \quad -2\gamma'_{ij} \quad \cdots \quad \frac{1}{2}\gamma'_{ij} \quad \cdots \quad 0]$$
$$A_{ij} = \frac{h}{k}J_{ij}T_{room}\sqrt{\gamma'_{ij}}$$

2.1.5.5. Faces located far from cutting area (CF, EF)

The free surfaces of the tool that are located far from the cutting zone are considered to have room temperature. Therefore, the matrices for these points can be written as:

$$C_{ij} = [0 \quad \dots \quad \underset{\downarrow}{ps} \quad \dots \quad 0]_{1\times mn} \qquad (57)$$
$$A_{ij} = T_{\infty}$$

2.1.5.6. Internal points

The matrix form for the internal points can be written as:

$$C_{ij} = [\cdots \underset{\downarrow}{(ps-n-1)} \quad -\frac{1}{2}\beta'_{ij} \quad \underset{\downarrow}{(ps-n)} \quad \gamma'_{ij} \quad \underset{\downarrow}{(ps-n+1)} \quad \frac{1}{2}\beta'_{ij} \quad \cdots \quad \underset{\downarrow}{(ps-1)} \quad \alpha'_{ij} \quad \underset{\downarrow}{(ps)} \quad -2(\alpha'_{ij}+\gamma'_{ij}) \quad \underset{\downarrow}{(ps+} \quad \alpha'_{ij} \quad \underset{\downarrow}{(ps+n-1)} \quad \frac{1}{2}\beta'_{ij} \quad \underset{\downarrow}{(ps+n)} \quad \gamma'_{ij} \quad \underset{\downarrow}{(ps+n+1)} \quad -\frac{1}{2}\beta'_{ij} \quad \cdots \quad 0] \tag{58}$$

$$A_{ij} = 0$$

2.2. Temperature Distribution in Oblique Cutting

2.2.1. Heat Generation in the First Deformation Zone

The primary deformation zone model is based on the model developed by Molinari and Dudzinski [90]. This model was later modified by Budak and Ozlu [99] to be used in oblique cutting modeling. In order to define the material behavior, Johnson-Cook was chosen as the constitutive equation:

$$\tau = \frac{1}{\sqrt{3}}\left[A + B\left(\frac{\gamma}{\sqrt{3}}\right)^{n}\right]\left[1 + \ln\left(\frac{\dot{\gamma}}{\dot{\gamma}_0}\right)^{m}\right]\left[1 - \left(\frac{T_w - T_r}{T_m - T_r}\right)^{\upsilon}\right] \tag{59}$$

where τ is the shear stress; γ is the shear strain; $\dot{\gamma}$ is the shear strain rate; $\dot{\gamma}_0$ is the reference shear strain rate; T_w is the absolute temperature of workpiece; T_r is the reference temperature; T_m is the melting temperature of workpiece; and $A, B, n, m,$ and υ represent the material constants.

In the primary shear zone model it is assumed that the shear band has h_s thickness. All the deformations are occurred inside the shear band which means no deformation occurs before and after this band. The material enters this band with shear stress τ_0 and after being deformed under uniform pressure, exits the region with shear stress τ_1. Moreover, the heat generated by the secondary and third deformation zones do not substantially affect the hypothesis of one-dimensional distribution of the shear strain and of the temperature in the primary shear zone [91].

The shear stresses τ_0 and τ_1 can be calculated iteratively considering the conservation of momentum with below equation [99]:

$$\tau_1 = \rho(V_c \sin \phi_n \cos i)^2 \gamma_1 + \tau_0 \quad (60)$$

where, ρ is the density of the workpiece material, V_c is the cutting speed, i is the inclination angle, ϕ_n is the shear angle in the normal plane, and γ_1 is the shear strain at the exit of the shear band.

An important issue in the oblique cutting modeling is the definition of the shear angle. Due to oblique cutting conditions, the shear angle in the plane that is normal to the inclined shear band, was used as the shear angle. The inclination of shear band with respect to cutting edge radius is equal to the shear flow angle, η_s.

The temperature generated at the exit of the primary deformation zone can be calculated under adiabatic conditions and using the conservation of energy:

$$T_1 = T_w + \frac{\chi}{\rho c}\left(\rho V_c^2 \sin^2 \phi_n \cos^2 i \frac{{\gamma_1}^2}{2} + \tau_0 \gamma\right) \quad (61)$$

where T_1 is the temperature at the exit of shear band; χ is the fraction of the work converted into heat; and c is the heat capacity. In previous experimental studies, χ has been found to be 0.9 for metals [93].

The shear stress at the start of the shear band, τ_0, can be calculated iteratively by using below equation:

$$\frac{d\gamma}{dy} = \frac{d\gamma}{dt}\frac{dt}{dy} = \frac{\dot{\gamma}}{V_c \sin \emptyset_n} \quad (62)$$

The boundary conditions for Equation (4) are:

$$T = T_w \qquad @\ y = 0 \quad (63)$$

$$\gamma = 0 \qquad @y = 0 \quad (64)$$

$$\gamma = \gamma_1 = tan(\phi_n - \alpha) + \frac{1}{tan\, \phi_n} \qquad @y = h_s \quad (65)$$

In these equations, α is the rake angle, the y axis is the axis along the shear band thickness, and h_s is the thickness of shear band. τ_0 is obtained by solving equations (59) and (4), iteratively. The shear stress at the exit of the first deformation zone, τ_1 can be calculated by equation (2), and the resulting temperature can be determined by equation (3) [21].

2.2.2. Heat Generation in the Second Deformation Zone

During the cutting process, a high normal stress is exerted on the tool rake face by the chip. ‘Therefore, a sticking friction condition occurs between the chip and the rake face

of the tool. As the normal stress value on the chip and rake face decreases, the friction condition turns into sliding. This stress decreases continuously and the point with zero stress is the end of contact length on the rake face. The total length of contact area between the chip and the tool is represented by l_{c2} which is shown in Figure 7.

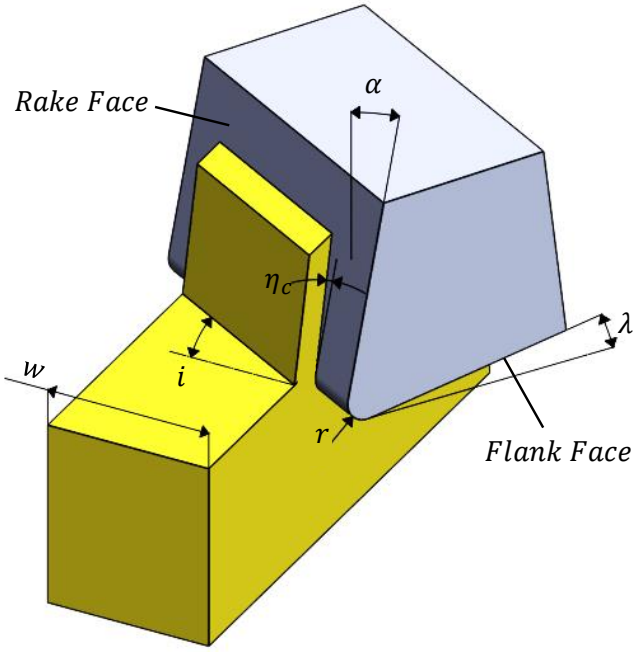

Figure 7. The oblique cutting process.

In the modeling of the second deformation zone, it is assumed that the heat transfer in the chip flow direction is negligible due to the high speed of the chip and it is not included in the calculations [21]. In order to model the rake face contact, dual-zone model is enhanced in the calculations [94]. The heat transfer is considered to reach the steady-state condition which is time-independent.

The normal force on the tool rake face, N, can be calculated as follows, assuming that the normal pressure distribution varies exponentially:

$$N = \int_0^{l_{c2}} P_0 \left(1 - \frac{x_2}{l_{c2}}\right)^{\zeta} w_c dx = P_0 \frac{w_c l_{c2}}{\zeta+1} = P_0 \frac{w l_{c2}}{\zeta+1} \frac{\cos \eta_c}{\cos i} \tag{66}$$

where P_0 is the normal pressure on the tool tip, ζ is the control parameter for pressure distribution, η_c is the chip flow angle, i is the inclination angle, l_{c2} is the total rake contact length and w is the depth of cut. P_0 can be obtained as:

$$P_0 = \tau_1 \frac{h_0(\zeta+1)}{l_{c2}} \frac{\cos\eta_s \cos\beta_n}{\sin\phi_n \cos\eta_c \cos(\phi_n+\beta_n-\alpha_n)} \quad (67)$$

where $h_0$is the uncut chip thickness, β_n is the normal friction angle, α_n is the normal rake angle, and η_s is the shear flow angle. Normal friction angle, β_n, is defined as:

$$\beta_n = \tan^{-1}(\mu_a \cos\eta_c) \quad (68)$$

where μ_a is the apparent friction coefficient.

Once the pressure distribution is determined, the total contact length can be calculated using the moment equilibrium at the tool tip. By equating the moment at the tool tip due to shear force and moment generated by normal pressure of the rake face, the total contact length equation can be derived as:

$$l_{c2} = \frac{h_0(\zeta+2)}{2} \frac{\sin(\phi_n+\beta_n-\alpha_n)}{\sin\phi_n \cos\beta_n \cos\eta_c} \quad (69)$$

At the end of sticking contact area, the normal and shear stress become equal. Considering this fact, the sticking contact length can be calculated as:

$$l_{p2} = l_{c2}\left(1 - \left(\frac{\tau_1}{P_0\mu_a}\right)^{\frac{1}{\zeta}}\right) \quad (70)$$

To determine the shear and chip flow angles, it can be assumed that the chip velocity and friction are coincident. The same assumption is applicable for the shear force and shear velocity. As a result, following relations can be found [100]:

$$\tan(\phi_n + \beta_n) = \frac{\tan i \cos\alpha_n}{\tan\eta_c - \sin\alpha_n \tan i} \quad (71)$$

$$\tan\eta_s = (\tan i \cos(\phi_n - \alpha_n) - \tan\eta_c \sin\phi_n)/\cos\alpha_n \quad (72)$$

For determining the shear angle, ϕ_n, cutting power is calculated for a range of shear angles and the angle that corresponds to the minimum cutting power is chosen as the shear angle.

In order to calculate the heat generation in the secondary deformation zone, the two-dimensional heat equation was solved:

$$a\frac{\partial^2 T(x_2,y_2)}{\partial y_2^2} = \frac{V_{ch}\partial T(x_2,y_2)}{\partial x_2} \quad (73)$$

where $a = k/\rho c$ is the thermal diffusivity; k is the thermal conductivity; and c is specific heat capacity. x_2, y_2 presents the coordinates in the second deformation zone that are shown in Figure 8. V_{ch} is the chip velocity that can be formulated as:

$$V_{ch} = \frac{V_c \sin\phi_n \cos i}{\cos(\phi_n - \alpha_n)\cos(\eta_c)} \tag{74}$$

The temperature at the end of the primary deformation zone, T_1, is used as a boundary condition in solving the heat equation for second and third deformation zone. Moreover, the temperature of the free surface of the chip is accepted as T_1. Therefore, the boundary conditions in solving Equation (12) are:

$$\begin{aligned} &T(0, y_2) = T_1 && x_2 = 0\,,\ y_2 \geq 0 \\ &\lim_{y_2 \to \infty} T(x_2, y_2) = T_1 && x_2 \geq 0 \\ &-k\frac{\partial T(x_2,0)}{\partial y_2} = q_2(x_2) && x_2 \geq 0 \end{aligned} \tag{75}$$

where q_2 is the frictional heat flux in second deformation zone. The Laplace transformation was used [97] in determining the analytical solution of these equations. Then Equations (14) can be transformed as follows:

$$\begin{aligned} &\bar{T}(s, y_2) = \int_0^{\infty} T(x_2, y_2) e^{-sx_2} dx_2 \\ &\bar{T}(s, \infty) = \frac{T_1}{s} \\ &-k\frac{d\bar{T}(s, y_2)}{dy_2} = Q(s) \end{aligned} \tag{76}$$

Here, $Q(s)$ is the representation of $q_2(x_2)$ after Laplace transformation. Applying the Laplace transformation on Equation (12), it can be written as:

$$a\frac{d^2\bar{T}(s, y_2)}{dy_2{}^2} = V_{ch}(s\bar{T}(s, y_2) - T_1) \tag{77}$$

Reverse Laplace Transform and convolution property was applied to the equations to determine the temperature distribution inside the chip as:

$$T(x_2, y_2) = \frac{1}{k}\sqrt{\frac{a}{\pi V_{ch}}}\int_0^{x_2} q_2(x_2 - u)\frac{1}{\sqrt{u}} e^{\left(-\frac{V_{ch} y_2^2}{4au}\right)} du + T_1 \tag{78}$$

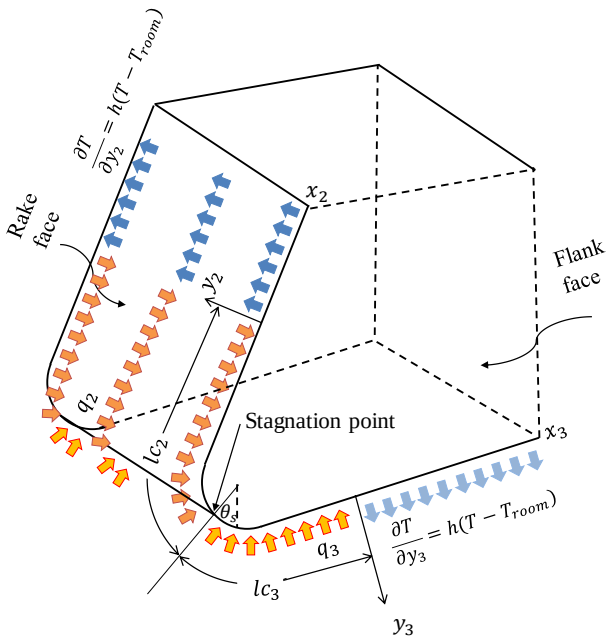

Figure 8. Boundary conditions applied in the model for oblique cutting.

Due to the high normal pressure at the exit of shear band and near the tool tip, there exists a sticking region. With the decrease of normal pressure on the chip-tool contact area, friction will change to sliding. Therefore, the contact between chip and tool rake face can be represented with dual-zone contact model. The heat flux for the second deformation zone can be written as:

$$q_2(x_2) = \begin{cases} \tau_1 V_{ch} & x_2 \le l_{p2} \\ \mu_{sl} V_{ch} P_0 \left(1 - \frac{x_2}{l_{c2}}\right)^{\zeta} & l_{p2} \le x_2 \le l_{c2} \\ 0 & x_2 \ge l_{c2} \end{cases} \tag{79}$$

where x_2 is the distance from tool tip on the rake face, μ_{sl} is the sliding friction coefficient and it is calculated using the equations provided by Ozlu et al. [87]. These equations are calibrated based on orthogonal tube cutting tests. Therefore, the temperature at the tool-chip interface ($y_2 = 0$) can be written as:

$$T(x_2, 0) = \frac{1}{k}\sqrt{\frac{a}{\pi V_{ch}}}\left(\int_0^{l_{p2}} \tau_1 V_{ch} \frac{1}{\sqrt{u}} du + \int_{l_{p2}}^{l_{c2}} \mu_{sl} V_{ch} P_0 \left(1 - \frac{x_2 - u}{l_{c2}}\right)^{\zeta} \frac{1}{\sqrt{u}} du\right) + T_1 \tag{80}$$

The heat partition fraction along the contact length is an important issue in the modeling of cutting temperature. In this study, a non-uniform distribution of the heat partition ratio, which was suggested by Komanduri and Hou [27], was used for the tool-chip interface. The function for tool and chip side can be described as:

$$B_{i,chip} = \left(B_{chip} - \Delta B\right) + 2\Delta B\left(\frac{l_{c2}-x_2}{l_{c2}}\right)^e$$
$$B_{i,tool} = \left(B_{tool} + \Delta B\right) - 2\Delta B\left(\frac{l_{c2}-x_2}{l_{c2}}\right)^e \quad (81)$$

where $B_{i,chip} + B_{i,tool} = 1$ for any point on the tool-chip interface. B_{chip}, B_{tool}, ΔB and e are the coefficients, which are calibrated considering equal temperature at the tool-chip interface. These coefficients are obtained experimentally.

2.2.3. Heat Generation in the Third Deformation Zone

The reason for the existence of third deformation zone is the cutting-edge radius. The material below the stagnation point (Figure 8) experiences ploughing and recovery. Therefore the normal pressure distribution on the flank face is modeled with an increasing-decreasing equation [86]. In this study, the force and heat model developed for orthogonal cutting have been modified and adapted to oblique cutting conditions. It is assumed that workpiece has a fully-elastic recovery after passing the third deformation zone [86]. Similar to the rake contact, sticking and sliding regions are considered to exist in this area and dual-zone model is used to simulate the flank contact. Due to the high cutting speed, the heat transfer in the workpiece movement direction is neglected and problem is considered to be steady-state.

The total contact length on the flank face is identified by using the fully elastic recovery assumption [86]. The third deformation zone is divided into three regions, which are illustrated in Fig . Considering the inclination angle, the total contact length on the flank face can be calculated as:

$$l_{c3} = l_1 + l_2 + l_3$$
$$l_1 = \theta . r / \cos i$$
$$l_2 = \lambda . r / \cos i \quad (82)$$
$$l_3 = r\frac{(\cos\lambda - \cos\theta)}{\sin\lambda \cos i}$$

where θ is the stagnation angle; and r is the cutting-edge radius. In order to calculate the stagnation angle the experimental procedure proposed by Budak et al. [86] was used.

There are different types of relationships that explain the normal pressure on the flank

face. Based on the comparisons conducted by Budak et al. [86], between predicted and measured forces, an increasing-decreasing trend was found out to describe the normal pressure variation on the flank contact most accurately. This result can be justified considering the geometry of third zone in which the material is first pressurized and then it has a relaxation phase. Then, the normal pressure distribution on the flank face can be described as:

$$P_3(x_3) = a'x_3^2 + b'x_3 + c'$$

$$a' = \frac{P_0}{l_{c3}(2l_3 - l_{c3})}$$
$$b' = -2P_0 a' l_1 \tag{83}$$

$$c' = P_0$$

where P_0 is the normal pressure at the stagnation point; and x_3 is the distance from tool tip on the flank face. A complex friction model is considered for describing the flank contact. The region with high normal pressure is modeled as sticking and when the normal pressure begins to decrease, contact is assumed to be sliding. Using the Coulomb friction law along the sliding region, the following can be written:

$$\tau_{(x_3)} = \mu_{sl} P_3 = \mu_{sl}(a'x_3^2 + b'x_3 + c') \tag{84}$$

It is assumed that the μ_{sl} on the flank face is equal to the sliding friction coefficient on the rake face. Considering the equality of tangential and shear yield stresses at the end of sticking region, the length of sticking contact length can be calculated as:

$$l_{p3} = \frac{-b' + \sqrt{b'^2 - 4a'(c' - \frac{\tau_1}{\mu_{sl}})}}{2a'} \tag{85}$$

Similar to the second deformation zone, two-dimensional heat equation was used in the calculation of the heat generation in third deformation zone [21]:

$$a\frac{\partial^2 T(x_3, y_3)}{\partial y_3^2} = \frac{V_c \partial T(x_3, y_3)}{\partial x_3} \tag{86}$$

In order to solve this equation below boundary conditions can be considered:

$$T(0, y_3) = T_1 \qquad x_3 = 0\ ,\ y_3 \geq 0$$

$$\lim_{y_3 \to d} T(x_3, y_3) = T_\infty \qquad x_3 \geq 0 \tag{87}$$

$$-k\frac{\partial T(x_3, 0)}{\partial y_3} = q_3(x_3) \qquad x_3 \geq 0$$

where T_∞ is the room temperature; and d is the workpiece diameter.

For solving Equation (25) the Laplace transformation is applied to, Equations (25)-(26):

$$a\frac{d^2\bar{T}(s,y_3)}{dy_3{}^2} = V_c(s\bar{T}(s,y_3) - T_1) \tag{88}$$

$$\bar{T}(s,y_3) = \int_0^\infty T(x_3,y_3)e^{-sx_3}dx_3$$

$$\bar{T}(s,\infty) = \frac{T_1}{s} \tag{89}$$

$$-k\frac{d\bar{T}(s,y_3)}{dy_3} = Q(s)$$

where $Q(s)$ is the Laplace transform of the heat flux q_3. Considering all these equations, and using Reverse Laplace Transform, the equation for expressing the temperature distribution in the workpiece can be written as:

$$T(x_3,y_3) = \frac{1}{k}\sqrt{\frac{a}{\pi V_c}}\int_0^{x_3} q_3(x_3-u)\frac{1}{\sqrt{u}}e^{\left(-\frac{V_c y_3^2}{4au}\right)}du + \left(\frac{T_\infty - T_1}{d}\right)(y_3) + T_1 \tag{90}$$

The heat flux q_3 can be described as:

$$q_3(x_3) = \begin{cases} \tau_1 V_i & x_3 \le l_{p3} \\ \mu_{sl}(a'x_3^2 + b'x_3 + c')V_i & l_{p3} \le x_3 \le l_{c3} \\ 0 & x_3 \ge l_{c3} \end{cases} \tag{91}$$

where V_i is the local velocity along the flank contact. By applying Equation (31) to Equation (29), the temperature distribution in the tool-workpiece interface ($y_3 = 0$) can be determined as:

$$T(x_3,0) = \frac{1}{k}\sqrt{\frac{a}{\pi V_c}}\left(\int_0^{l_{p3}} \tau_1 V_i \frac{1}{\sqrt{u}}du + \int_{l_{p3}}^{l_{c3}} \mu_{sl}(a'x_3^2 + b'x_3 + c')V_i\frac{1}{\sqrt{u}}du\right) \tag{92}$$

2.2.4. Temperature Distribution in the Cutting Tool

As described in the previous sections, the temperature in the tool-chip and tool-workpiece contact areas are determined analytically. The temperature distribution in the tool is calculated by using the Finite Difference Method. The analytically calculated temperatures at the rake and flank contacts were used as a boundary condition in the calculation of temperature inside the tool.

The temperature distribution in the tool was obtained by solving the 3D steady state heat Equation below:

$$\frac{\partial^2 T(x,y,z)}{\partial x^2} + \frac{\partial^2 T(x,y,z)}{\partial y^2} + \frac{\partial^2 T(x,y,z)}{\partial z^2} = 0 \tag{93}$$

The existence of the cutting-edge radius makes the geometry of the problem complex. Therefore, classical Finite Difference Methods are not able to solve the problem. In this study, the 2D structured grid generation method is modified to be used in oblique cutting simulations. The first step is determining the location of grid points inside tool, chip and workpiece. In this study, a 2D grid is constructed in $x-y$ plane with the use of elliptic grid generation method and these grids are distributed in z direction with equal intervals. The solution of a partial differential equation is used to relate the physical and computational domain. The transformation from the physical x, y coordinates to the computational ξ, η coordinates can be expressed as

$$\begin{aligned} \xi &\equiv \xi(x,y) \\ \eta &\equiv \eta(x,y) \end{aligned} \tag{94}$$

Using the numerical solution of elliptic partial differential equations, transformation relations between x, y and ξ, η planes can be determined as:

$$\begin{aligned} \nabla^2 \xi &= \frac{\partial^2 \xi}{\partial x^2} + \frac{\partial^2 \xi}{\partial y^2} = 0\,, \\ \nabla^2 \eta &= \frac{\partial^2 \eta}{\partial x^2} + \frac{\partial^2 \eta}{\partial y^2} = 0 \end{aligned} \tag{95}$$

Using the chain rule of differentiation and Cramer's rule Equation (35) becomes:

$$\begin{aligned} \alpha' \frac{\partial^2 x}{\partial \xi^2} - 2\beta' \frac{\partial^2 x}{\partial \xi \partial \eta} + \gamma' \frac{\partial^2 x}{\partial \eta^2} &= 0 \\ \alpha' \frac{\partial^2 y}{\partial \xi^2} - 2\beta' \frac{\partial^2 y}{\partial \xi \partial \eta} + \gamma' \frac{\partial^2 x}{\partial \eta^2} &= 0 \end{aligned} \tag{96}$$

where α', β', γ' are some geometric coefficients. The location of the boundary points on the tool faces were used as a boundary condition for solving Equation (39). Solving Equation (39) iteratively, the x, y coordinates at each ξ, η grid point in the computational domain can be obtained. The iteration continues until the maximum difference between two successively calculated coordinates reaches a predefined tolerance value. Then, the generated grids are distributed in z direction with equal intervals to develop a 3D grid.

After determining the location of all grid points for tool, chip and workpiece the heat conduction equation (33) should be transformed from x, y, z to ξ, η, ϑ coordinates of the computational domain as:

$$\frac{\partial^2 T}{\partial \xi^2}\left({\xi_x}^2+{\xi_y}^2+{\xi_z}^2\right)+\frac{\partial^2 T}{\partial \eta^2}\left({\eta_x}^2+{\eta_y}^2+{\eta_z}^2\right)+\frac{\partial^2 T}{\partial \vartheta^2}\left({\vartheta_x}^2+{\vartheta_y}^2+{\vartheta_z}^2\right)+$$
$$2\ \frac{\partial^2 T}{\partial \xi\ \partial \eta}\left(\xi_x\ .\ \eta_x+\xi_y\ .\ \eta_y+\xi_z\ .\ \eta_z\right)+2\ \frac{\partial^2 T}{\partial \xi\ \partial \vartheta}\left(\xi_x\ .\ \vartheta_x+\xi_y\ .\ \vartheta_y+\xi_z\ .\ \vartheta_z\right)+ \quad (97)$$
$$2\ \frac{\partial^2 T}{\partial \eta\ \partial \vartheta}\left(\eta_x\ .\ \vartheta_x+\ \eta_y\ .\ \vartheta_y+\eta_z\ .\vartheta_z\right)=0$$

The finite difference form of second order derivatives in the equation (97) for interior points can be written as:

$$\frac{\partial^2 T}{\partial \xi^2}=T_{i+1,j,k}-2T_{i,j,k}+T_{i-1,j,k}$$
$$\frac{\partial^2 T}{\partial \eta^2}=T_{i,j+1,k}-2T_{i,j,k}+T_{i,j-1,k}$$
$$\frac{\partial^2 T}{\partial \vartheta^2}=T_{i,j,k+1}-2T_{i,j,k}+T_{i,j,k-1}$$
$$\frac{\partial^2 T}{\partial \xi \partial \eta}=\frac{1}{4}\left(T_{i+1,j+1,k}-T_{i-1,j+1,k}-T_{i+1,j-1,k}+T_{i-1,j-1,k}\right) \quad (45)$$
$$\frac{\partial^2 T}{\partial \xi \partial \vartheta}=\frac{1}{4}\left(T_{i+1,j,k+1}-T_{i-1,j,k+1}-T_{i+1,j,k-1}+T_{i-1,j,k-1}\right)$$
$$\frac{\partial^2 T}{\partial \eta \partial \vartheta}=\frac{1}{4}\left(T_{i,j+1,k+1}-T_{i,j-1,k+1}-T_{i,j+1,k-1}+T_{i,j-1,k-1}\right)$$

Due to the existence of inclination angle and chip flow angle in oblique cutting, the grid points on tool-chip interface on the tool and chip sides are not coincident (Figure 9). It also happens for the grids of tool and workpiece at flank contact area. Therefore, the temperature of any point on rake and flank contact area is considered equal to the temperature of closest point on chip and workpiece, respectively.

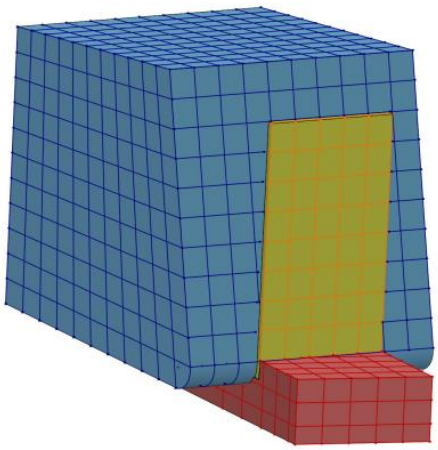

Figure 9. Grid points for tool, chip and workpiece.

For the segments of rake and flank surfaces, which are not in contact with the chip or workpiece, the convection boundary condition is considered:

$$-k\frac{\partial T}{\partial n} = h(T - T_{\infty}) \tag{98}$$

where h is the heat convection coefficient and T_{∞} is the room temperature. The faces, which are located far from the cutting area, are considered to have room temperature, T_{∞}.

2.2.5. Solution Procedure

The solution procedure of the proposed model is described in this section. The simulations starts with the calculation of the temperature and shear stress at the exit of the primary shear zone by Equations (60) and (61). Then the normal and shear stress distributions in the secondary and the third deformation zones should be determined by Equations (66) and (83). After calculating the lengths of the sticking and sliding contacts with Equations (69), (70), (82), and (85) the heat generation can be obtained by Equations (72) and (91). In the next step, the number of elements and their locations at the tool boundaries must be selected. Then the grids inside the cutting tool can be generated iteratively with the use of structured mesh generation method. In order to decrease the calculation time without reducing the accuracy, the grids are smaller in the areas near cutting edge and they get larger in areas which are far from cutting zone. The average mesh size of 50 mm x 50 mm is used during the analysis, which results in around 500,000 elements on a typical tool size. The solution time of such a simulation is around 10 minutes on a moderate Laptop. In the next step, boundary conditions should be applied to the tool model. Analytical relations are provided for the calculation of temperature in the chip and workpiece. Considering the steady-state condition, the temperature of tool and chip at their interface is equal for both sides. The same rule is applicable to the tool-workpiece interface in the third deformation zone. Therefore, the temperature of tool-chip and tool-workpiece interfaces can be used as boundary conditions for the rake and flank faces, respectively. For the boundary points of tool, which are not in contact area, the convection boundary condition should be applied. For the faces located far from the cutting area, room temperature is considered.

2.3. Temperature Distribution in Turning

In this section, the heat model developed for turning operation has been developed to include the effect of each deformation zone. Heat generation and temperature calculation in each zone are described in detail below.

2.3.1. Chip Thickness Model

The existence of nose radius in the turning operation makes the modeling process more complex due to two reasons: First reason is the change of uncut chip area along the nose radius. Second reason is the need to calculate local cutting angles on any point on the nose radius.

In general, based on the depth of cut, w_c, uncut chip area may involve two regions (Figure 10): first region is a parallelogram and the second region is the area enclosed by two arcs and a line. In the case that w_c is smaller than the nose height, w_n, the chip area would involve only the second region.

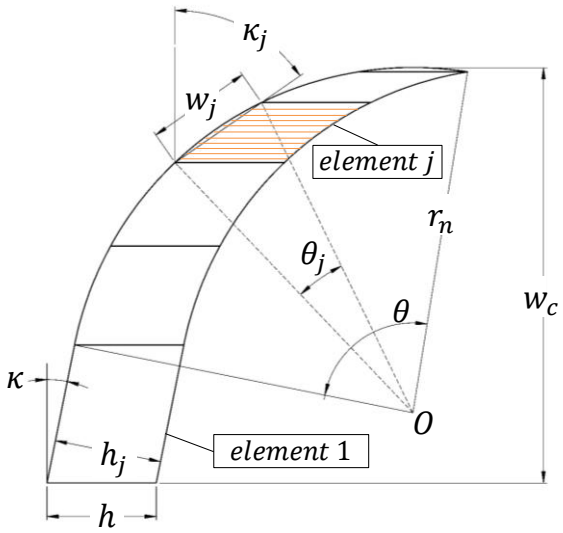

Figure 10. The uncut chip area in turning.

In order to calculate local angles along second region, it is divided to many parallelograms and 1st region is considered as one element (Figure 11).

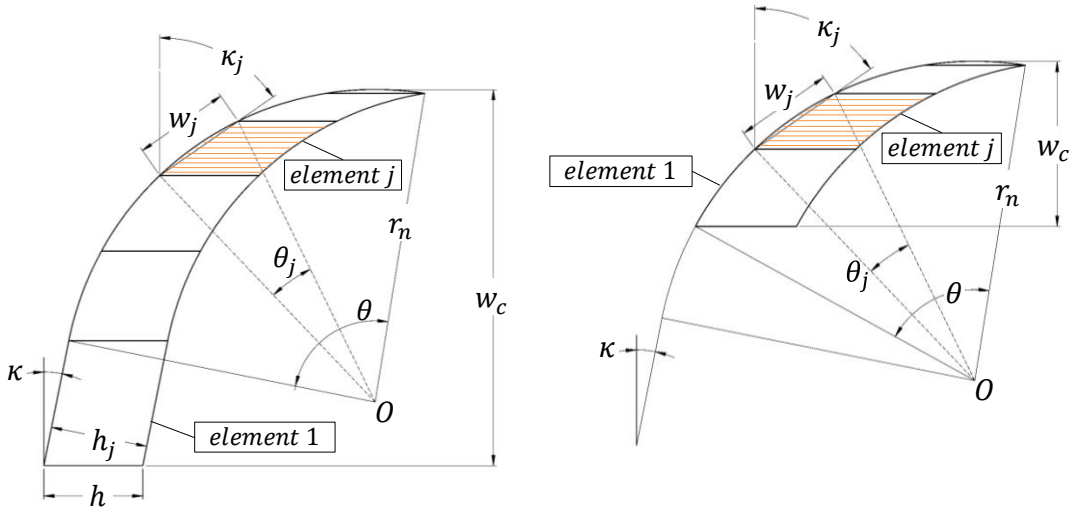

(a) (b)

Figure 11. The uncut chip area, a) $w_c > w_n$ b) $w_c < w_n$.

For calculating the local angles, below calculations are required:

$$w_n = r_n(1 - \sin(\kappa)) \tag{99}$$

If the depth of cut is higher than the nose height, below calculations are required:

$$\theta = \cos^{-1}(1 - w_n/r_n) + \sin^{-1}(f/2r_n) \tag{100}$$

$$\theta_j = \theta/(ne - 1) \tag{101}$$

$$\kappa_j = \begin{cases} \kappa & j = 1 \\ \kappa_0 + \theta_j/2 & j = 2 \\ \kappa_{j-1} + \theta_j & j > 2 \end{cases} \tag{102}$$

$$w_j = \begin{cases} (w_c - w_n)/\cos(\kappa) & j = 1 \\ 2r_n sin(\theta_j/2) & j > 1 \end{cases} \tag{103}$$

$$h_j = f.\cos(\kappa_j) \tag{104}$$

where r_n is the nose radius, κ and κ_j are side edge cutting angles for tool and j^{th} element, respectively, θ_j is the j^{th} element's angle with the origin of the insert nose, w_j is the length of each element, ne is the number of elements in uncut chip area and h_j is uncut chip thickness for each element.

For the case that depth of cut is smaller than the height of nose, only the 2nd region will

involve in the cutting and following parameters should be calculated:

$$\theta = \cos^{-1}(1 - w_c/r_n) + \sin^{-1}(f/2r_n) \tag{105}$$

$$\theta_j = \theta/(ne) \tag{106}$$

$$\kappa_j = \begin{cases} \sin^{-1}\left(1 - \frac{w_c}{r_n}\right) + \frac{\theta_j}{2} & j = 1 \\ \kappa_{j-1} + \theta_j & j > 1 \end{cases} \tag{107}$$

$$w_j = 2r_n sin(\theta_j/2) \tag{108}$$

$$h_j = f.\cos(\kappa_j) \tag{109}$$

As discussed above, in addition to global angles, the local angles should be calculated as well. The local normal rake angle, α_n^j, and local inclination angles, i^j, are to be determined with:

$$\alpha_n^j = 2\sin^{-1}\left(\cos(\kappa_j - \kappa)\sin(\alpha_n/2)\right) + 2\sin^{-1}\left(\sin(\kappa_j - \kappa)\sin(i/2)\right) \tag{110}$$

$$i^j = 2\sin^{-1}\left(\sin(\kappa_j - \kappa)\sin(\alpha_n/2)\right) + 2\sin^{-1}\left(\cos(\kappa_j - \kappa)\sin(i/2)\right) \tag{111}$$

where α_n an i are global normal rake angle and inclination angles, respectively. If $w_c > w_n$the local angles for the first element will be equal to the global values:

$$\alpha_n^1 = \alpha_n$$
$$i^1 = i \tag{112}$$

2.3.2. Heat Generation in First Deformation Zone

In order to model the turning operation, the proposed model for the orthogonal cutting has been applied to any element. The material behavior in the first deformation zone is represented by the Johnson-Cook constitutive equation as:

$$\tau^j = \frac{1}{\sqrt{3}}\left[A + B\left(\frac{\gamma}{\sqrt{3}}\right)^n\right]\left[1 + \ln\left(\frac{\dot{\gamma}}{\dot{\gamma}_0}\right)^m\right]\left[1 - \left(\frac{T_w - T_r}{T_m - T_r}\right)^v\right] \tag{113}$$

In this equation τ is shear yield stress, γ is the shear strain, $\dot{\gamma}$ is shear strain rate, $\dot{\gamma}_0$ is reference shear strain rate, T_w is absolute temperature of workpiece, T_r is the reference

temperature, T_m is the melting temperature of workpiece. $A, B, n, m,$ and υ represent the material constants.

Shear stress at the exit of shear band for each element can be obtained by:

$$\tau_1^j = \rho\left(V_c \sin\phi_n \, cosi^j\right)^2 \gamma_1^j + \tau_0^j \tag{114}$$

where τ_0^j is the shear stress at the entry of shear band, τ_1^j is the shear stress at the exit of shear band, i^j is the inclination angle and γ_1^j is the shear strain at the exit of shear band for j^{th} element. ρ is the workpiece density, V_c is the cutting speed, ϕ_n is the normal shear angle in normal plane. Due to the geometry of the oblique cutting, the vector of chip flow direction does not lie on the tool normal plane. In this case, the chip flow direction is used for defining the pressure and shear stress distribution.

In order to satisfy the continuity of the shear band, it is assumed that the normal shear angle should be equal for all the elements.

In adiabatic conditions, the temperature resulting from the conservation of energy at the end of the shear band can be determined by the following equation:

$$T_1^j = T_w + \frac{\chi}{\rho c}\left(\rho V_c^2 \sin^2\phi_n \cos^2 i^j \frac{\left(\gamma_1^j\right)^2}{2} + \tau_0^j \gamma_1^j\right) \tag{115}$$

where T_1^j is the temperature at the exit of shear band for each element, χ is the fraction of the work converted into heat and c is the heat capacity. As mentioned in the previous sections, χ is assumed to be 0.9 for metals.

2.3.3. Heat Generation in Second Deformation Zone

For modeling the second deformation zone, it is assumed that due to the high normal pressure at the tool tip and reduction of pressure along rake face, there exists sticking and sliding contact areas for each element. The total length of this friction area for each element is represented by l_{c2}^j.

As derived in detail in the model for orthogonal cutting, below parameters can be calculated for any element:

$$P_0^j = \tau_1^j \frac{h_j(\xi+1)}{l_{c2}^j} \frac{\cos\eta_s \cos\beta_n^j}{\sin\phi_n \cos\eta_c \cos(\phi_n + \beta_n^j - \alpha_n^j)} \tag{116}$$

$$l_{c2} = \frac{h_j(\xi+2)}{2} \frac{\sin(\phi_n+\beta_n^j-\alpha_n^j)}{\sin\phi_n \cos\beta_n^j \cos\eta_c^j} \tag{117}$$

$$l_{p2}^j = l_{c2}^j \left(1 - \left(\frac{\tau_1^j}{P_0^j \mu}\right)^{\frac{1}{\xi}}\right) \tag{118}$$

where P_0^j , l_{c2}^j , l_{p2}^j and η_c^j are the normal pressure at the tool tip, total contact length, sticking contact length and chip flow angle for each element. μ is the sliding friction coefficient and β_n^j is the normal friction angle:

$$\beta_n^j = \tan^{-1}\left(\tan(\beta)\cos\left(\eta_c^j\right)\right) \tag{119}$$

where β is

$$\beta = \tan^{-1}(\mu_a) \tag{120}$$

To determine the apparent friction coefficient, the ratio between the total normal force and total friction force should be obtained:

$$N = \sum_{j=1}^{n} \tau_1^j \frac{w_j h_j}{\sin\phi_n \cos i^j} \frac{\cos\eta_s \cos\beta_n^j}{\cos(\phi_n+\beta_n^j-\alpha_n^j)} \tag{121}$$

$$F = \sum_{j=1}^{n} \tau_1^j w_j \left(l_{p2}^j + \frac{l_{c2}^j - l_{p2}^j}{\xi+1}\right) \tag{122}$$

Then the apparent friction coefficient can be written as:

$$\mu_a = \frac{\sum_{j=1}^{n} \tau_1^j w_j \left(l_{p2}^j + \frac{l_{c2}^j - l_{p2}^j}{\xi+1}\right)}{\sum_{j=1}^{n} \tau_1^j \frac{w_j h_j}{\sin\phi_n \cos i^j} \frac{\cos\eta_s \cos\beta_n^j}{\cos(\phi_n+\beta_n^j-\alpha_n^j)}} \tag{123}$$

Based on previous studies, a global chip flow angle can be considered for all the elements [87]. Since each element in the chip area, has a different coordinate system, local chip flow angles should be defined for each element:

$$\eta_c^j = \begin{cases} \eta_c & j = 1 \\ \eta_c + \kappa_j - \kappa & j > 1 \end{cases} \tag{124}$$

where η_c is the global chip flow angle. To find the global chip flow angle, energy equilibrium on the chip can be considered [100]. Also the shear force can be calculated as:

$$F_s = \sum_{j=1}^{n} \frac{\tau_1^j w_j h_j}{\sin(\phi_n)\cos i^j} \tag{125}$$

To calculate the chip and shear velocity, the equilibrium of velocity should be considered and it will result in:

$$V_{ch} = \frac{V_c \sin\phi_n \cos i'}{\cos(\phi_n - \alpha_n')\cos\eta_c} \tag{126}$$

$$V_s = \frac{V_c \cos i' \cos\alpha_n'}{\cos(\phi_n - \alpha_n')\cos\eta_s} \tag{127}$$

The terms α_n' and i' are the equivalent rake and inclination angles:

$$\alpha_n' = 2\sin^{-1}(\cos(\eta_c - \kappa)\sin(\alpha_n/2)) + 2\sin^{-1}(\sin(\eta_c - \kappa)\sin(i/2)) \tag{128}$$

$$i' = 2\sin^{-1}(\sin(\eta_c - \kappa)\sin(\alpha_n/2)) + 2\sin^{-1}(\cos(\eta_c - \kappa)\sin(i/2)) \tag{129}$$

Assuming that all the removed material should flow in a unique direction, the shear flow angle is obtained with below equation:

$$\tan\eta_s = (\tan i' \cos(\phi_n - \alpha_n') - \tan\eta_c \sin\phi_n)/\cos\alpha_n' \tag{130}$$

As it was mentioned previously, the normal shear angle is assumed to be same for all the elements and it is determined considering the minimum cutting energy principle. As a result, cutting power is computed for a variety of shear angles, and the angle with the minimum power is chosen as the shear angle. For calculating the total cutting forces, below equations can be used:

$$F_t = \sum_{j=1}^{n} \frac{\tau_1^j w_j h_j \left(\cos\left(\beta_n^j - \alpha_n^j\right) + \tan i^j \tan\eta_c^j \sin\beta_n^j\right)}{\sin\phi_n \sqrt{\cos^2\left(\phi_n + \beta_n^j - \alpha_n^j\right) + \tan^2\eta_c^j \sin^2\beta_n^j}} \tag{131}$$

$$F_f = \sum_{j=1}^{n} \frac{\tau_1^j w_j h_j \sin\left(\beta_n^j - \alpha_n^j\right)}{\cos i^j \sin\phi_n \sqrt{\cos^2\left(\phi_n + \beta_n^j - \alpha_n^j\right) + \tan^2\eta_c^j \sin^2\beta_n^j}} \tag{132}$$

$$F_r = \sum_{j=1}^{n} \frac{\tau_1^j w_j h_j \left(\cos\left(\beta_n^j - \alpha_n^j\right)\tan i^j - \tan\eta_c^j \sin\beta_n^j\right)}{\sin\phi_n \sqrt{\cos^2\left(\phi_n + \beta_n^j - \alpha_n^j\right) + \tan^2\eta_c^j \sin^2\beta_n^j}} \tag{133}$$

where F_t is the tangential, F_f is the feed and F_r is the radial cutting force.

The temperature distribution in the contact area between the tool and chip will be used as a boundary condition in the calculations for tool temperature distribution. The 2-D heat

equation used in our previous report is also used for turning operation:

$$a\frac{\partial^2 T^j(x_2,y_2)}{\partial y_2^2} = \frac{V_{ch}\partial T^j(x_2,y_2)}{\partial x_2} \tag{134}$$

where $a = k/\rho c$ is the thermal diffusivity of workpiece, k is the heat conductivity, ρ is density and c is heat capacity.

The boundary conditions for solving the Equation (134) can be written as:

$$T^j(0,y_2) = T_1^j \qquad x_2 = 0\,,\ y_2 \geq 0$$

$$\lim_{y_2\to\infty} T^j(x_2,y_2) = T_1^j \qquad x_2 \geq 0 \tag{135}$$

$$-k\frac{\partial T^j(x_2,0)}{\partial y_2} = q_2^j(x_2) \qquad x_2 \geq 0$$

Equation (134) can be solved by Laplace transformation using the boundary conditions. Applying Laplace transformation to the Equation (135) will result in:

$$\alpha\frac{d^2\overline{T^j}(s,y_2)}{dy_2{}^2} = V_{ch}(s\overline{T^j}(s,y_2) - T_1^j) \tag{136}$$

$$\overline{T^j}(s,y_2) = \int_0^\infty T^j(x_2,y_2)e^{-sx_2}dx_2 \tag{137}$$

$$\overline{T^j}(s,\infty) = \frac{T_1^j}{s} \tag{138}$$

$$-k\frac{d\overline{T^j}(s,y_2)}{dy_2} = f(s) \tag{139}$$

$f(s)$ is the Laplace transform of the rake face heat flux q_2^j. Thus,

$$f(s) = \int_0^{l_{c2}^j} q_2^j(x_2)e^{(-sx_2)}dx_2 \tag{140}$$

The solution of Equation (137) will be in the form of:

$$\overline{T^j}(s,y_2) = c_1 e^{y_2\sqrt{\frac{sV_{ch}}{a}}} + c_2 e^{-y_2\sqrt{\frac{sV_{ch}}{a}}} + \frac{T_1^j}{s} \tag{141}$$

Using Equation (136), (138), (139) the Equation (141) can be solved as:

$$\overline{T^j}(s, y_2) = \frac{f(s)}{k}\sqrt{\frac{a}{sV_{ch}}}\,e^{-y_2\sqrt{\frac{sV_{ch}}{a}}} + \frac{T_1^j}{s} \tag{142}$$

Applying Reverse Laplace Transform to Equation (142) the temperature distribution equation can be determined as:

$$T^j(x_2, y_2) = \frac{1}{k}\sqrt{\frac{a}{\pi V_{ch}}}\int_0^{x_2} q_2^j(x_2 - u)\frac{1}{\sqrt{u}}e^{(-\frac{V_{ch}y_T^2}{4au})}du + T_1^j \tag{143}$$

Using the convolution property of the Laplace and inverse Laplace transforms, the temperature distribution on the rake face can be found:

$$T_2^j(x_2, 0) = \frac{1}{k}\sqrt{\frac{a}{\pi V_{ch}}}\int_0^{x_2} q_2^j(x_2 - u)\frac{1}{\sqrt{u}}du + T_1^j \tag{144}$$

where q_2^j is the heat flux on rake face contact for any element. Sticking and sliding friction areas in the second deformation zone must be taken into account for the calculation of the heat flux. In this case, the heat flux can be defined as follows:

$$q_2^j(x_2) = \begin{cases} \tau_1^j V_{ch} & x_2 \le l_{p2}^j \\ \mu_{sl} V_{ch} P_0^j \left(1 - \frac{x_2}{l_{c2}^j}\right)^{\xi} & l_{p2}^j \le x_2 \le l_{c2}^j \\ 0 & x_2 \ge l_{c2}^j \end{cases} \tag{145}$$

Replacing the q_2^j in Equation (144) with Equation (145) the temperature distribution along the tool-chip interface for each element can be obtained as:

$$T_2^j(x_2) = \frac{1}{k}\sqrt{\frac{\alpha}{V_{ch}}}\left(\int_0^{l_{p2}^j} \tau_1^j V_{ch}\frac{1}{\sqrt{\pi u}}du + \int_{l_{p2}^j}^{l_{c2}^j} \mu_{sl} V_{ch} P_0^j \left(1 - \frac{x_2 - u}{l_{c2}^j}\right)^{\xi}\frac{1}{\sqrt{\pi u}}du\right) + T_1^j \tag{146}$$

2.3.4. Heat Generation in Third Deformation Zone

In turning process, due to the contribution of nose radius in the cutting, parameters like contact length, normal pressure distribution, and shear stress in third deformation zones may vary at different points along depth of cut direction. Consequently, the tool is divided into smaller elements, j, and the calculation for oblique cutting are performed for any element, separately. However, the chip flow angle is considered to have a unique value for all elements, as it is observed in the experimental studies [100].

Cutting edge radius of the tool results in the formation of third deformation zone. The reason is the recovery of ploughed material, which are placed under the stagnation point. This point separates the second deformation zone from the third deformation zone. The total contact length on the flank face is identified by using the fully elastic recovery assumption [86]. Considering the inclination angle, there are three regions on the flank contact:

$$l_1^j = r\theta_s / \cos i^j \tag{147}$$

$$l_2^j = r\lambda / \cos i^j \tag{148}$$

$$l_3^j = r\frac{\cos\lambda - \cos\theta_s}{\sin\lambda \cos i^j} \tag{149}$$

$$l_{c3}^j = l_1^j + l_2^j + l_3^j = \frac{r_h}{\cos i^j}\left(\theta_s + \lambda + \frac{\cos\lambda - \cos\theta_s}{\sin\lambda}\right) \tag{150}$$

where r is the cutting edge radius, θ_s is the stagnation angle, λ is the clearance angle and l_{c3}^j is the total flank contact length for each element.

Similar to the normal pressure distribution used in the orthogonal cutting model, the normal pressure distribution for turning is defined by the following equation [86]:

$$P_3^j(x_3) = P_0^j(a_j x_3^2 + b_j x_3 + c_j) \tag{151}$$

where,

$$\begin{aligned} a_j &= \frac{1}{2lc_3^j l_3^j - lc_3^j} \\ b_j &= -2a_j l_1^j \\ c_j &= 1 \end{aligned} \tag{152}$$

where P_0^j is the normal pressure at the stagnation point for each element and x_f is the distance from tool tip on the flank face.

Due to the existence of sticking and sliding friction regions on the flank contact, third deformation zone is represented by a dual-zone contact model. The tool-workpiece contact might be sticking as the result of high normal pressure or sliding which appears due to the decrease of normal pressure. Using the coulomb friction law along the sliding zone below equation can be written:

$$\tau_{(x_3)}^{j} = \mu_{sl} P_0^j (a_j x_3^2 + b_j x_3 + c_j) \tag{153}$$

At the end of sticking zone, the tangential stress is equal to the shear yield stress:

$$\tau_1^j = \mu_{sl} P_0^j (a_j . {l_{p3}^j}^2 + b_j . l_{p3}^j + c_j) \tag{154}$$

From Equation (154) the length of sticking contact zone can be determined as:

$$l_{p3}^j = \frac{-b_j + \sqrt{b_j^2 - 4a_j(c_j - \frac{\tau_1^j}{\mu P_0^j})}}{2a_j} \tag{155}$$

In the calculation of the heat generated in the third deformation zone, the 2D heat equation was used similar to the calculation of the second deformation zone:

$$a \frac{\partial^2 T^j(x_3, y_3)}{\partial y_3^2} = \frac{V_c \partial T^j(x_3, y_3)}{\partial x_3} \tag{156}$$

The boundary conditions for solving the Equation (156) can be written as:

$$\begin{aligned} &T^j(0, y_3) = T_1^j && \text{for} \quad x_3 = 0, y_3 \geq 0 \\ &\lim_{y \to d} T^j(x_3, y_3) = T_\infty && \text{for } x_3 \geq 0 \\ &-k \frac{\partial T^j(x_3, 0)}{\partial y_3} = q_3^j(x_3) && \text{for } x_3 \geq 0 \end{aligned} \tag{157}$$

where T_∞ is the room temperature and d is the workpiece diameter. Laplace transformation is used to solve the Equation (156) considering the boundary conditions in Equation (157). After applying Laplace transformation, the Equation (156) and (157) can be written as:

$$\alpha \frac{d^2 \overline{T^j}(s, y_3)}{dy_3^2} = V_c (s \overline{T^j}(s, y_3) - T_1^j) \tag{158}$$

$$\begin{aligned} &\bar{T}^j(s, y_3) = \int_0^\infty T^j(x_3, y_3) e^{-s x_3} dx \\ &\bar{T}^j(s, \infty) = \frac{T_1^j}{s} \\ &-k \frac{d\bar{T}^j(s, y_3)}{dy_3} = g(s) \end{aligned} \tag{159}$$

$g(s)$ is the Laplace transform of the heat flux q_3^j. Thus, it can be written as:

$$g(s) = \int_0^{l_{c3}^j} q_3^j(x_3) e^{(-sx_3)} dx \tag{160}$$

The solution of Equation (159) will be in the form of:

$$\bar{T}^j(s, y_3) = c_1 e^{y_3\sqrt{\frac{sV_c}{a}}} + c_2 e^{-y_3\sqrt{\frac{sV_c}{a}}} + \frac{T_1^j}{s} \tag{161}$$

Using Equation (159) the Equation (161) can be solved as:

$$\overline{T^j}(s, y) = \frac{g(s)}{k}\sqrt{\frac{a}{sV_c}} e^{-y_f\sqrt{\frac{sV_c}{a}}} + \frac{T_1^j}{s} \tag{162}$$

In order to find the relation for expressing the temperature distribution on flank face, Reverse Laplace Transform should be applied to Equation (162):

$$T^j(x_3, y_3) = \frac{1}{k}\sqrt{\frac{a}{\pi V_c}} \int_0^{x_f} q_3^j(x_f - u) \frac{1}{\sqrt{u}} e^{(-\frac{V_c y_f^2}{4au})} du + \left(\frac{T_\infty - T_1^j}{d}\right)(y_3) + T_1^j \tag{163}$$

The temperature distribution on the flank face is calculated using the convolution property of the Laplace and inverse Laplace transforms:

$$T_3^j(x_3, 0) = \frac{1}{k}\sqrt{\frac{a}{\pi V_c}} \int_0^{x_3} q_3^j(x_3 - u) \frac{1}{\sqrt{u}} du + T_1^j \tag{164}$$

Shear stress due to friction conditions in the third region can be expressed as follows:

$$\tau^j(x_3) = \begin{cases} \tau_1^j & x_3 \le l_{p3}^j \\ \mu_{sl} P_3^j & l_{p3}^j \le x_3 \le l_{c3}^j \\ 0 & x_3 \ge l_{c3}^j \end{cases} \tag{165}$$

Then the heat flux can be described as:

$$q_3^j(x_3) = \begin{cases} \tau_1^j V_i & x_3 \le l_{p3}^j \\ \mu_{sl} P_0^j (a_j x_3^2 + b_j x_3 + c_j) V_i & l_{p3}^j \le x_3 \le l_{c3}^j \\ 0 & x_3 \ge l_{c3}^j \end{cases} \tag{166}$$

Be applying the Equation (166) to Equation (164) the temperature distribution in the tool-workpiece contact area can be determined as:

$$T_3^j(x_3) = \frac{1}{k}\sqrt{\frac{\alpha}{V_c}}\left(\int_0^{l_{p3}^j} \tau_1^j V_i \frac{1}{\sqrt{\pi u}} du + \int_{l_{p3}^j}^{l_{c3}^j} \mu_{sl} P_0^j (a_j x_3^2 + b_j x_3 + c_j) V_i \frac{1}{\sqrt{\pi u}} du\right) + T_1^j \tag{167}$$

2.3.5. Temperature Distribution in Cutting Tool for Turning

Due to the existence of nose radius in the turning process, the calculations are different from the oblique cutting. As it was discussed in the previous sections, the cutting tool is divided into different segment in the depth of cut direction. The force and heat flux calculations are performed for any of these elements separately. The calculated temperature at the tool-chip and tool-workpiece contact areas for each element, are considered as a boundary condition for the grid points on the tool rake and flank faces. A convection boundary condition for the grids, which are not in contact with chip or workpiece, were considered. The surfaces that are far from cutting area supposed to have room temperature. Figure 12 shows the boundary conditions applied to each element in turning model.

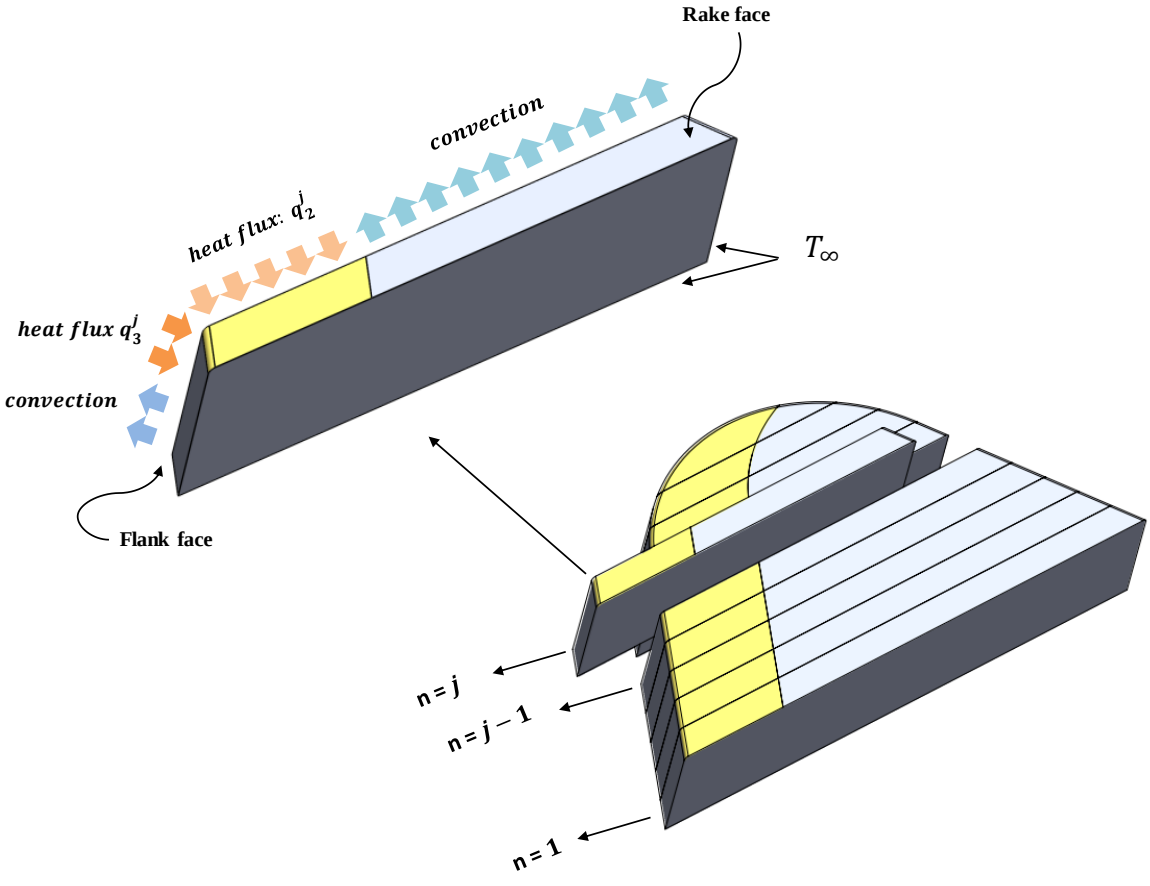

Figure 12. Heat flux and convection for each element in turning model

When the temperature at the rake and flank faces are determined, the temperature distribution inside the tool is calculated by using Finite Difference Method. The temperature distribution in the tool is obtained by solving the 3D steady-state heat equation below:

$$\frac{\partial^2 T(x,y,z)}{\partial x^2}+\frac{\partial^2 T(x,y,z)}{\partial y^2}+\frac{\partial^2 T(x,y,z)}{\partial z^2}=0 \tag{168}$$

As mentioned above, Finite Difference Method is used in the solution of this equation. Similar to oblique and orthogonal cutting, structured grid generation method was used [98]. The first step is determining the location of grid points inside tool, chip and workpiece. In this study, a 2D grid is constructed in $x-y$ plane with the use of elliptic grid generation method and these grids are distributed in z direction with equal intervals. The solution of a partial differential equation is used to relate the physical and computational domain. The transformation from the physical x, y coordinates to the computational ξ, η coordinates can be expressed as

$$\begin{aligned} \xi &\equiv \xi(x,y) \\ \eta &\equiv \eta(x,y) \end{aligned} \tag{169}$$

Transformation relations for mapping from x, y plane to the ξ, η (or vice versa) are determined from the numerical solution of elliptic partial differential equations below:

$$\begin{aligned} \nabla^2\xi &= \frac{\partial^2\xi}{\partial x^2}+\frac{\partial^2\xi}{\partial y^2}=0\,, \\ \nabla^2\eta &= \frac{\partial^2\eta}{\partial x^2}+\frac{\partial^2\eta}{\partial y^2}=0 \end{aligned} \tag{170}$$

The transformation relations can be developed by application of the chain rule of differentiation:

$$\begin{aligned} \frac{\partial}{\partial x} &= \frac{\partial\xi}{\partial x}\cdot\frac{\partial}{\partial\xi}+\frac{\partial\eta}{\partial x}\cdot\frac{\partial}{\partial\eta}=\xi_x\frac{\partial}{\partial\xi}+\eta_x\frac{\partial}{\partial\eta} \\ \frac{\partial}{\partial y} &= \frac{\partial\xi}{\partial y}\cdot\frac{\partial}{\partial\xi}+\frac{\partial\eta}{\partial y}\cdot\frac{\partial}{\partial\eta}=\xi_y\frac{\partial}{\partial\xi}+\eta_y\frac{\partial}{\partial\eta} \\ \frac{\partial^2}{\partial x^2} &= \frac{\partial^2}{\partial\xi^2}\cdot\left(\frac{\partial\xi}{\partial x}\right)^2+2\frac{\partial^2}{\partial\xi\partial\eta}\left(\frac{\partial\xi}{\partial x}\cdot\frac{\partial\eta}{\partial x}\right)+\frac{\partial^2}{\partial\eta^2}\cdot\left(\frac{\partial\eta}{\partial x}\right)^2 \\ \frac{\partial^2}{\partial y^2} &= \frac{\partial^2}{\partial\xi^2}\cdot\left(\frac{\partial\xi}{\partial y}\right)^2+2\frac{\partial^2}{\partial\xi\partial\eta}\left(\frac{\partial\xi}{\partial y}\cdot\frac{\partial\eta}{\partial y}\right)+\frac{\partial^2}{\partial\eta^2}\cdot\left(\frac{\partial\eta}{\partial y}\right)^2 \end{aligned} \tag{171}$$

where the subscripts denote differentiation with respect to the variable considered. Then the Laplace operator can be written as:

$$\nabla^2 = \frac{\partial^2}{\partial \xi^2}\left(\left(\frac{\partial \xi}{\partial x}\right)^2 + \left(\frac{\partial \xi}{\partial y}\right)^2\right) + \frac{\partial^2}{\partial \eta^2}\left(\left(\frac{\partial \eta}{\partial x}\right)^2 + \left(\frac{\partial \eta}{\partial y}\right)^2\right) + 2\,\frac{\partial^2}{\partial \xi\,\partial \eta}\left(\frac{\partial \xi}{\partial x}\cdot\frac{\partial \eta}{\partial x} + \frac{\partial \xi}{\partial y}\cdot\frac{\partial \eta}{\partial y}\right) \tag{172}$$

By the interchange of x and y with ξ and η respectively, we will get:

$$\frac{\partial}{\partial \xi} = x_\xi \frac{\partial}{\partial x} + y_\xi \frac{\partial}{\partial y}$$
$$\frac{\partial}{\partial \eta} = x_\eta \frac{\partial}{\partial x} + y_\eta \frac{\partial}{\partial y} \tag{173}$$

Using Cramer's rule for solving the system of equations, transformation relations for the first derivatives can be determined as:

$$\frac{\partial}{\partial x} = \frac{1}{J}\left(y_\eta \frac{\partial}{\partial \xi} - y_\xi \frac{\partial}{\partial \eta}\right)$$
$$\frac{\partial}{\partial y} = \frac{1}{J}\left(-x_\eta \frac{\partial}{\partial \xi} + x_\xi \frac{\partial}{\partial \eta}\right) \tag{174}$$

where the Jacobian of the transformation is defined as:

$$J = \begin{vmatrix} x_\xi & y_\xi \\ x_\eta & y_\eta \end{vmatrix} = x_\xi y_\eta - y_\xi x_\eta \neq 0 \tag{175}$$

It can be concluded that:

$$\xi_x = \frac{1}{J} y_\eta, \qquad \xi_y = -\frac{1}{J} x_\eta$$
$$\eta_x = -\frac{1}{J} y_\xi, \quad \eta_y = \frac{1}{J} x_\xi \tag{176}$$

Laplace operator can be written as:

$$\nabla^2 = \frac{\partial^2}{\partial \xi^2}\left(\left(\frac{\partial \xi}{\partial x}\right)^2 + \left(\frac{\partial \xi}{\partial y}\right)^2\right) + 2\,\frac{\partial^2}{\partial \xi\,\partial \eta}\left(\frac{\partial \xi}{\partial x}\cdot\frac{\partial \eta}{\partial x} + \frac{\partial \xi}{\partial y}\cdot\frac{\partial \eta}{\partial y}\right) + \frac{\partial^2}{\partial \eta^2}\left(\left(\frac{\partial \eta}{\partial x}\right)^2 + \left(\frac{\partial \eta}{\partial y}\right)^2\right) = J^2\left(\alpha \frac{\partial^2}{\partial \xi^2} - 2\beta \frac{\partial^2}{\partial \xi \partial \eta} + \gamma \frac{\partial^2}{\partial \eta^2}\right) \tag{177}$$

Then the equation (170) becomes:

$$\alpha \frac{\partial^2 x}{\partial \xi^2} - 2\beta \frac{\partial^2 x}{\partial \xi \partial \eta} + \gamma \frac{\partial^2 x}{\partial \eta^2} = 0$$
$$\alpha \frac{\partial^2 y}{\partial \xi^2} - 2\beta \frac{\partial^2 y}{\partial \xi \partial \eta} + \gamma \frac{\partial^2 x}{\partial \eta^2} = 0 \tag{178}$$

where the geometric coefficients α, β, γ are given by:

$$\alpha = \left(\frac{\partial x}{\partial \eta}\right)^2 + \left(\frac{\partial y}{\partial \eta}\right)^2$$
$$\beta = \frac{\partial x}{\partial \xi}\frac{\partial x}{\partial \eta} + \frac{\partial y}{\partial \xi}\frac{\partial y}{\partial \eta} \tag{179}$$
$$\gamma = \left(\frac{\partial x}{\partial \xi}\right)^2 + \left(\frac{\partial y}{\partial \xi}\right)^2$$

The location of the boundary points on tool, chip and workpiece are used as a boundary condition for solving Equations (178). An iterative procedure is used in the solution of these equations. The iteration continues until the maximum difference between two successive iteration reaches a predefined tolerance value. The solution of this problem determines the values of the x, y coordinates at each ξ, η grid point in the computational domain. Once the correspondence between x, y and ξ, η coordinate values are known at each grid point in the computational domain, the results can be transformed to the physical domain.

After determining the location of all grid points for tool, chip and workpiece, the heat conduction equation should be transformed from x, y, z to ξ, η, ϑ coordinates of the computational domain as:

$$\frac{\partial^2 T}{\partial \xi^2}\left({\xi_x}^2 + {\xi_y}^2 + {\xi_z}^2\right) + \frac{\partial^2 T}{\partial \eta^2}\left({\eta_x}^2 + {\eta_y}^2 + {\eta_z}^2\right) + \frac{\partial^2 T}{\partial \vartheta^2}\left({\vartheta_x}^2 + {\vartheta_y}^2 + {\vartheta_z}^2\right) + 2\,\frac{\partial^2 T}{\partial \xi\,\partial \eta}\left(\xi_x \,.\, \eta_x + \xi_y \,.\, \eta_y + \xi_z \,.\, \eta_z\right) + 2\,\frac{\partial^2 T}{\partial \xi\,\partial \vartheta}\left(\xi_x \,.\, \vartheta_x + \xi_y \,.\, \vartheta_y + \xi_z \,.\, \vartheta_z\right) + 2\,\frac{\partial^2 T}{\partial \eta\,\partial \vartheta}\left(\eta_x \,.\, \vartheta_x + \eta_y \,.\, \vartheta_y + \eta_z \,.\, \vartheta_z\right) = 0 \tag{180}$$

The finite difference form of second order derivatives for interior points can be written as:

$$\frac{\partial^2 T}{\partial \xi^2} = T_{i+1,j,k} - 2T_{i,j,k} + T_{i-1,j,k}$$
$$\frac{\partial^2 T}{\partial \eta^2} = T_{i,j+1,k} - 2T_{i,j,k} + T_{i,j-1,k}$$
$$\frac{\partial^2 T}{\partial \vartheta^2} = T_{i,j,k+1} - 2T_{i,j,k} + T_{i,j,k-1}$$
$$\frac{\partial^2 T}{\partial \xi \partial \eta} = \frac{1}{4}\left(T_{i+1,j+1,k} - T_{i-1,j+1,k} - T_{i+1,j-1,k} + T_{i-1,j-1,k}\right) \tag{181}$$
$$\frac{\partial^2 T}{\partial \xi \partial \vartheta} = \frac{1}{4}\left(T_{i+1,j,k+1} - T_{i-1,j,k+1} - T_{i+1,j,k-1} + T_{i-1,j,k-1}\right)$$
$$\frac{\partial^2 T}{\partial \eta \partial \vartheta} = \frac{1}{4}\left(T_{i,j+1,k+1} - T_{i,j-1,k+1} - T_{i,j+1,k-1} + T_{i,j-1,k-1}\right)$$

Using equation (146) the temperature of chip, at tool-chip interface can be calculated analytically for each element. Equation (167) can be used for determining the temperature of workpiece at the tool-workpiece interface, as well. These temperatures can be used as a boundary condition in solving equation (168) for tool. Due to the existence of nose radius, inclination angle and chip flow angle in turning operation, the grid points on tool-chip interface on the tool and chip sides are not coincident. It also happens for the grids of tool and workpiece at flank contact area. Therefore, the temperature of any point on rake and flank contact area is considered equal to the temperature of closest point on chip and workpiece, respectively.

For the segments of rake and flank surfaces, which are not in contact with the chip or workpiece, convection boundary condition was considered:

$$-k\frac{\partial T}{\partial n} = h(T - T_{\infty}) \tag{182}$$

where h and T_{∞} are the heat transfer coefficient and temperature of environment, respectively. The faces, which are located far from the cutting area, are considered to have room temperature.

2.3.6. Solution Procedure

This section presents the solution procedure for the calculation of cutting temperature in the turning process, using proposed model. The first step is creation of elements by using Equations (100)-(109). Calculations start with an initial value for the normal shear angle, ϕ_n and chip flow angle, η_c. The equivalent rake and inclination angles can be calculated by Equations (128) and (129). The next steps is the calculation of chip velocity, V_{ch}, shear velocity V_s, and shear flow angle η_s by the Equations (126), (127) and (128), respectively. In this step the sliding friction coefficient, μ_{sl} can be calculated using the calibrated equations provided by Ozlu et al. [99]. The calculation continues with an iterative procedure for determining the apparent friction coefficient. For an initial value of μ_a, friction angle β can be calculated. Then the calculations related to each element starts. For each element η_c^j ,β_n^j , l_{c2}^j, l_{p2}^j, and τ_1^j can be obtained from the Equations (124), (119), (117), (118) and (115), respectively. Now cutting forces can be determined by the Equation (131). To calculate the apparent friction coefficient the Equation (123) is used. If the difference between selected and newly calculated μ_a meets the requirements of desired tolerance, the iteration for apparent fraction coefficient ends. To select the global

chip flow angle, the equilibrium of energy should be satisfied. To use the minimum cutting energy principle in selecting the normal shear angle, the whole procedure should be repeated for different values of shear angles.

The next step is the simulations related to third deformation zone. The total contact length, l_{c3}^{j}, sticking contact length, l_{p3}^{j}, normal pressure distribution on flank face, P_3^j, and local velocity at any point, V_i should be determined.

After determining the contact lengths and pressure distribution on rake and flank faces of each element, the heat fluxes for second and third deformation zones can be calculated using Equations (145) and (166). Finally, the temperature on tool-chip and tool-workpiece contact areas can be determined using equations (146) and (167), respectively. All these calculations should be done for any element. Due to the existence of inclination angle and chip flow angle in turning operation, the grid points on tool-chip interface on the tool and chip sides are not coincident. It also happens for the grids of tool and workpiece at flank contact area. Therefore, the temperature of any point on rake and flank contact area is considered equal to the temperature of closest point on chip and workpiece, respectively. Convection boundary condition should be applied to the areas on rake and flank faces, which are not in contact with chip or workpiece. Room temperature is applied to the regions which are far away from cutting edge. After calculating the temperature on contact areas for each element and applying the other boundary conditions, the temperaure distribution inside the cutting tool is calculted using FDM method.

2.4. Temperature Distribution of Worn Tool

2.4.1. Model in Orthogonal Cutting Condition

Cutting temperature in the presence of flank wear can significantly affect the tool life, part surface quality and dimensional tolerance of produced part. Thus, understanding the cutting temperature distribution is of high importance in cutting process modeling. In this study, Finite Difference Method is used to determine the temperature distribution in the worn cutting tool when the temperature distribution along the rake and flank contact length can be calculated analytically. The flank wear is shown in Figure 13. VN is called depth of cut line and VB is considered to be the flank wear.

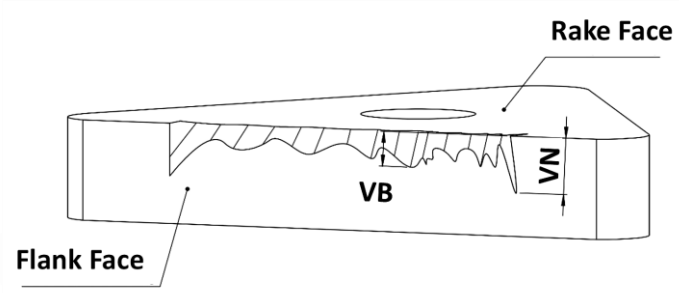

Figure 13. Flank wear (V_B) of cutting tool.

The force model for a worn tool is adapted from orthogonal cutting model. Considering the flank wear, the total contact length on the flank face and pressure distribution of third deformation zone will change. These modifications are explained in this section.
The geometry of a worn tool is shown in Figure 14. Based on this figure, the total contact length on the flank face of a worn tool can be divided to 3 regions:

$$AB: l_1 = r(\theta_s - \theta_{w1}) \tag{183}$$

$$BC: l_2 = VB \tag{184}$$

$$CD: l_3 = r\left(\frac{\cos\lambda - \cos\theta_s}{sin\,\lambda} - \tan(\theta_{w2} - \lambda)\right) \tag{185}$$

$$l_{c3} = l_1 + l_2 + l_3 \tag{186}$$

where,

$$\theta_{w2} = \sin^{-1}\left(\frac{VB}{r} - \sin\theta_{w1}\right) \tag{187}$$

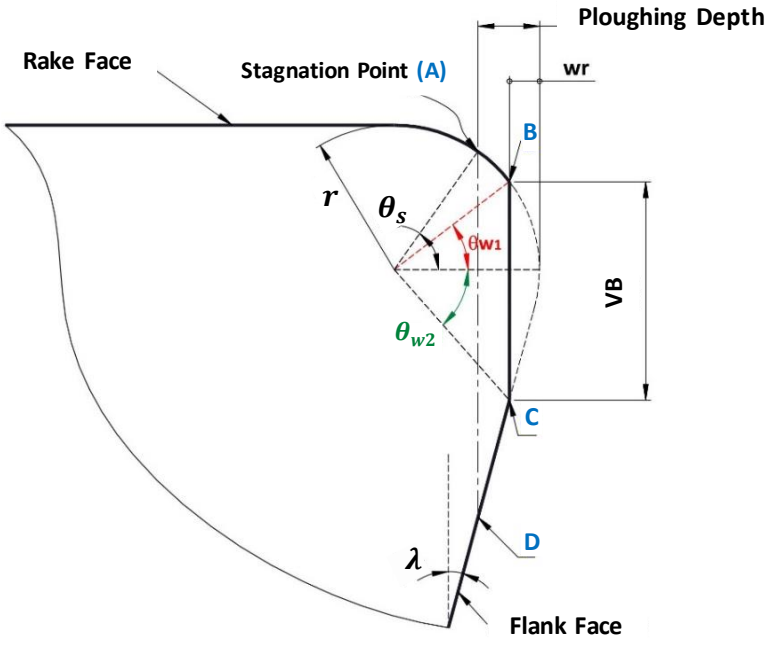

Figure 14. Geometry of flank wear.

Based on the proposed model for the orthogonal cutting, a modified increasing decreasing pressure distribution is used for wear model. This distribution is shown in Figure 15. Normal pressure on the flank face, first increases along AB. On the wear area (BC) a constant pressure (P_{avg}) is considered and starting from point C pressure will decrease until it reaches zero value at the end of total contact length on flank face, D. P_{avg} can be explained as:

$$P_{avg} = \frac{1}{2}(P_3(l_1) + P_3(l_1 + l_2)) \tag{188}$$

where P_3 is the normal pressure distribution on flank face without wear. A new equation is fitted to the points A, B, C and D. Therefore, the coefficients of this relation can be

calculated using points:

$$\begin{aligned} &A: \ @x_3 = 0 && P_{3w} = P_0 \\ &B: \ @x_3 = l_1 && P_{3w} = P_{avg} \\ &C: \ @x_3 = l_1 + l_2 && P_{3w} = P_{avg} \\ &D: \ @x_3 = l_{cw} && P_{3w} = 0 \end{aligned} \tag{189}$$

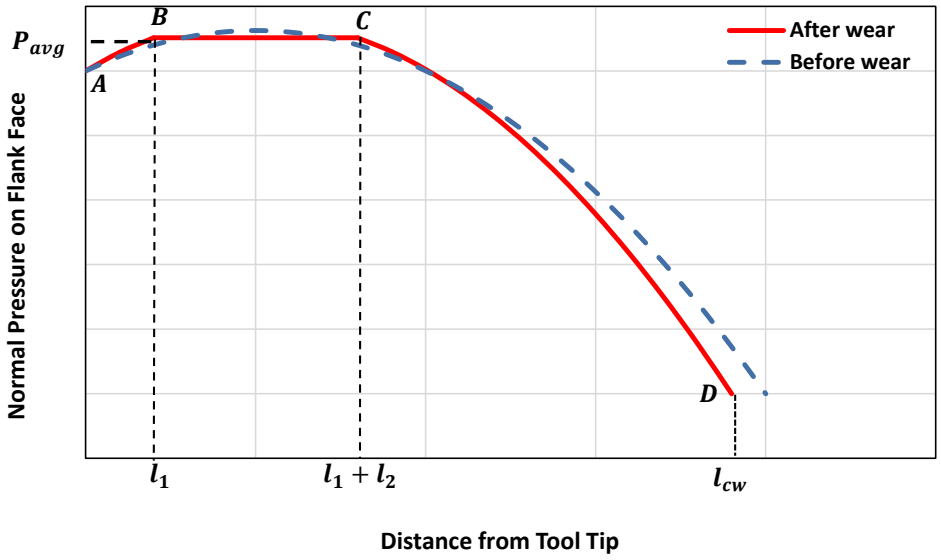

Figure 15. Modified normal pressure distribution on worn flank face.

In the third deformation zone, the contact between tool flank face and machined surface of workpiece results in the friction and temperature rise in this region. Using the dual-zone model, the heat flux for a worn tool can be written as:

$$q_{3w}(x_3) = \begin{cases} \tau_1 V_i & 0 \le x \le l_{p3} \\ \mu_{sl} V_i P_{3w} & l_{p3} \le x \le l_{cw} \\ 0 & x \ge l_{cw} \end{cases} \tag{190}$$

where V_i is the local speed for any point along the flank contact.

Applying the Equation (190) to the Equation (32) the temperature distribution equation of a worn tool can be determined as:

$$T(x_3, 0) = \frac{1}{k}\sqrt{\frac{a}{V_c}}\left(\int_0^{l_{p3}} \tau_1 V_i \frac{1}{\sqrt{\pi u}} du + \int_{l_{p3}}^{l_{c3}} \mu_{sl} V_i P_{3w}(x) \frac{1}{\sqrt{\pi u}} du\right) + T_1 \tag{191}$$

2.4.2. Model in Oblique Cutting Condition

Modeling the wear in oblique cutting is adopted from the orthogonal cutting model. Due to the use of inclination angle, some modification should be applied to the orthogonal model.

The total contact length on the flank face of a worn tool in oblique cutting can be divided to three regions:

$$l_{cw} = l_1 + l_2 + l_3$$

$$l_1 = r(\theta - \theta_{w1})/\cos i$$

$$l_2 = VB/\cos i \tag{192}$$

$$l_3 = \frac{r}{\cos i}\left(\frac{cos\,\lambda - cos\,\theta}{sin\,\lambda} - \tan(\theta_{w2} - \lambda)\right)$$

where,

$$\theta_{w2} = \sin^{-1}\left(\frac{VB}{r} - \sin\theta_{w1}\right) \tag{193}$$

A pressure distribution similar to the orthogonal condition is used in oblique cutting which can be described with Equation (189).

Finally placing the equation (189) in the equation (29), the temperature distribution equation on the tool-workpiece contact for a worn tool can be calculated as:

$$T(x_3, 0) = \frac{1}{k}\sqrt{\frac{a}{\pi V_c}}\left(\int_0^{l_{p3}} \tau_1 V_i \frac{1}{\sqrt{u}}du + \int_{l_{p3}}^{l_{cw}} \mu_{sl} V_i P_{3w}(x_3)\frac{1}{\sqrt{u}}du\right) \tag{194}$$

2.4.3. Model in Turning Operations

In the previous sections, the implementation of flank wear into the orthogonal and oblique cutting models was described. In this step, the wear is included in the temperature model for the turning process.

The force model for a worn tool is adapted from oblique cutting model. Considering the flank wear, the total contact length on the flank face and pressure distribution of third deformation zone will change. These modifications are explained in this section. On the other hand, existence of nose radius in the turning process results in some modifications

to the calculations that are used in oblique cutting. As it was discussed in the previous sections, the cutting tool is divided into different segment in the depth of cut direction and the calculations for the oblique cutting is applied to any of these elements, separately. The total contact length on the flank face of a worn tool is assumed to include three regions:

$$AB: l_1^j = r(\theta_s - \theta_{w1})/\cos i^j \tag{195}$$

$$BC: l_2^j = VB/\cos i^j \tag{196}$$

$$CD:\ l_3^j = r\frac{\cos\lambda - \cos\theta_s}{\sin\lambda \cos i^j} - \frac{-\tan(\theta_{w2} - \lambda)}{\cos i^j} \tag{197}$$

$$l_{cw}^j = l_1^j + l_2^j + l_3^j \tag{198}$$

where,

$$\theta_{w2} = \sin^{-1}\left(\frac{VB}{r} - \sin\theta_{w1}\right) \tag{199}$$

Based on the proposed model for the orthogonal cutting, a modified increasing decreasing pressure distribution is used for wear model in turning. Normal pressure on the flank face, first increases along AB (Figure 15). On the wear area (BC) a constant pressure (P_{avg}) is considered and starting from point C pressure will decrease until it reaches zero value at the end of total contact length on flank face, D. P_{avg} can be explained as:

$$P_{avg}^j = \frac{1}{2}\left(P_3^j\left(l_1^j\right) + P_3^j(l_1^j + l_2^j)\right) \tag{200}$$

where P_3^j is the normal pressure distribution for any element j on the flank face without wear. A new equation is fitted to the points $A, B, C\ and\ D$. Therefore, the coefficients of this relation can be calculated using points:

$$\begin{aligned}
&A:\ @x = 0 && P_{3w}^j = P_0^j \\
&B:\ @x = l_1^j && P_{3w}^j = P_{avg}^j \\
&C:\ @x = l_1^j + l_2^j && P_{3w}^j = P_{avg}^j \\
&D:\ @x = l_{cw}^j && P_{3w}^j = 0
\end{aligned} \tag{201}$$

In order to consider the effect of nose radius, similar to the force calculations, the heat flux calculations should also performed for any element. In the third deformation zone, the contact between tool flank face and machined surface of workpiece results in the friction and temperature rise in this region. In this study, flank contact is modeled by dual zone model. In this model, the flank contact starts with sticking region and it is followed by sliding area. The reason is high normal pressure at the stagnation point. Then, the reduced normal pressure converts the friction state to Coulomb friction. Mathematically, this friction situation can be expressed as follows:

$$\tau_{(x_3)}^{j} = \begin{cases} \tau_1^j & 0 \le x_3 \le l_{p3}^j \\ \mu_{sl} P_{3w}^j & l_{p3}^j \le x_3 \le l_{cw}^j \\ 0 & x_3 \ge l_{cw}^j \end{cases} \tag{202}$$

where τ^j is the shear stress, τ_1^j is the shear stress at the exit of shear band for jth element and μ_{sl} is the sliding friction coefficient. Consequently, the heat flux can be written as:

$$q_{3w}^{j}(x_3) = \begin{cases} \tau_1^j V_i^j & 0 \le x_3 \le l_{p3}^j \\ \mu_{sl} V_i^j P_{3w}^j & l_{p3}^j \le x_3 \le l_{cw}^j \\ 0 & x_3 \ge l_{cw}^j \end{cases} \tag{203}$$

where V_i^j is the local speed for any point along the flank contact on element j.

Importing the Equation (203) to Equation (164) the temperature distribution in the tool-workpiece contact area while cutting with a worn tool can be determined as:

$$T_3^j(x_3) = \frac{1}{k}\sqrt{\frac{\alpha}{V_c}}\left(\int_0^{l_{p3}^j} \tau_1^j V_i^j \frac{1}{\sqrt{\pi u}} du + \int_{l_{p3}^j}^{l_{cw}^j} \mu_{sl} P_{3w}^j V_i^j \frac{1}{\sqrt{\pi u}} du\right) + T_1^j \tag{204}$$

Therefore, the temperature at the tool-workpiece contact area of a worn tool, can be calculated for any element j in the depth of cut direction. Then, similar to the calculations for a new tool, these temperatures are used as a boundary condition for the grids points on the tool.

3. EXPERIMENTAL VERIFICATION

3.1. Orthogonal Cutting Experiments

Experimental studies were conducted on Mori Seiki NL1500 CNC lathe. Uncoated WC grooving KennaMetal inserts (Figure 16) without chip breaker was used. Al 7075 and AISI 1050 were used as the workpiece materials. Three methods were used for temperature measurement which are thermocouples attached to the tool, thermocouples attached to the workpiece, and thermal camera. Face turning operation is applied in dry cutting conditions in order to capture the temperature distribution with the thermal camera. The cutting-edge radius of inserts were measured using NanoFocus, µsurf confocal microscope. All the tests are conducted under orthogonal cutting conditions i.e. there is no oblique angle on the tool. The first set of tests are conducted with Al7075 workpiece material. The tool has cutting-edge radius of 50 µm, rake angle of 5° and clearance angle of 7°. The thermal properties of the tool and workpiece can be seen in Table 1. The coefficients of Johnson-Cook equation for aluminum are $A = 286, B = 575, n = 0.71, m = 0.024, \upsilon = 1.6$ which were calibrated from orthogonal cutting tests [101]. The sliding friction coefficient for Al7075-WC pair can be obtained from the experiments as [99]:

$$\mu_{sl} = 5 \times 10^{-7} V_{ch} - 7 \times 10^{-4} V_{ch} + 0.4258 \quad (205)$$

where V_{ch} is the chip velocity in m/min.

Figure 16. Grooving insert used in the experiments

Table 1. Thermal properties of cutting tool and workpiece.

	Density (kg/m^3)	Thermal conductivity $k(W/mK)$	Specific heat capacity $c\ (J/kgK)$
Workpiece Al7075	2810	130	960
Cutting Tool Uncoated WC	11900	110	406

Feed rate value was selected as 0.05 mm/rev whereas the cutting speed values of 100 m/min, 150 m/min and 200 m/min were chosen. The depth of cut was constant and equal to 3.5 mm.

For the temperature measurement with the thermocouples attached to the tool, K-type thermocouples with diameter of 0.08 mm and 0.13 mm were used. Holes having 0.5 mm diameter were drilled on the rake and flank faces using EDM in order to attach the thermocouples (Figure 17). Drilling the hole very near to cutting-edge may result in the breakage of tool. Hence, the holes were made at a specific distance from the cutting-edge. Then the exact position of the holes was measured using a Dino-Lite digital microscope, and these values were considered while comparing the experimental and model results. In order to fix the thermocouple in the hole without affecting the thermal conductivity of the environment, Air Set Cements were used.

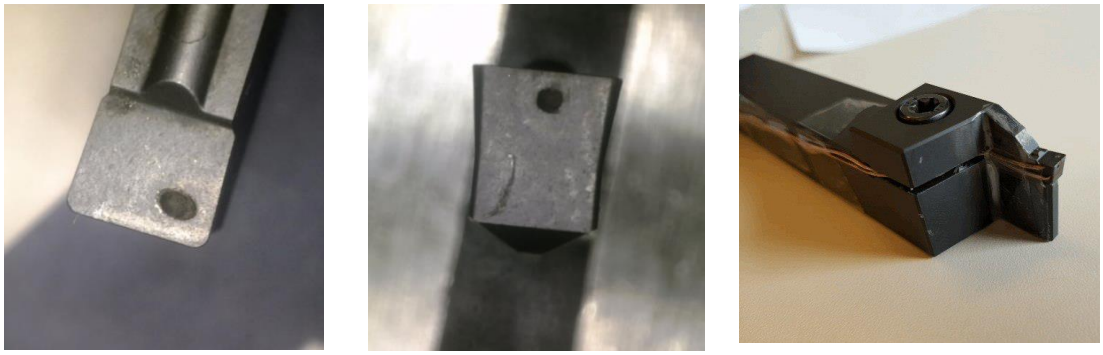

(a) (b) (c)

Figure 17. Thermocouple holes on the (a) rake face, (b) flank face drilled with EDM, (c) thermocouples embedded in the cutting tool.

In addition to thermocouples, the FLIR A325 SC IR thermal camera is used for the measurement of maximum cutting temperature. A special fixture is designed to place the camera in the lathe. Also, a special lens which conducts infrared lights is used for the protection of camera lens from the chip. It was observed by several controlled experiments that this protective lens does not affect the results.

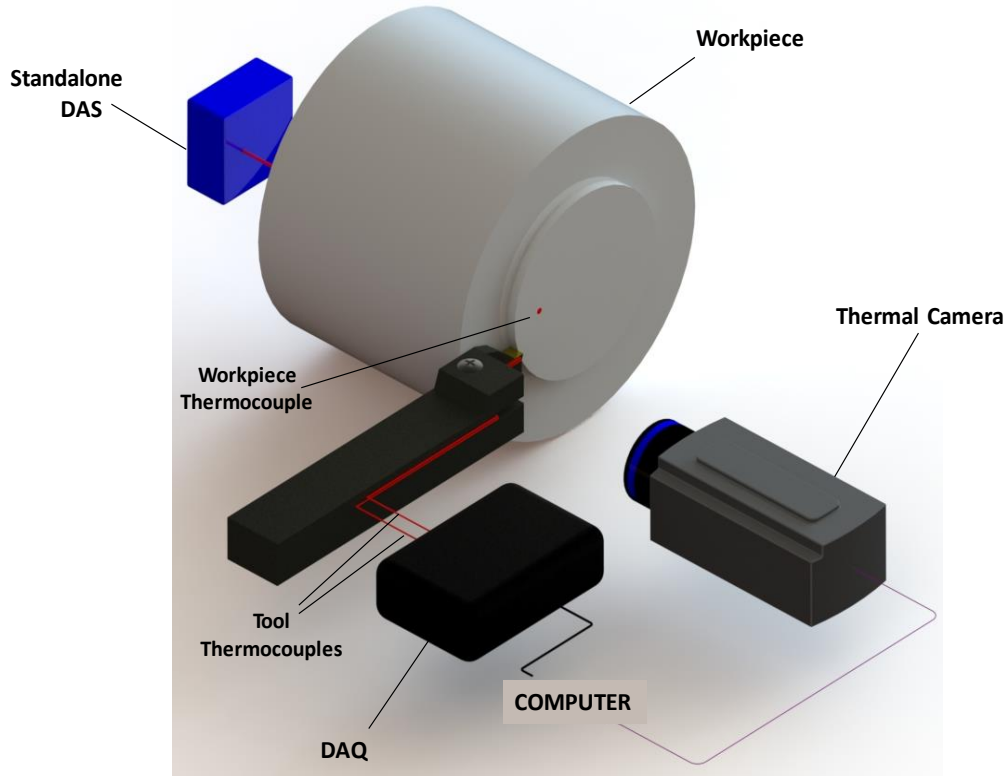

(a)

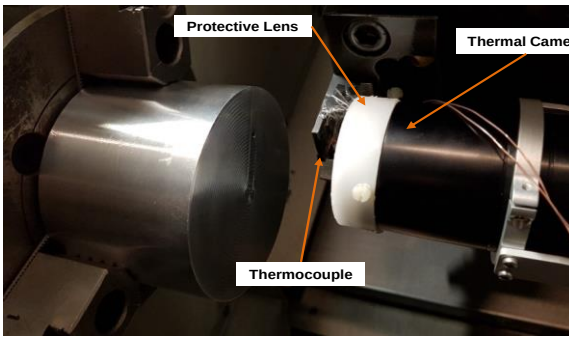

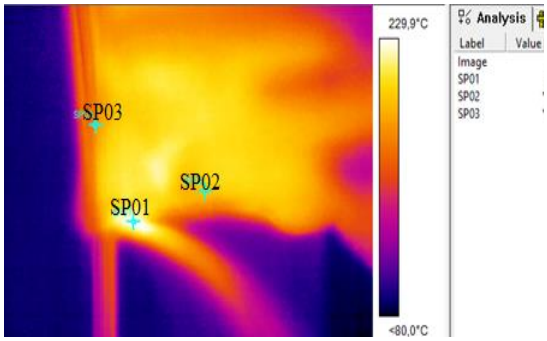

(b) (c)

Figure 18. (a) Schematic of test setup for the temperature measurement with thermocouples and thermal camera (b) Test setup (c) A sample measurement with the thermal camera.

Figure 18.a. shows the setup for the temperature measurement with the thermocouples and thermal camera. The thermocouple data are transferred to computer using a DAQ, making it possible to observe the results during the test. The data obtained from thermal camera are transferred to computer with a LAN cable. A sample measurement can be seen in Figure 8.b.

For measuring the temperature with the thermocouples attached to the workpiece, K-type thermocouples were used (Figure 19). Due to the rotation of workpiece in turning operation, temperature measurement becomes challenging. Hence, a new technique is used to measure workpiece temperatures in this study. Figure 19 shows the experimental setup in which a miniature standalone data acquisition system (DAS) is also rotating with the workpiece. As it is shown in Figure 19, the DAS is mounted on the spindle with a special fixture. The data is recorded in this data acquisition card during the tests. The card is removed and attached to computer to gather the data after the test is finished.

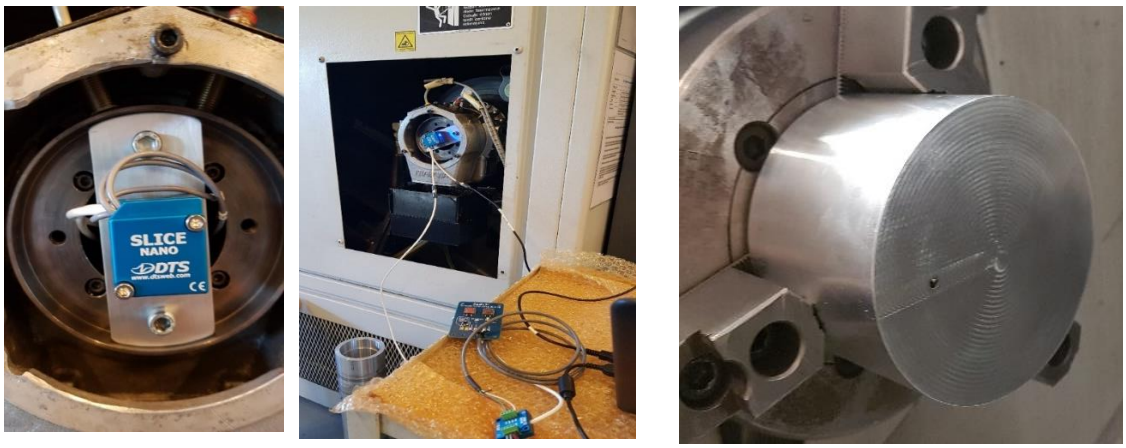

(a) (b)

Figure 19. (a) DAS setup on the spindle for temperature measurement of workpiece (b) The position of the thermocouple on the workpiece.

The experimental results of the thermocouple and thermal camera measurements together with the simulation predictions are reported in Table 2. These results report the temperature of a specific point on the tool (where the thermocouples are attached). In addition, the results of measurements and model prediction for workpiece temperature are reported in Table 3.

Table 2. Comparison of thermal camera results with thermocouple and model predictions for Al7075.

#	Vc (m/min)	Rake Face Temperature ($°C$)				Flank Face Temperature ($°C$)			
		TCM*	TC**	Model	Error %	TCM	TC	Model	Error %
1	100	185	180	210	14	150	168	185	16
2	150	193	184	220	16	165	172	192	16
3	200	195	210	230	13	178	200	210	11

*TCM: Thermal Camera , **TC: Thermocouple

Table 3. Comparison of measured and model predictions for workpiece temperature for Al7075.

#	Cutting Speed (m/min)	TC ($°C$)	Model Prediction ($°C$)	Error (%)
1	100	80	110	30
2	150	100	120	20
3	200	120	130	8

According to Table 2, maximum error of 16% and average error of 14% was observed between the measured and predicted tool temperature. In addition, a good agreement for the workpiece temperature was observed between model prediction and measurement results where the average error is 19%.

Another set of experiments were conducted using AISI1050 steel as the workpiece material for which the thermal properties are summarized in V_{ch} is the chip velocity in m/min.

Table 4. In these tests, only the thermocouples are used to measure the temperature at the rake and flank faces. These experiments were done using feed rate values of 0.05 mm/rev and 0.1 mm/rev, cutting speed values of 100 m/min, 200 m/min, and 250 m/min and depth of cut of 3 mm. Similar to first set of experiments, tools with 5° rake angle and 7° clearance angle were used. In order to study the effect of cutting-edge geometry, tools having 35 μm and 50 μm cutting-edge radius were chosen for the tests. The coefficients of Johnson-Cook equation for AISI1050 are $\mathrm{A} = 880, \mathrm{B} = 500, \mathrm{n} = 0.234, \mathrm{m} = 0.0134,$ and $\upsilon = 1$ [101]. The sliding friction coefficient for AlSI1050-WC pair is defined using

the calibrated equation as [99]:

$$\mu_{sl} = 0.398 + 6.12 \times 10^{-4} V_{ch} \quad (206)$$

V_{ch} is the chip velocity in m/min.

Table 4. Thermal properties of AISI1050 and the cutting tool.

	Density (kg/m^3)	Thermal conductivity $k(W/mK)$	Specific heat capacity $c\ (J/kgK)$
Workpiece AISI1050	7800	54	500
Cutting Tool Uncoated WC	11900	110	406

The results of the measurements for the rake face temperature can be seen in Table 5. It should be again noted here that these results are measured with a thermocouple located on the rake face, and the model results are calculated correspondingly. As can be seen from the results the maximum and average error was calculated to be 12% and 8%, respectively.

Table 5. Comparison of experiment results and model predictions for temperature at the rake face for AISI1050.

#	Feed rate (mm/rev)	Cutting-edge radius (μm)	Cutting speed (m/min)	Rake temperature $(°C)$		Error (%)
				Measurement	Model prediction	
1	0.05	35	100	350	360	3
2	0.05	35	200	370	415	12
3	0.05	35	250	400	438	9
4	0.05	50	100	360	385	6
5	0.05	50	200	375	416	11
6	0.05	50	250	410	433	5

Table 6 shows the thermocouple measurement results and its comparison with the developed model predictions at the flank face. These results show the temperature on a specified point on the tool, where the thermocouples are placed.

Table 6. Comparison of model prediction with thermocouple measurement results for the flank face temperature at a specific point for AISI1050.

#	Feed rate (mm/rev)	Cutting-edge radius (μm)	Cutting speed (m/min)	Flank temperature ($°C$)		Error (%)
				Measurement	Model prediction	
1	0.05	35	100	300	359	20
2	0.05	35	200	330	380	15
3	0.05	35	250	360	452	23
4	0.1	35	100	380	376	1
5	0.1	35	200	400	350	13
6	0.05	50	100	330	390	18
7	0.05	50	200	400	420	5
8	0.05	50	250	450	510	13
9	0.1	50	100	350	410	17
10	0.1	50	200	430	440	2

Comparing the model predictions with the measured results for flank temperature in Table 6, the average error of 13% and maximum error of 23% was calculated. According to these data, flank face temperature can be decreased using lower cutting speed, lower feed rate, and smaller cutting-edge radius.

3.2. Oblique Cutting Experiments

In order to verify the proposed model, experiments were conducted on Mori Seiki NL1500 CNC lathe. Uncoated TPGN WC inserts without chip breaker was used (Figure 20). During the experiments, the temperature on the rake and flank faces were measured using K-type thermocouples with diameter of 0.08mm and 0.13mm. In order to implement the thermocouples in the tool, some fine holes of 0.5 mm diameter were drilled

on the rake and flank faces using EDM, which are shown in Figure 21. Drilling the hole very near to cutting edge may result in the breakage of tool. Hence, the holes were made at a specific distance from the cutting edge. Then the exact position of the holes was measured using a Dino-Lite microscope and these values were considered while comparing the experimental and model results. In order to fix the thermocouple in the hole without affecting the thermal conductivity of the environment, Air Set Cements were used. The test setup can be seen in Figure 21.

For the workpiece, tubes of AISI1050 and Al7075 with 2mm thickness were prepared and experiments were conducted in dry cutting condition. The cutting-edge radius of inserts were measured using NanoFocus, µsurf confocal microscope. The tool has cutting-edge radius of 30 and 50 µm, rake angle of 5°, clearance angle of 7°, and inclination angle of 7°. The thermal properties of the tool and workpiece can be seen in Table 1. The coefficients of Johnson-Cook equation for aluminum and steel which were calibrated from orthogonal cutting tests [101] are reported in Table 1, as well. The sliding friction coefficients are calibrated experimentally [99] for Al7075-WC and AISI1050-WC pairs respectively as:

$$\mu_{sl} = 5 \times 10^{-7} V_{ch} - 7 \times 10^{-4} V_{ch} + 0.4258 \quad (207)$$

$$\mu_{sl} = 0.398 + 6.12 \times 10^{-4} V_{ch} \quad (208)$$

where V_{ch} is the chip velocity in m/min.

Table 7. Properties of cutting tool and workpiece.

	Density (kg/m^3)	Thermal conductivity $k(W/mK)$	Specific heat capacity $c\ (J/kgK)$	Johnson-Cook Coefficients (A, B, n, m, υ)
Workpiece Al7075	2810	130	960	286,575,0.71,0.024,1.6
Workpiece AISI1050	7800	54	500	880,500,0.234,0.0134,1
Cutting Tool Uncoated WC	11900	110	406	-

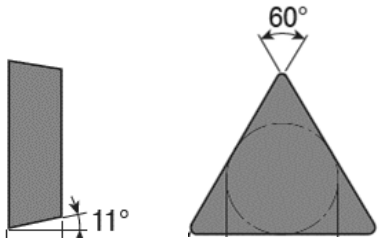

Figure 20. TPGN WC tool used in the oblique verification tests.

Cutting speed for the AISI1050 experiments were 100, 200, and 250 m/min. For the Al7075 tests 100, 150, and 200 m/min of cutting speed was used. Feed rates of 0.05 and 0.1 mm/rev was used in the experiments.

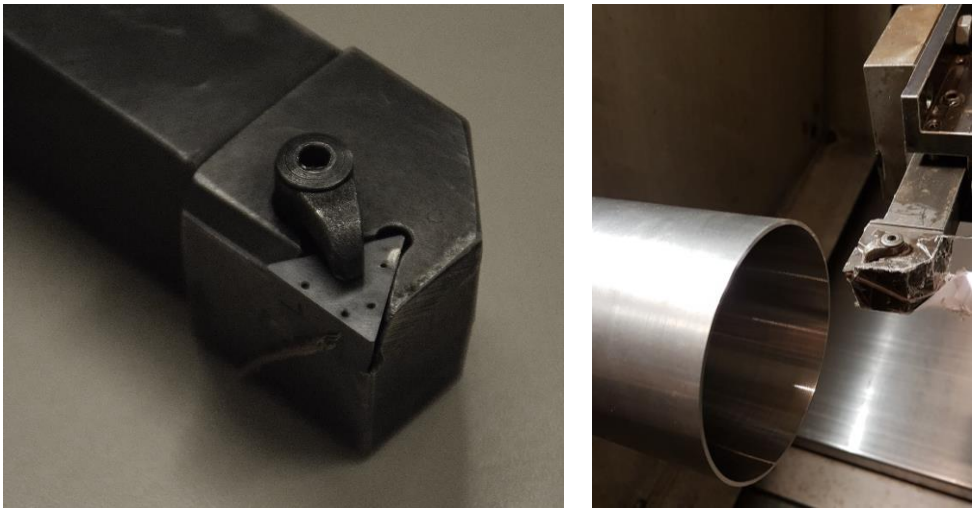

(a) (b)

Figure 21. (a) Thermocouple holes on the rake and flank face drilled with EDM, (b) Experimental setup for oblique cutting tests.

The measurements for the rake face temperature can be seen in Table 8. It should be again noted here that these results are measured with the thermocouples located on the rake and flank faces at a specific distance from cutting area, and the model results are calculated correspondingly for the same points. According to Table 8, the maximum and average error in the prediction of rake temperature was calculated to be 19% and 12%, respectively. The maximum and average error in the calculation of flank temperature, while cutting AISI1050 was 18% and 10%, respectively.

Table 8. Comparison of measured results and model predictions for rake temperature-AISI1050.

#	Cutting edge radius (μm)	Cutting speed (m/min)	Feed (mm/rev)	Measured temperature ($°C$)	Predicted temperature ($°C$)	Error (%)
1	30	100	0.05	270	250	14
2	30	200	0.05	340	330	6
3	30	250	0.05	400	450	12
4	30	100	0.1	300	280	19
5	30	200	0.1	360	380	5
6	30	250	0.1	410	480	17

Table 9. Comparison of measured results and model predictions for flank temperature – Al7075.

#	Cutting edge radius (μm)	Cutting speed (m/min)	Feed (mm/rev)	Measured temperature ($°C$)	Predicted temperature ($°C$)	Error (%)
1	30	100	0.05	140	160	14
2	30	200	0.05	180	190	6
3	30	250	0.05	210	230	10
4	30	100	0.1	160	190	18
5	30	200	0.1	200	210	5
6	30	250	0.1	220	240	9
7	50	100	0.05	145	170	17
8	50	200	0.05	180	200	11
9	50	250	0.05	220	235	7
10	50	100	0.1	155	185	16
11	50	200	0.1	220	205	7
12	50	250	0.1	240	250	4

3.3. Turning Experiments

Experimental studies were conducted on Mori Seiki NL1500 CNC lathe in Sabanci University Manufacturing Research Laboratory. Uncoated WC inserts (SECO TPGN, Figure 20) without chip breaker was used. The rake of the tools was 5 ° and the clearance angle was 7°. AISI-1050 and Al7075 was used as the workpiece material. The thermal properties of the tool and workpiece used can be seen in Table 10.

Table 10. Thermal properties of tool and workpiece used in the turning experiments.

	Density (kg/m^3)	Thermal conductivity (W/mK)	Specific heat capacity (J/kgK)	Johnson-Cook Coefficients (A, B, n, m, υ)
Workpiece Al7075	2810	130	960	286,575,0.71,0.024,1.6
Workpiece AISI1050	7800	54	500	880,500,0.234,0.0134,1
Cutting Tool Uncoated WC	11900	110	406	-

In order to study the effect of nose radius on cutting temperature, inserts with four different nose radii were used in the experiments. The geometric properties of the tool and cutting parameters are presented in Table 11. The depth of cut for tools with 0.2, 0.4 and 0.8 mm nose radii was 0.8 mm. For the tool with 1.2 mm of nose radius, depth of cut was equal to 1.5 mm.

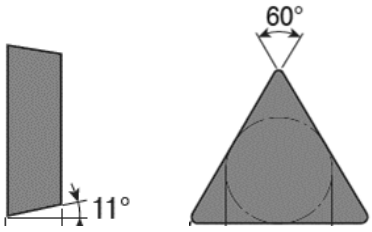

Figure 22. TPGN WC tool used in the turning verification tests.

Table 11. Cutting parameters of turning experiments.

Rake angle $\alpha(°)$	Clearance angle $\lambda(°)$	Inclination angle $i(°)$	Feed rate $f(\frac{mm}{dev})$	Cutting speed $V_c(\frac{m}{dak})$	Cutting-edge radius $r(mm)$
5	7	7	0.05	100	0.2
			0.1	150	0.4
				200	0.8
				250	1.2

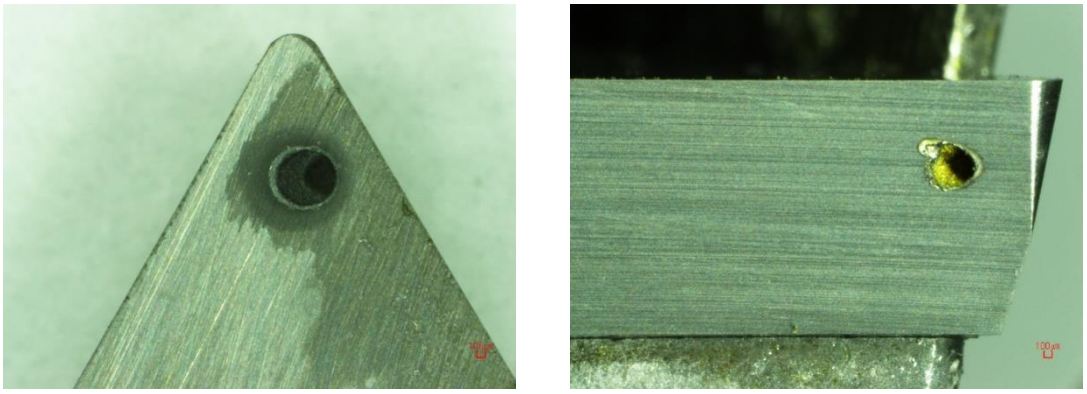

(a) (b)

Figure 23. Holes drilled on (a) Rake and (b) Flank faces for turning tests.

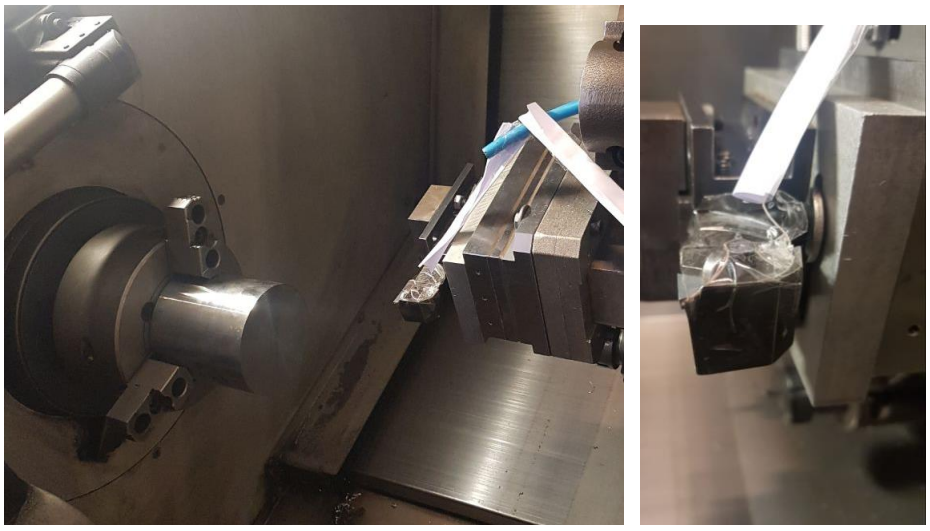

Figure 24. Experimental setup for turning tests.

The aim of the experiments is to measure the temperature of the rake face and flank face. For this purpose, temperature measurements with thermocouples were performed. In this study, K-type thermocouples with diameter of 0.13mm were used. In order to implement the thermocouples in the tool, some fine holes of 0.5 mm diameter were drilled on the rake and flank faces using EDM, which are shown in Figure 23. Drilling the hole very near to cutting edge may result in the breakage of tool. Hence, the holes were made at a specific distance from the cutting edge. Then the exact position of the holes was measured using a Dino-Lite microscope and these values were considered while comparing the experimental and model results. In order to fix the thermocouple in the hole without affecting the thermal conductivity of the environment, Air Set Cements were used. The test setup can be seen in Figure 21. The thermocouple data are transferred to computer using a DAQ, making it possible to observe the results during the test. The cutting process is continued until the temperature reaches a steady-state condition.

Table 12. Comparison of model prediction with experimental results for rake face temperature measurements – AISI1050

#	Feed (mm/rev)	Cutting Speed (m/min)	Nose Radius (mm)	Depth of Cut (mm)	Measured Temperature (°C)	Predicted Temperature (°C)	Error (%)
1	0.05	100	1.2	1.5	200	190	5
2	0.05	200	1.2	1.5	240	210	13
3	0.05	250	1.2	1.5	260	215	17
4	0.1	100	1.2	1.5	290	280	3
5	0.1	200	1.2	1.5	320	305	5
6	0.1	250	1.2	1.5	380	310	18
7	0.05	100	0.8	1	160	185	16
8	0.05	200	0.8	1	200	210	5
9	0.05	250	0.8	1	230	270	17
10	0.1	100	0.8	1	200	220	10
11	0.1	200	0.8	1	240	250	4
12	0.1	250	0.8	1	310	270	13
13	0.05	100	0.4	0.8	150	180	20
14	0.05	200	0.4	0.8	190	205	8
15	0.05	250	0.4	0.8	220	265	20
16	0.1	100	0.4	0.8	185	210	14
17	0.1	200	0.4	0.8	230	250	9
18	0.1	250	0.4	0.8	280	255	9
19	0.05	100	0.2	0.8	145	180	24
20	0.05	200	0.2	0.8	190	200	5
21	0.05	250	0.2	0.8	210	259	23
22	0.1	100	0.2	0.8	180	206	14
23	0.1	200	0.2	0.8	230	245	7
24	0.1	250	0.2	0.8	235	265	13

Table 13. Comparison of model prediction with experimental results for flank face temperature measurements – AISI1050

#	Feed (mm/rev)	Cutting Speed (m/min)	Nose Radius (mm)	Depth of Cut (mm)	Measured Temperature (°C)	Predicted Temperature (°C)	Error (%)
1	0.05	100	1.2	1.5	200	160	20
2	0.05	200	1.2	1.5	250	205	18
3	0.05	250	1.2	1.5	280	240	14
4	0.1	100	1.2	1.5	260	220	15
5	0.1	200	1.2	1.5	340	315	7
6	0.1	250	1.2	1.5	350	380	9
7	0.05	100	0.8	1	195	165	15
8	0.05	200	0.8	1	240	195	19
9	0.05	250	0.8	1	250	200	20
10	0.1	100	0.8	1	170	190	12
11	0.1	200	0.8	1	240	210	13
12	0.1	250	0.8	1	250	225	10
13	0.05	100	0.4	0.8	185	157	15
14	0.05	200	0.4	0.8	200	185	7
15	0.05	250	0.4	0.8	210	190	10
16	0.1	100	0.4	0.8	165	180	9
17	0.1	200	0.4	0.8	230	205	11
18	0.1	250	0.4	0.8	235	215	9
19	0.05	100	0.2	0.8	180	155	14
20	0.05	200	0.2	0.8	210	185	12
21	0.05	250	0.2	0.8	220	190	14
22	0.1	100	0.2	0.8	165	190	15
23	0.1	200	0.2	0.8	225	200	11
24	0.1	250	0.2	0.8	230	205	11

Table 14. Comparison of model prediction with experimental results for rake face temperature measurements – AL7075.

#	Feed (mm/rev)	Cutting Speed (m/min)	Nose Radius (mm)	Depth of Cut (mm)	Measured Temperature (°C)	Predicted Temperature (°C)	Error (%)
1	0.05	100	1.2	1.5	105	96	9
2	0.05	150	1.2	1.5	110	104	5
3	0.05	200	1.2	1.5	125	120	4
4	0.05	250	1.2	1.5	130	123	5
5	0.1	100	1.2	1.5	150	138	8
6	0.1	150	1.2	1.5	160	139	13
7	0.1	200	1.2	1.5	165	154	7
8	0.1	250	1.2	1.5	168	161	4
9	0.05	100	0.8	1	92	78	15
10	0.05	150	0.8	1	99	81	18
11	0.05	200	0.8	1	110	89	19
12	0.05	250	0.8	1	113	90	20
13	0.1	100	0.8	1	100	120	20
14	0.1	150	0.8	1	110	130	18
15	0.1	200	0.8	1	118	140	19
16	0.1	250	0.8	1	120	145	21
17	0.05	100	0.4	0.8	85	105	24
18	0.05	150	0.4	0.8	90	110	22
19	0.05	200	0.4	0.8	96	125	30
20	0.05	250	0.4	0.8	100	130	30
21	0.1	100	0.4	0.8	95	110	16
22	0.1	150	0.4	0.8	105	115	10
23	0.1	200	0.4	0.8	115	140	22
24	0.1	250	0.4	0.8	120	150	25
25	0.05	100	0.2	0.8	80	100	25
26	0.05	150	0.2	0.8	87	110	26
27	0.05	200	0.2	0.8	90	115	28
28	0.05	250	0.2	0.8	98	123	26
29	0.1	100	0.2	0.8	85	105	24
30	0.1	150	0.2	0.8	95	120	26
31	0.1	200	0.2	0.8	110	135	23
32	0.1	250	0.2	0.8	115	145	26

Table 15. Comparison of model prediction with experimental results for flank face temperature measurements – AL7075.

#	Feed (mm/rev)	Cutting Speed (m/min)	Nose Radius (mm)	Depth of Cut (mm)	Measured Temperature (°C)	Predicted Temperature (°C)	Error (%)
1	0.05	100	1.2	1.5	105	90	14
2	0.05	150	1.2	1.5	110	125	14
3	0.05	200	1.2	1.5	140	120	14
4	0.05	250	1.2	1.5	140	126	10
5	0.1	100	1.2	1.5	130	128	2
6	0.1	150	1.2	1.5	138	134	3
7	0.1	200	1.2	1.5	145	134	8
8	0.1	250	1.2	1.5	149	156	5
9	0.05	100	0.8	1	90	75	17
10	0.05	150	0.8	1	110	83	25
11	0.05	200	0.8	1	115	87	24
12	0.05	250	0.8	1	120	92	23
13	0.1	100	0.8	1	115	110	4
14	0.1	150	0.8	1	120	115	4
15	0.1	200	0.8	1	125	135	8
16	0.1	250	0.8	1	125	140	12
17	0.05	100	0.4	0.8	90	105	17
18	0.05	150	0.4	0.8	95	120	26
19	0.05	200	0.4	0.8	105	130	24
20	0.05	250	0.4	0.8	110	135	23
21	0.1	100	0.4	0.8	100	110	10
22	0.1	150	0.4	0.8	103	115	12
23	0.1	200	0.4	0.8	110	125	14
24	0.1	250	0.4	0.8	115	130	13
25	0.05	100	0.2	0.8	97	105	8
26	0.05	150	0.2	0.8	100	115	15
27	0.05	200	0.2	0.8	108	130	20
28	0.05	250	0.2	0.8	115	132	15
29	0.1	100	0.2	0.8	95	105	11
30	0.1	150	0.2	0.8	105	115	10
31	0.1	200	0.2	0.8	108	120	11
32	0.1	250	0.2	0.8	110	130	18

3.4. Experiments Using Worn Tools

3.4.1. Orthogonal Cutting with a Worn Tool

In order to verify the proposed model for worn tool, experimental study was conducted. In these tests grooving WC tool (KennaMetal A4G0405M04U04B KC5025) was used. The tool has cutting edge radius of 70 µm, rake angle of 5° and clearance angle of 7°. The workpiece is selected to be AISI 1050. Measurements are performed on Mori Seiki Lathe. The depth of cut was equal to $3.5\,mm$. The cutting speed was $90\,and\,180\,m/min$. Cutting tests were continued until reaching the $VB = 150\,\mu m$ and temperature was measured during the test. K-type thermocouples with diameter of 0.08mm and 0.13mm were used in the tool during the tests to measure the tool temperature. In order to implement the thermocouples in the tool, some fine holes of 0.5 mm diameter were drilled on the rake and flank faces using EDM. Dino-Lite microscope and Nikon digital microscope (ShuttlePix- P-400R) were used to measure the flank wear after each test. Measurement setup is shown in the Figure 25.

Figure 25. Measurement setup for wear test in orthogonal condition.

The measured temperature and flank wear after each test are summarized in Table 16 and Table 17. The tests started with an unused tool and cutting speed was set to 90 m/min.

Temperature on rake and flank face was measured. The tests were continued until reaching $VB = 0.08\,mm$. Then using the same tool, more cutting tests were performed with $V_c = 180\,m/min$ and the flank temperature was recorded. In addition, after each test the flank wear was measured. Figure 26 shows some sample of wear measurements.

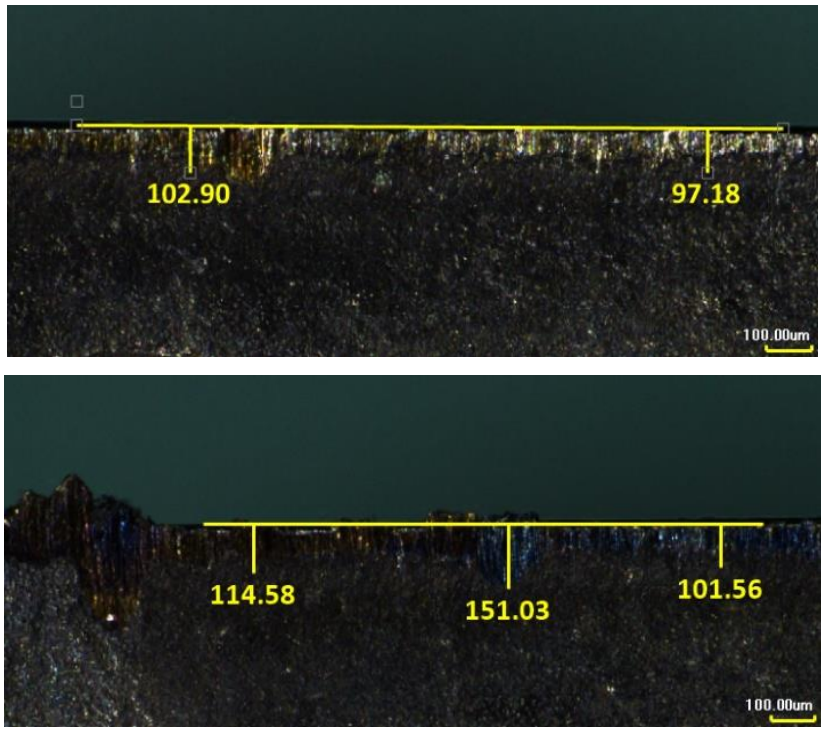

Figure 26. Wear measurement using Nikon microscope in orthogonal cutting.

The experimental results were compared with the model prediction to verify the proposed model. The result of this comparison is listed in Table 16 and Table 17 for flank and rake face, respectively.

Table 16. Comparison between test results and model predictions for flank temperature vs flank wear, maximum error=16% and average error=8%.

#	$VB\ (\mu m)$	Cutting speed (m/min)	Predicted flank temperature $(°C)$	Measured flank temperature $(°C)$	Error (%)
1	0	90	366	310	16
2	10	90	359	320	12
3	20	90	350	330	6
4	30	90	368	330	12
5	40	90	369	350	5
6	50	90	369	360	3
7	60	90	389	370	5
8	70	90	403	370	9
9	80	90	415	370	12
10	90	180	480	460	5
11	100	180	483	464	4
12	110	180	491	469	5
13	120	180	493	482	2
14	150	180	521	495	5

Table 17. Comparison between test results and model predictions for rake temperature vs flank wear, maximum error=18% and average error=11%

#	$VB\ (\mu m)$	Cutting speed (m/min)	Predicted rake temperature $(°C)$	Measured rake temperature $(°C)$	Error (%)
1	0	90	431	380	13
2	10	90	451	380	18
3	20	90	445	380	17
4	30	90	433	385	13
5	40	90	428	400	7
6	50	90	432	400	8
7	60	90	441	400	10
8	70	90	451	420	7
9	80	90	465	425	9

3.4.2. Oblique Cutting with a Worn Tool

In order to investigate the effect of flank wear on the cutting temperature and verify the proposed model, an experimental study was conducted. For this purpose, some uncoated WC TPGN inserts were worn in different levels beforehand and the flank wear were measured using Dino-Lite and Nikon digital microscopes (ShuttlePix- P-400R). Experiments were done on AISI1050 tubes. K-type thermocouples were embedded in the drilled holes on rake and flank faces of inserts. The cutting parameters in the experiments are reported in Table 18. The rake, clearance and inclination angle of the cutting tools were 5°, 7°, and 7° respectively. The cutting-edge radius of the tools were measured to be 30 μm.

Table 18. Cutting parameters for temperature measurements of worn tool.

Depth of cut (mm)	Feed rate $(\frac{mm}{rev})$	Cutting speed $(\frac{m}{min})$	Wear Value
1.5	0.05	100	0
		200	40
		250	80
			120

Table 19. Comparison of measured results and model predictions for flank temperature in tests with worn tools, $\alpha = 5°$, $\lambda = 7°$, $i = 7°$, $feed = 0.05\ mm/rev$, $r = 30\ \mu m$

#	Flank Wear (μm)	Cutting Speed (m/min)	Measured Temperature ($°C$)	Model Prediction ($°C$)	Error (%)
1	0	100	140	160	14
2	40	100	145	160	10
3	80	100	155	175	13
4	120	100	175	210	20
5	0	200	180	190	6
6	40	200	185	205	11
7	80	200	195	225	15
8	120	200	210	240	14
9	0	250	210	230	10
10	40	250	220	250	14
11	80	250	230	275	20
12	120	250	260	300	15

Table 20. Comparison of measured results and model predictions for rake temperature in tests with worn tools, $\alpha = 5°$, $\lambda = 7°$, $i = 7°$, $feed = 0.05\ mm/rev$, $r = 30\ \mu m$

#	Flank Wear (μm)	Cutting Speed (m/min)	Measured Temperature ($°C$)	Model Prediction ($°C$)	Error (%)
1	0	100	270	250	7
2	40	100	285	245	14
3	80	100	310	295	5
4	120	100	330	320	3
5	0	200	340	330	3
6	40	200	360	330	8
7	80	200	385	365	5
8	120	200	405	430	6
9	0	250	400	450	13
10	40	250	415	430	4
11	80	250	435	480	10
12	120	250	460	510	11

3.4.3. Turning with a Worn Tool

In order to verify the proposed model, experimental study was conducted. In these tests WC SECO tools were used. The tool had cutting edge radius of 30 µm, rake angle of 5° and clearance angle of 7°. The workpiece is selected to be AISI 1050 and the measurements are performed on Mori Seiki Lathe. The depth of cut was equal to 0.8 and $1.5\ mm$. The cutting speed was $250\ m/min$. The nose radius of the cutting tool was selected to be 0.4 and 1.2 mm. Cutting tests were performed using pre-worn tools with wear value equal to $VB = 40, 80, 100\ \mu m$. The temperature was measured during the test with K-type thermocouples with diameter of 0.13mm. Dino-Lite microscope and Nikon digital microscope (ShuttlePix- P-400R) were used to measure the flank wear after each test. The measured temperature and model predictions for rake and flank faces are summarized in Table 21 and Table 22, respectively.

Table 21. Comparison of model prediction with experimental results for rake temperature (average error= 11%).

#	VB (μm)	Cutting Speed (m/min)	Nose Radius (mm)	Depth of Cut (mm)	Measured (°C)	Model Prediction (°C)	Error (%)
1	0	100	1.2	1.5	290	280	3
2	40	100	1.2	1.5	295	280	5
3	80	100	1.2	1.5	310	290	6
4	100	100	1.2	1.5	330	295	11
5	0	250	1.2	1.5	380	310	18
6	40	250	1.2	1.5	385	315	18
7	80	250	1.2	1.5	395	335	15
8	100	250	1.2	1.5	420	350	17
9	0	100	0.4	0.8	185	210	14
10	40	100	0.4	0.8	190	210	11
11	80	100	0.4	0.8	195	215	10
12	100	100	0.4	0.8	210	220	5
13	0	250	0.4	0.8	280	255	9
14	40	250	0.4	0.8	290	260	10
15	80	250	0.4	0.8	305	270	11
16	100	250	0.4	0.8	315	275	13

Table 22. Comparison of model prediction with experimental results for flank temperature (average error = 8%).

#	VB (μm)	Cutting Speed (m/min)	Nose Radius (mm)	Depth of Cut (mm)	Measured (°C)	Model Prediction (°C)	Error (%)
1	0	100	1.2	1.5	260	220	15
2	40	100	1.2	1.5	270	250	7
3	80	100	1.2	1.5	300	290	3
4	100	100	1.2	1.5	330	370	12
5	0	250	1.2	1.5	350	380	9
6	40	250	1.2	1.5	360	400	11
7	80	250	1.2	1.5	370	420	14
8	100	250	1.2	1.5	395	435	10
9	0	100	0.4	0.8	165	180	9
10	40	100	0.4	0.8	175	200	14
11	80	100	0.4	0.8	190	215	13
12	100	100	0.4	0.8	210	240	14
13	0	250	0.4	0.8	235	215	9
14	40	250	0.4	0.8	240	230	4
15	80	250	0.4	0.8	255	250	2
16	100	250	0.4	0.8	280	300	7

4. DISCUSSION AND RESULTS

4.1. Orthogonal Cutting

4.1.1. Simulation Results

The proposed model can be used to predict the temperature for different cutting conditions and tool geometry. Figure 27 shows an example of model prediction for the conditions that are summarized in Table 23. As it is clear in the Figure 27, temperature distribution on the flank face shows an increasing-decreasing behavior. In the previous studies, due to the absence of the third deformation zone, the temperature of flank face has its maximum value at the tool tip, and it has a decreasing trend towards the flank face after this point. Therefore, the proposed model is more realistic for the prediction of flank face temperature and the location of its maximum value.

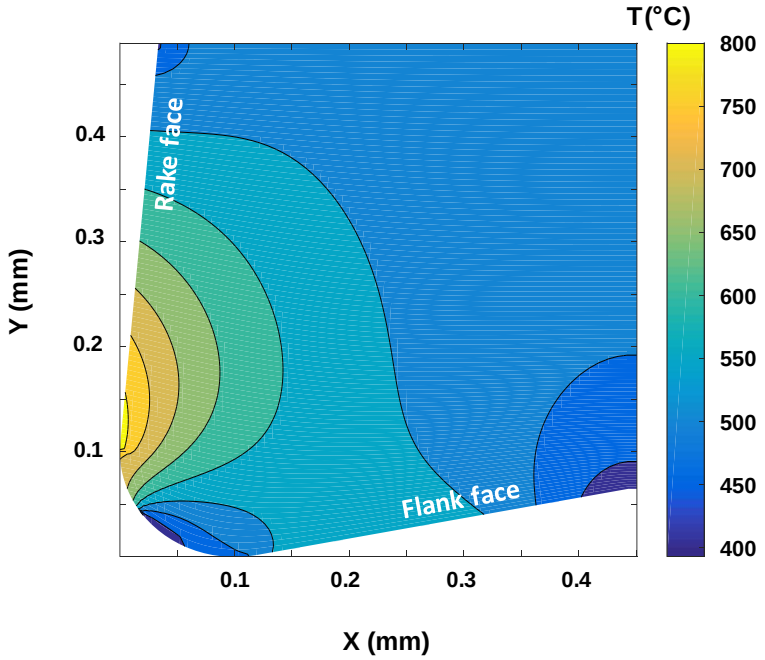

Figure 27. Temperature distribution in the tool obtained from the proposed model.

Table 23. Parameters used for the sample orthogonal simulation

Workpiece-Tool		AISI1050-WC
Cutting speed (m/min)	V_c	250
Feed rate (mm/rev)	f	0.1
Depth of cut (mm)	a_p	3
Rake angle (°)	α	5
Clearance angle (°)	λ	11
Stagnation angle (°)	θ	55
Cutting-edge radius (μm)	r_h	100
Constants for JC equation (AISI 1050)	$A, B, n,$ m, v	880, 500, 0.234, 0.0134, 1
Density of workpiece $(\frac{kg}{m^3})$	ρ	7800
Melting temperature of workpiece $(°C)$	T_m	1460
Heat capacity of workpiece $(J/kg * K)$	c	500
Thermal conductivity of workpiece $(W/(m^2K))$	k	54
Room temperature $(°C)$	T_∞	25
Reference temperature $(°C)$	T_r	25
Fraction of the work converted into heat	χ	0.9
Sliding friction coefficient	μ	0.51
Pressure distribution exponent on rake face	ζ	3
Heat convection coefficient for Air $(W/(m^2K))$	h	20

4.1.2. Effect of the Third Deformation Zone

In most of the previous studies, the effect of cutting-edge radius and the third deformation zone on the temperature distribution inside the tool has not been considered. However, the contact between tool and workpiece has a significant effect on tool temperature due to existence of friction and heat generation in this region. The model prediction with and without the effect of this region are shown in Figure 28. As it can be seen in Figure 28, not only the maximum flank temperature, but also its location on the flank face is affected. In the case of neglecting the heat generation at the third deformation zone i.e. sharp tool, convective boundary conditions arise, and the temperature on the flank face has its

maximum value at the tool tip. As a result, temperature decreases along the flank face. On the other hand, considering the effect of the third deformation zone and heat source at this region, the temperature distribution on the flank face is affected. Firstly, starting from the tool tip, temperature on the flank face increases until it reaches its maximum value at a point and then decreases. This change in the behavior shows that the heat generation at the third deformation zone is critical and important in terms of modelling the temperature distribution at the flank face in order to obtain more realistic results.

Moreover, not only the temperature distribution on the flank face but also the temperature distribution inside the tool changes when the effect of the third deformation zone is taken into account, as can be clearly seen from Figure 28. In Figure 28.b, where the effect of the third deformation zone is neglected, due to the single heat source at the rake face, the temperature distribution inside the tool follows smooth contours. However, when the heat generation at the third deformation zone is taken into account (Figure 28.a) a new and more complicated temperature distribution inside the tool is obtained which is more realistic.

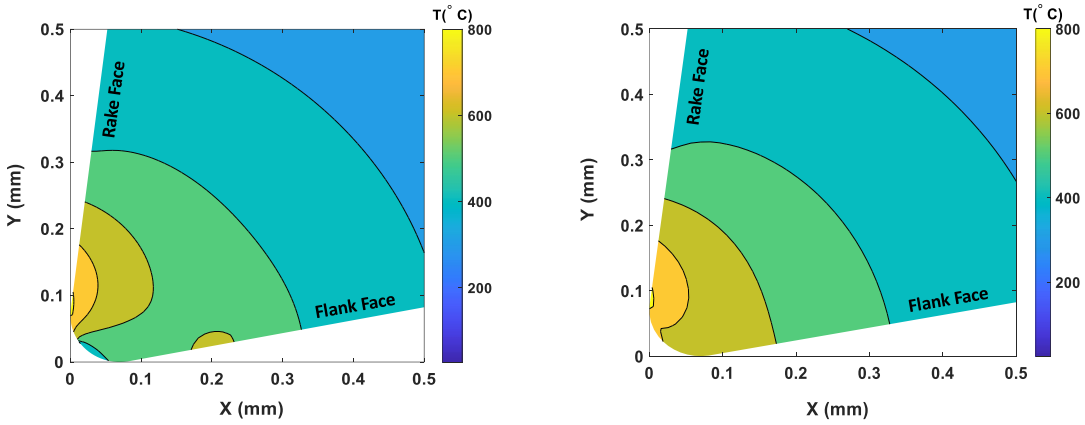

(a) (b)

Figure 28. Comparison of model predictions for temperature distribution in the tool (a) with and (b) without the third deformation zone effect for $V_c = 300m/min$, $f = 0.1\ mm/rev$, $r = 70\mu m$, $\alpha = 7°$, $\lambda = 11°$, uncoated carbide cutting tool and AISI1050 steel.

4.1.3. Effect of Cutting Speed

Cutting speed affects the cutting temperature significantly. As the cutting speed increases both strain rate and friction speed increases which will results in higher heat generation

in all the deformation zones. At the primary shear zone, the shear stress and temperature at the exit of shear band will increase which affects the heat generation in the second and third deformation zones. Moreover, the normal pressure and friction force on tool rake and flank faces increase when shear stress increases. Simulation results for the maximum temperatures at the rake and flank faces for varying rake angles and cutting speeds are presented in Figure 29. It can be seen that 5 times increase in the cutting speed (from 60 m/min to 300 m/min), results in around 80% increase in the maximum temperature (from 600°C to 1100°C) at the rake face. Similarly, 5 times increase in the cutting speed results in around 50% (from 500°C to 700°C) increase in maximum temperature at the flank face. Furthermore, 2 times increase in rake angle, results in 10% decrease in the maximum temperature at the rake and flank faces. In addition, comparing the rake and flank face temperatures it can be concluded that the temperature rise on the rake face is more significant than the flank face with the increase of cutting speed. By increasing the cutting speed, the chip velocity and the velocity on flank face varies almost with the same ratio. On the other hand, the rake contact length increases with the increase of cutting speed while the flank contact length is not affected by the cutting speed. Therefore, higher variation of rake face temperature with the change of cutting speed can be correlated with the increase of contact length on the rake face.

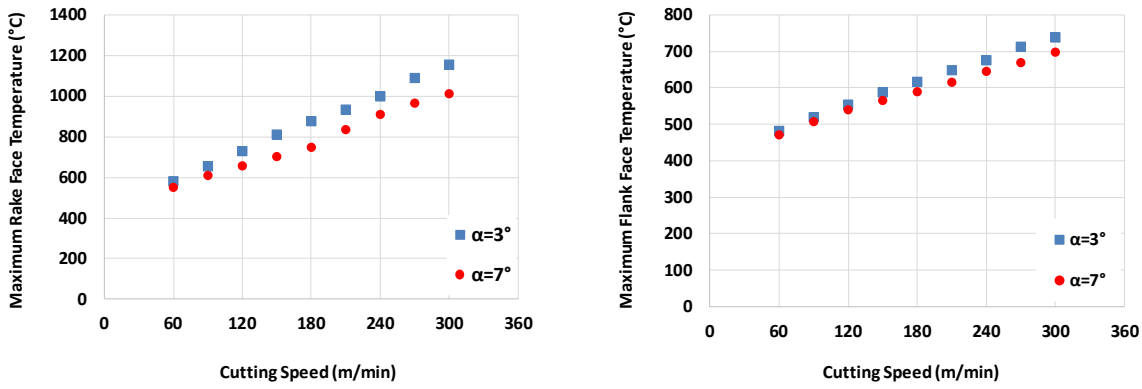

(a) (b)

Figure 29. Effect of cutting speed on maximum temperature at the (a) rake and (b) flank faces for $r = 70\mu m, \lambda = 5°, f = 0.15\ mm/rev$, uncoated carbide tool vs AISI1050 steel

4.1.4. Effect of Rake Angle

The effect of rake angle on the maximum rake and flank faces temperature using the

proposed model is presented in this section. For this purpose, the temperature of rake and flank faces were calculated for $r = 70\ \mu m$, $\lambda = 3°$ and $f = 0.15\ mm/rev$ which are shown in Figure 30. As can be seen from Figure 30, three times increase of rake angle (from 3° to 9°), results in around 20% decrease of the maximum temperature (from 1200°C to 1000°C) at the rake face. The change of maximum flank temperature with three times increase of rake angle is around 10% (from 830 to 750).This is due to the fact that, increasing rake angle reduces the normal stress and friction force on the rake and flank faces, which results in lower heat generation. Moreover, increase of rake angle will decrease the normal pressure at the tool tip, P_0 which is the pressure at the start of the flank contact Therefore, increasing rake angle will decrease the normal pressure on the flank face, as well. As a result, the temperature and its maximum value at the flank contact will reduce.

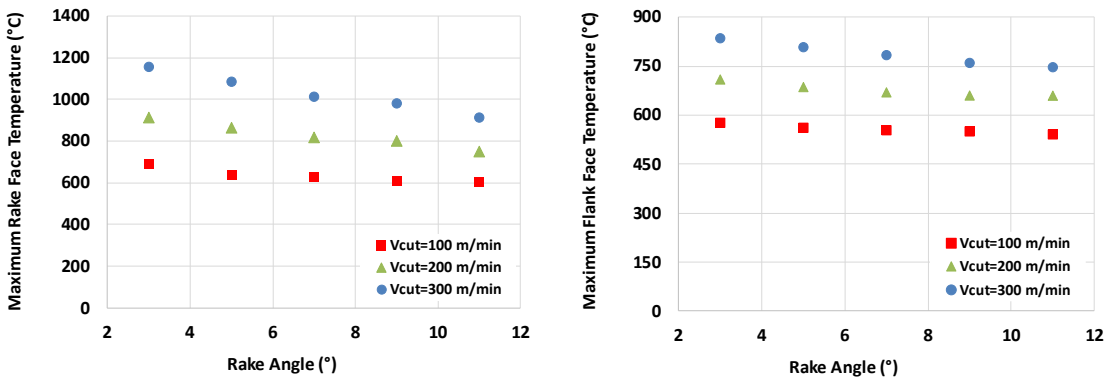

(a) (b)

Figure 30. Effect of rake angle on maximum temperature at the (a) rake and (b) flank faces for $r = 70\mu m, \lambda = 3°, f = 0.15\ mm/rev$, AISI1050 steel.

4.1.5. Effect of Clearance Angle

In this section, the effects of clearance angle on the maximum temperature at the flank face are presented. In the simulations the parameters are selected as $r = 70\mu m$, $\alpha = 3°$ and $feed = 0.15\ m/rev$. The simulations were conducted for two different materials: AISI1050 steel and Al7075 alloy. Figure 31 shows the effect of clearance angle on the maximum flank temperature for different cutting speeds. Increasing clearance angle results in significant drop in the maximum temperature at the flank face where the effect

is higher for larger cutting speeds. According to Figure 31.a. by increasing the clearance angle from 1° to 11°, flank temperature decreases around 45% for AISI1050 steel. A similar trend is observed for the Al7075, which is shown in Figure 31.b. By the change of clearance angle for 10°, the temperature decreases almost 20% for different cutting speeds. Therefore, using larger clearance angles will result in lower flank temperatures. The reason is the decrease of contact length on flank face with the increase of clearance angle, according to Equation (21). However, the temperature variation is more distinct in smaller clearance angles and this change becomes slighter when clearance angle gets larger. On the other hand, increase of clearance angle will make the tool weaker and increases the possibility of tool breakage. Therefore, an optimum value of clearance angle will help to reduce the temperature significantly without effecting the tool strength.

By comparing the results for steel and aluminum, it can be concluded that cutting temperature in steel is higher and more sensitive to the change of clearance angle. Therefore, proper selection of clearance angle for machining of workpiece materials with higher cutting temperatures are crucial in terms of optimization.

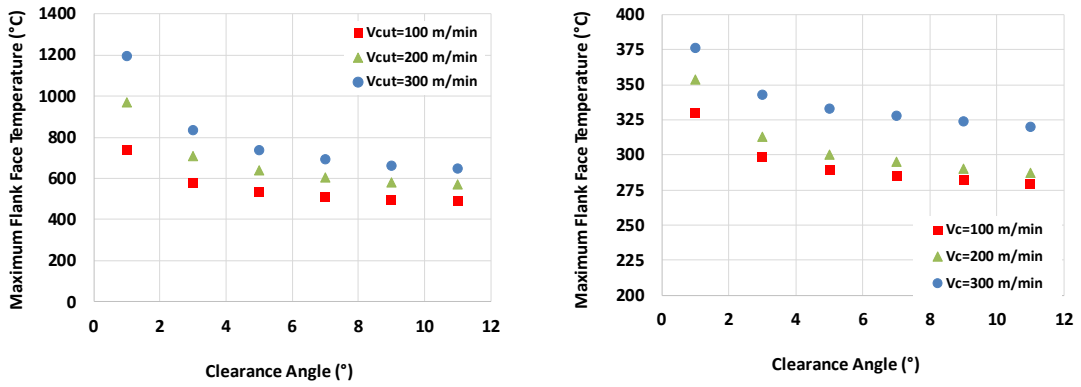

(a) (b)

Figure 31. Effect of clearance angle on maximum flank temperature for $r = 70\mu m, \alpha = 3°, f = 0.15\ mm/rev$, uncoated carbide tool with (a) AISI 1050 steel, and (b) Al7075 alloy.

4.1.6. Effect of Cutting-Edge Radius

The cutting-edge radius is the reason for the existence of the third deformation zone. Therefore, it is important to study the effect of this parameter on the cutting temperature. The result of model prediction for the maximum rake and flank temperature when using

different cutting-edge radii is demonstrated in Figure 32 and Figure 33 for AISI1050 steel and Al7075, respectively. According to these results, as a general conclusion, maximum temperature at the flank face increases with the increase of cutting-edge radius whereas maximum temperature at the rake face is not affected. This can be related to the increase of total contact length in the third deformation zone (l_{c3}) by the increase of cutting-edge radius, which is also addressed by equation (21).

Considering the results in Figure 32.b, increase in the cutting-edge radius 6 times (from $20\mu m$ to $120\mu m$) the maximum temperature increases around 50% for the orthogonal cutting of AISI1050. A similar behavior is shown for the Al7075 in Figure 33 (b). In this case, increase in the cutting-edge radius 6 times results in 15% increase in the maximum temperature at the flank face. This behavior is expected, as the thermal properties of Al7075 is almost 2 times better than AISI1050 in terms of temperature rise. This thermal behavior is also reflected in the behavior of the maximum temperature at the flank face in orthogonal cutting processes. Based on these results, it can be concluded that the correct selection of cutting-edge radius is of great importance considering the effect of different workpiece materials.

Figure 34 shows the variation of flank contact length and maximum temperature at the flank face with the change of clearance angle and cutting-edge radius. Figure 34.a shows that the effect of cutting-edge radius on flank face temperature is severe in smaller clearance angles. As the clearance angle increases the effect of cutting-edge radius on the maximum temperature at the flank face decreases. This behavior can be explained by the flank contact length between the tool and the workpiece. It can be seen from Figure 34.b that the same behavior exits, i.e. the effect of cutting-edge radius on the contact length is higher for lower clearance angles.

Figure 35 shows the simulation results for different cases, where the cutting-edge radius is changing between $20\mu m$ and $110\mu m$. The figure shows that not only the temperature at the flank face is changing, but also the temperature distribution inside the tool is highly affected by the variation of cutting-edge radius. For tools with smaller cutting-edge radius, the location of maximum flank face temperature is very close to the tool tip. By increasing the cutting-edge radius, the maximum temperature at the flank face increases and its location moves along the flank face.

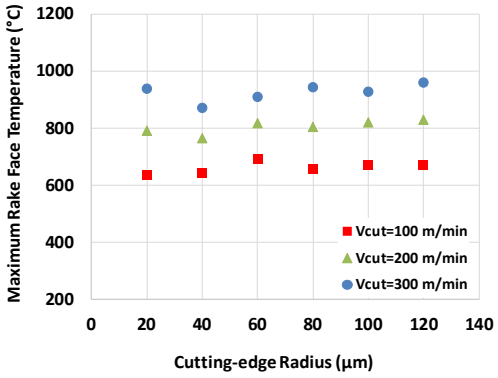

(a)

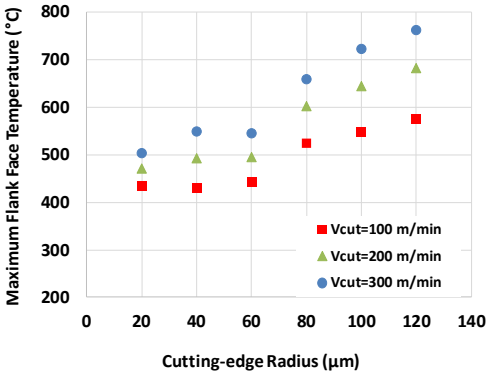

(b)

Figure 32. Effect of cutting-edge radius on maximum temperature at the (a) rake, and (b) flank faces for $\alpha = 3°, \lambda = 11°,\ f = 0.15\ mm/rev$, uncoated carbide tool with AISI1050 steel

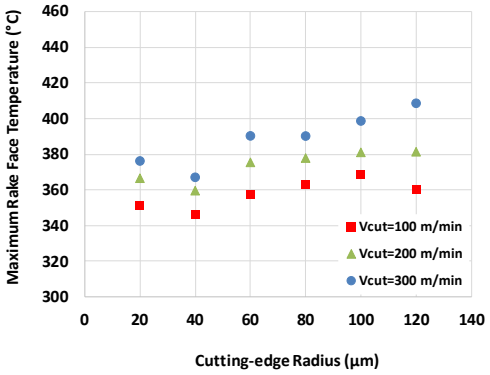

(a)

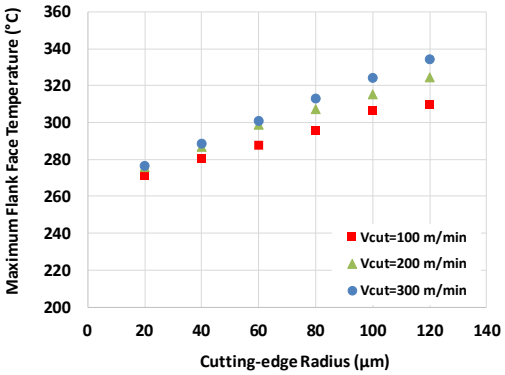

(b)

Figure 33. Effect of cutting-edge radius on maximum temperature at the (a) rake, and (b) flank faces for $\alpha = 3°, \lambda = 11°,\ f = 0.15\ mm/rev$, uncoated carbide tool with Al7075

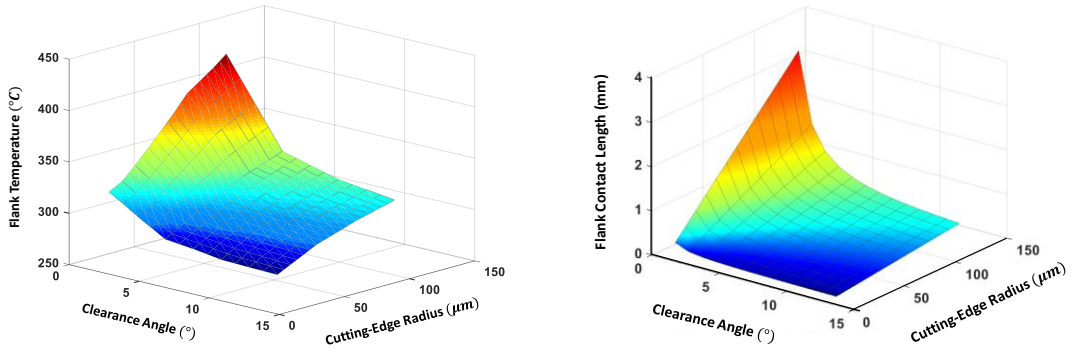

(a) (b)

Figure 34. Variation of (a) maximum temperature at the flank face, and (b) flank contact length with respect to clearance angle and cutting-edge radius, for $\alpha = 3°, f = 0.15\ mm/rev$, uncoated carbide tool with Al7075

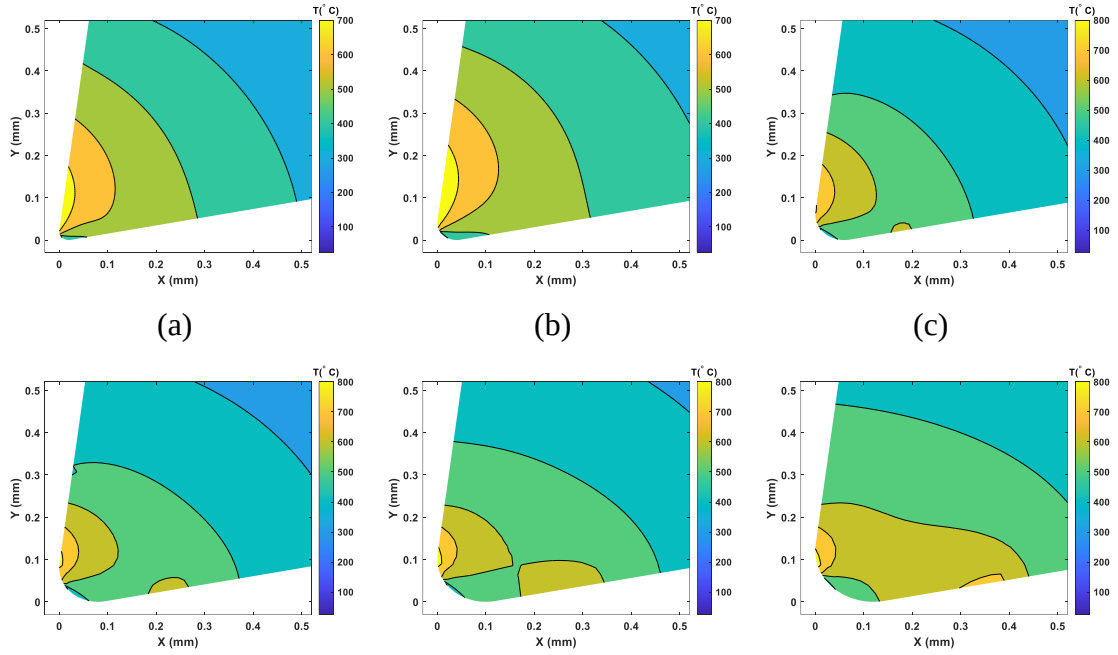

(a) (b) (c)

(d) (e) (f)

Figure 35. Effect of cutting-edge radius on temperature distribution in the tool for $\alpha = 7°, \lambda = 11°,\ f = 0.1\ mm/rev$, uncoated carbide tool with AISI1050, (a) $r = 20\mu m$, (b) $r = 40\mu m$, (c) $r = 60\mu m$, (d) $r = 80\mu m$, (e) $r = 100\mu m$, (f) $r = 120\mu m$

4.1.7. Effect of Stagnation Angle

The stagnation point is located at the tool tip where the second and third deformation zones are separated. The material above this point moves upward and contributes to the chip formation. Whereas, the material below stagnation point goes under a ploughing-recovery process due to the existence of cutting-edge radius. The stagnation angle is illustrated in Figure 3. It should be noted here again that, in this study, stagnation angle is determined by experiments by using the method proposed in [86]. Figure 36 shows the effect of stagnation angle on the maximum flank temperature. For larger stagnation angles, the contact length on the flank face increases which will result in the increase of maximum flank temperature. By increasing the stagnation angle for 40°, the maximum flank temperature increases about 40%. The variation of temperature with the increase of stagnation angle is higher for larger cutting-edge radii. By increasing the stagnation angle from 30° to 70°, the maximum flank temperature increases 30% and 50% for cutting-edge radii $r = 20\mu m$ and $r = 110\mu m$, respectively. Therefore, it can be deduced that determination of stagnation angle is critical in terms of temperature prediction at the third deformation zone.

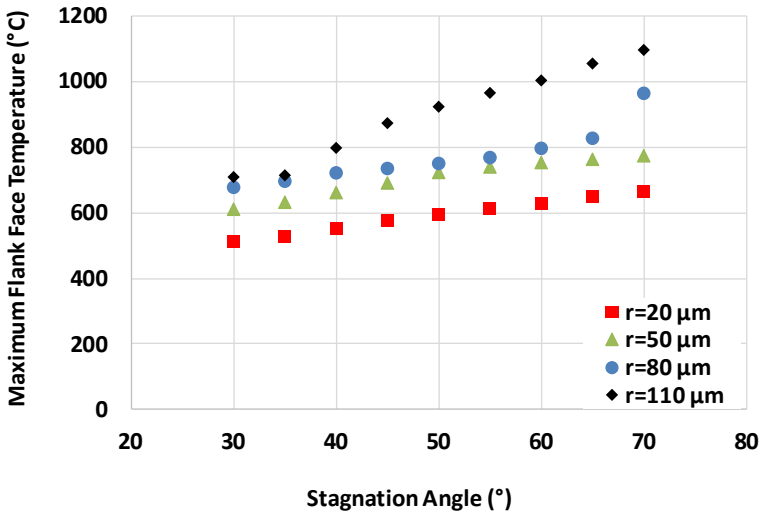

Figure 36. Effect of stagnation angle on maximum temperature at the flank face for $\alpha = 3°, \lambda = 3°,\ f = 0.2\ mm/rev, V_c = 300\ m/min$, uncoated carbide tool with AISI1050

4.1.8. Effect of Tool Wear

Using the verified model the temperature variation with the increase of flank wear for different cutting speeds was predicted. The results are shown in Figure 37.

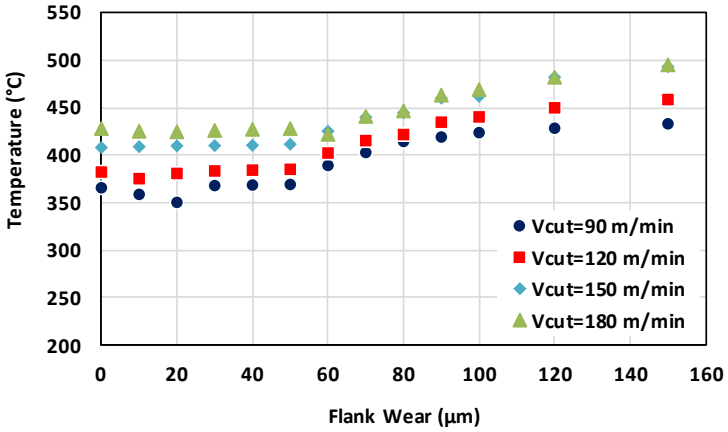

Figure 37. Variation of flank temperature with the increase of flank wear for different cutting speeds, $r = 70\ \mu m$, $f = 0.2\ mm/rev$, $\lambda = 7°$, $\alpha = 5°$.

4.2. Oblique Cutting

4.2.1. Simulation Results

As it was discussed in the previous sections, cutting temperature is an important issue in metal cutting. Developing a model that can predict the temperature and its trend with the change of cutting conditions and tool geometry is of great importance. In this section a sample simulation using the verified model is presented. Figure 27 shows the model prediction for the conditions that are summarized in Table 23. As it is shown in the Figure 27, temperature on the flank face has an increasing-decreasing behavior. In most of the previous studies the effect of third deformation zone is neglected. As a result, the temperature of flank face has its maximum value at the tool tip, and it has a decreasing trend along the flank face. Therefore, the proposed model provides a more realistic prediction of flank face temperature and the location of its maximum value.

Table 24. Parameters used for the sample simulation.

Workpiece-Tool		AISI1050-WC
Cutting speed (m/min)	V_c	300
Feed rate (mm/rev)	f	0.1
Depth of cut (mm)	a_p	0.5
Rake angle (°)	α	5
Clearance angle (°)	λ	7
Inclination angle (°)	i	5
Stagnation angle (°)	θ	55
Cutting-edge radius (μm)	r	50
Density of workpiece $(\frac{kg}{m^3})$	ρ	7800
Melting temperature of workpiece $(°C)$	T_m	1460
Heat capacity of workpiece $(J/kg * K)$	c	500
Thermal conductivity of workpiece $(W/(m^2K))$	k	54
Room temperature $(°C)$	T_∞	25
Reference temperature $(°C)$	T_r	25
Fraction of the work converted into heat	χ	0.9
Sliding friction coefficient	μ_{sl}	0.51
Pressure distribution exponent on rake face	ζ	3
Heat convection coefficient for Air $(W/(m^2K))$	h	20

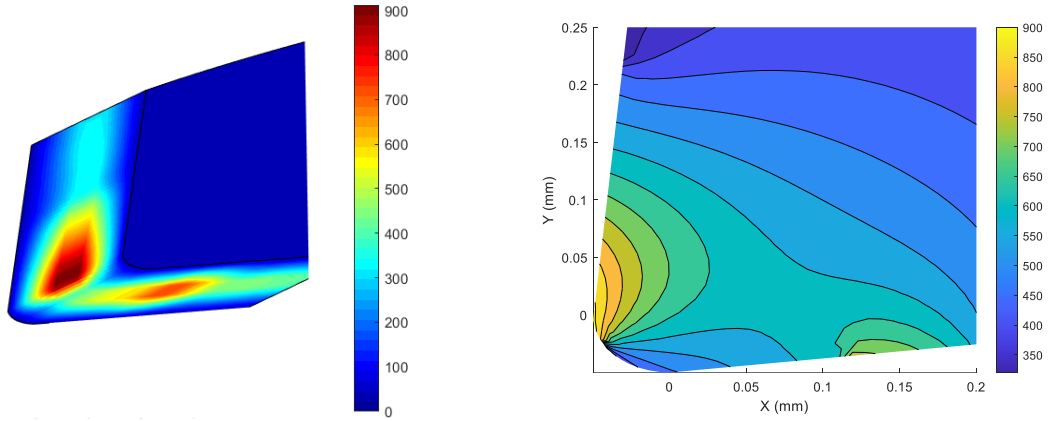

(a) (b)

Figure 38. Tool temperature calculated with the proposed model. (a) 3D model, (b) 2D temperature distribution for a cross-section.

4.2.2. Effect of Inclination Angle

This section investigates the effect of inclination angle on the maximum rake and flank temperature. Figure 39 and Figure 40 shows the variation of maximum rake and flank temperature for different cutting speeds and inclination angles for $\alpha = 7°, \lambda = 7°,\ f = 0.1\ mm/rev,\ r = 90\ \mu m$. According to these results, the cutting temperature for AISI1050 and Al7075 is not affected significantly by the inclination angle.

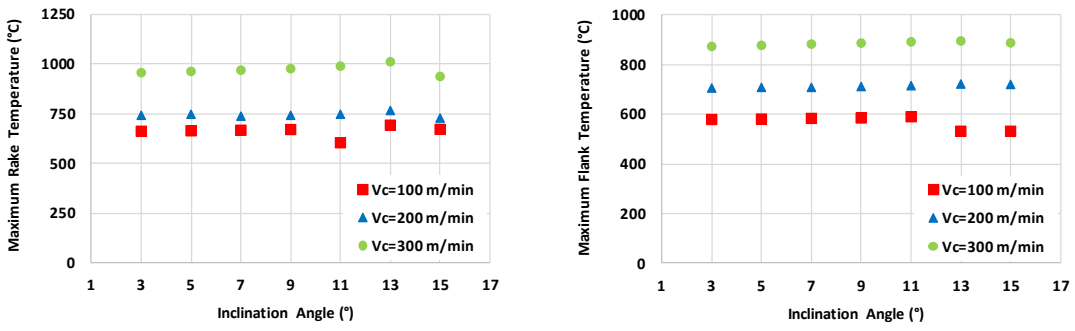

(a) (b)

Figure 39. Effect of inclination angle on maximum temperature at the (a) rake, and (b) flank faces for $\alpha = 7°, \lambda = 7°,\ f = 0.1\ mm/rev, r = 90\ \mu m$, uncoated carbide tool with AISI1050

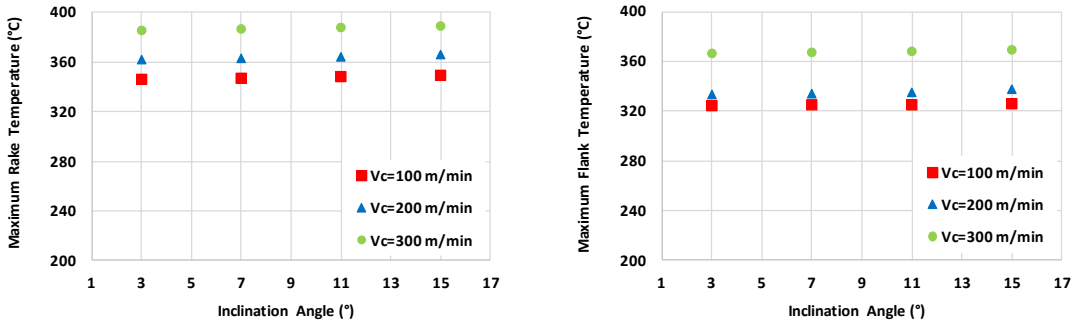

(a) (b)

Figure 40. Effect of inclination angle on maximum temperature at the (a) rake, and (b) flank faces for $\alpha = 7°, \lambda = 7°,\ f = 0.1\ mm/rev, r = 90\ \mu m$, uncoated carbide tool with Al7075

4.2.3. Effect of Cutting Edge Radius

It is important to study the effect of cutting-edge radius on the cutting temperature, since its existence results in the third deformation zone. The result of model prediction for the maximum rake and flank temperature when using different cutting-edge radii is shown in Figure 41 and Figure 42 for AISI1050 steel and Al7075, respectively. According to these figures, the maximum flank temperature increases with the increase of cutting-edge radius. This can be related to the increase of total contact length in the third deformation zone (l_{c3}) by the increase of cutting-edge radius, which is also addressed by equation (21).

Considering the results shown in Figure 41, using tools with 4 times larger cutting-edge radius can increase the flank temperature for 38%. A similar trend is shown in Figure 42 for Al7075. Increasing the cutting edge radius from $30\mu m$ to $130\mu m$, the maximum flank temperature is increased almost 18%. The difference between temperature rise in steel and aluminum can be related to the thermal properties of these two materials. Based on these results and considering the effect of different workpiece materials, it can be concluded that the correct selection of cutting-edge radius is of great importance in cutting processes.

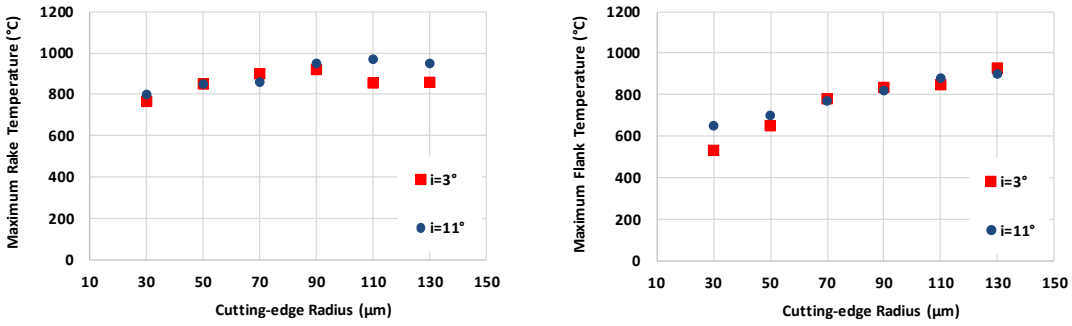

(a) (b)

Figure 41. Effect of cutting-edge radius on maximum temperature at the (a) rake, and (b) flank faces for $\alpha = 7°, \lambda = 11°,\ f = 0.1\ mm/rev, V_c = 300\ m/min$, uncoated carbide tool with AISI1050

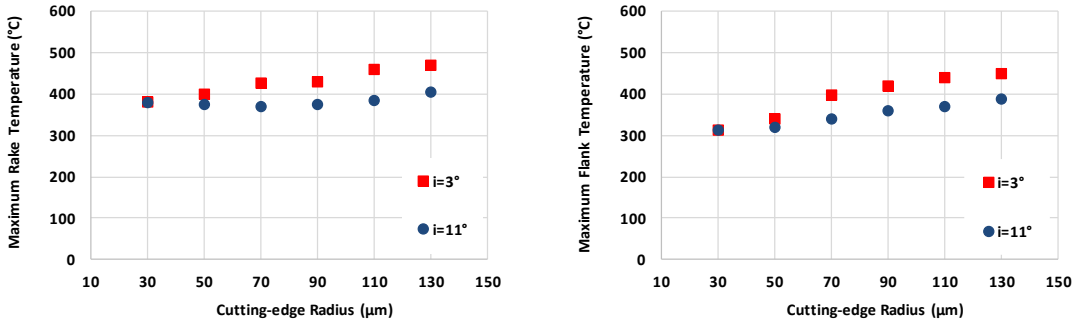

(a) (b)

Figure 42. Effect of cutting-edge radius on maximum temperature at the (a) rake, and (b) flank faces for $\alpha = 7°, \lambda = 11°,\ f = 0.1\ mm/rev,\ V_c = 300\ m/min$, uncoated carbide tool with Al7075

4.2.4. Effect of Clearance Angle

The effect of clearance angle on the maximum flank face temperature using the proposed model is presented in this section. For this purpose, the temperature of flank face was calculated for AISI1050 and Al7075 for $\alpha = 7°, i = 11°,\ f = 0.1\ mm/rev$, and $r = 90\ \mu m$ which are shown in Figure 43. As can be seen from Figure 43, increase of clearance angle from 3° to 11°, results in the decrease of maximum flank temperature by 18% (from 1005 to 820) and 5% (from 390°C to 367°C) for AISI1050 and Al7075,

respectively. This is due to the fact that the contact length on the flank face has an inverse relation with clearance angle which can be described by equation (22). According to this equation with the increase of clearance angle the total contact length on flank face will decrease and this will result in decrease of maximum flank temperature. It may be concluded that using tools with larger clearance angles will help to reduce the cutting temperatures. However, increase of clearance angle will make the tool weaker and increases the possibility of tool breakage. Therefore, an optimum value of clearance angle should be selected to reduce the temperature without affecting the tool strength significantly. In addition, the results for steel and aluminum shows that the cutting temperature in steel is higher and more affected by the clearance angle. Therefore, proper selection of clearance angle for machining of workpiece materials with lower heat conductivity is of high importance in terms of cutting temperature optimization.

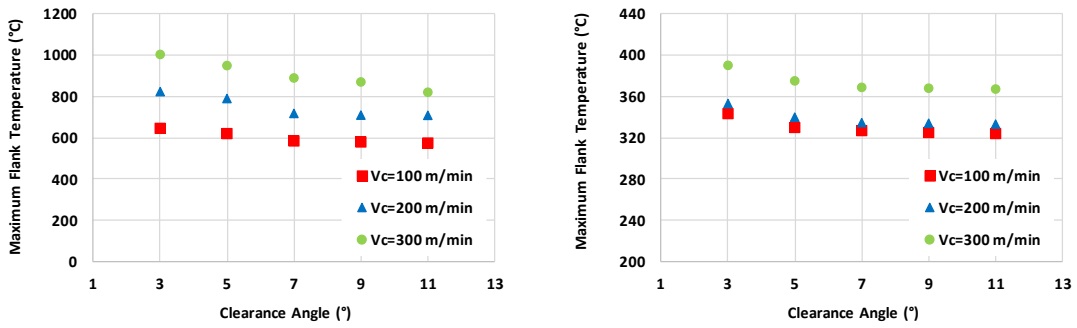

(a) (b)

Figure 43. Effect of clearance angle on maximum temperature at the flank faces for (a) AISI1050, and (b) Al7075, $\alpha = 7°, i = 11°, f = 0.1\ mm/rev, r = 90\ \mu m$, uncoated carbide tool

4.3. Turning Process

4.3.1. Simulation Results

In this section a sample simulation using the verified model is presented. Figure 44 shows the model prediction for the conditions that are summarized in Table 25. The solution time for such a simulation is almost 15 minutes.

Table 25. Parameters used for the sample simulation.

Workpiece-Tool		AISI1050-WC
Cutting speed (m/min)	V_c	200
Feed rate (mm/rev)	f	0.1
Depth of cut (mm)	a_p	1.5
Nose radius (mm)	r_n	1.2
Rake angle (°)	α	5
Clearance angle (°)	λ	7
Approach angle (°)	κ	0
Inclination angle (°)	i	7
Stagnation angle (°)	θ	55
Cutting-edge radius (μm)	r	30
Density of workpiece $(\frac{kg}{m^3})$	ρ	7800
Melting temperature of workpiece $(°C)$	T_m	1460
Heat capacity of workpiece $(J/kg * K)$	c	500
Thermal conductivity of workpiece $(W/(m^2K))$	k	54
Room temperature $(°C)$	T_∞	25
Reference temperature $(°C)$	T_r	25
Fraction of the work converted into heat	χ	0.9
Sliding friction coefficient	μ_{sl}	0.51
Pressure distribution exponent on rake face	ζ	3
Heat convection coefficient for Air $(W/(m^2K))$	h	20

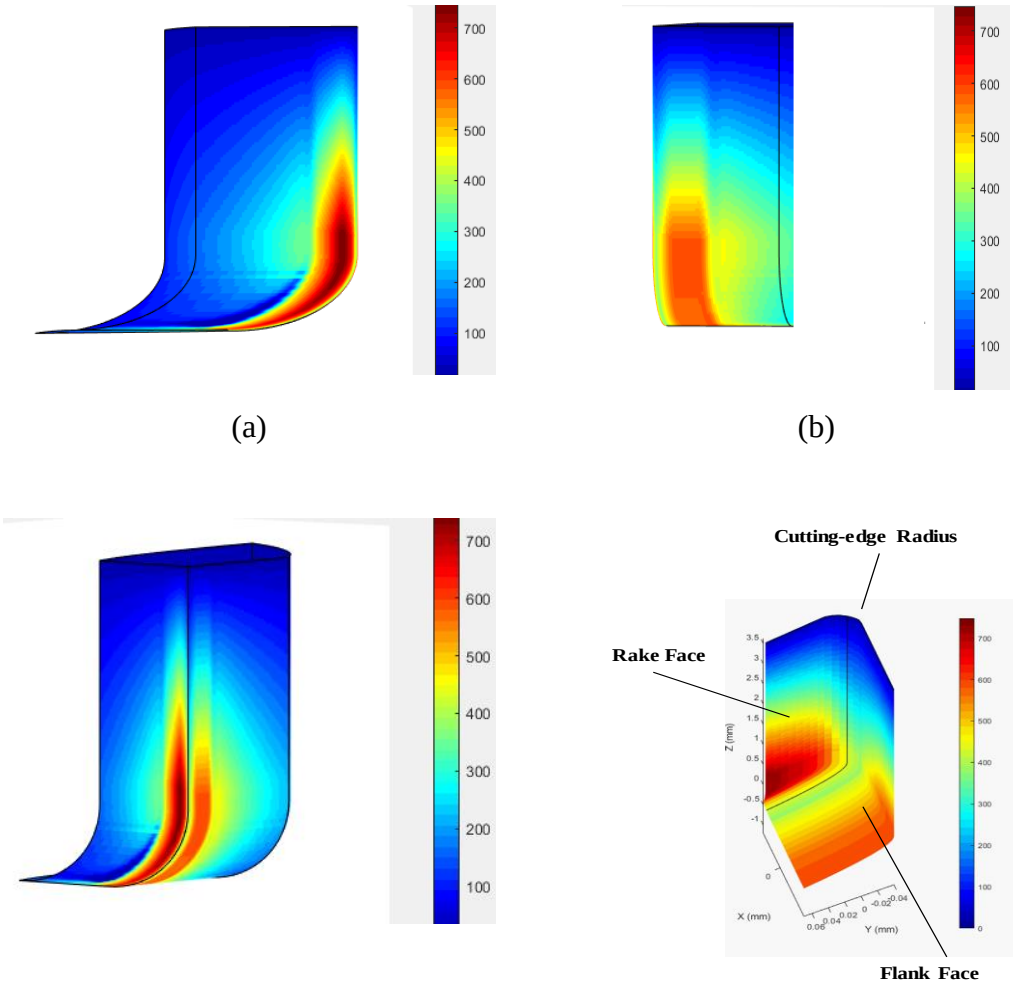

Figure 44. Tool temperature calculated with the proposed model. (a) Rake face, (b) Flank face, (c) 3D simulation result, (d) Simulation result near the cutting area

4.3.2. Effect of Nose Radius

The simulation results for the maximum rake and flank faces temperature while cutting AISI 1050 with uncoated carbide tool having difference nose radii (for $r_n = 0.2\,mm$ to $r_n = 1.4\,mm$) are shown in Figure 45. According to these results, the maximum temperature at the rake and flank faces are decreased with the increase of nose radius. Increasing the nose radius from $0.2\,mm$ to $1.4\,mm$, the maximum rake and flank face temperatures decrease for 14% and 13% , rexpectively. The increase in temperature as the tool nose radius decreases can be explained by the decrease in the area contribute to the heat conduction at the tool tip, causing the temperature to increase locally. Also, as the tool nose radius increases, there is a longer cutting edge for the same amount of chip

to be removed. This results in a reduction in the local contact surface, thus decreasing the temperatures.

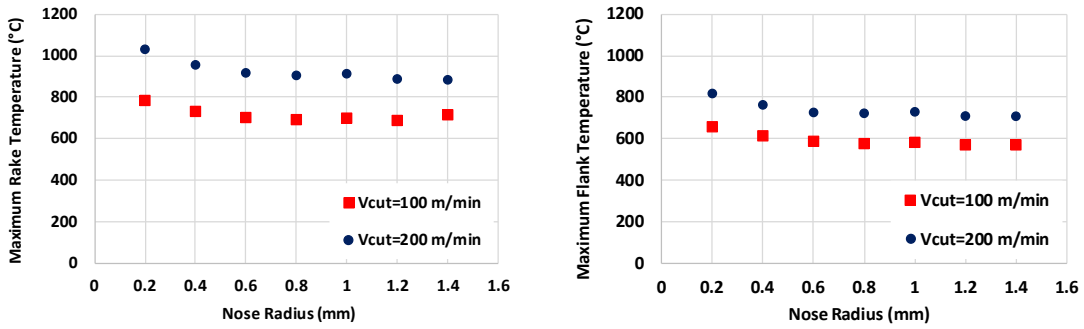

(a) (b)

Figure 45. Effect of cutting-edge radius on maximum temperature at the (a) rake, and (b) flank faces for $\alpha = 5°, \lambda = 7°,\ f = 0.1\ mm/rev, i = 11°, r = 50\mu m$, uncoated carbide tool with AISI1050

4.3.3. Effect of Cutting-edge Radius

Investigating the effect of the cutting-edge radius on cutting temperature is of high importance. Figure 46 illustrate the model predictions for maximum rake and flank temperature for different cutting-edge radii when cutting AISI1050 with uncoated carbide tool. According to this figure, as the cutting-edge radius increases, the maximum flank temperature rises. Similar to the orthogonal and oblique cutting, this can be explained by the fact that increasing the cutting-edge radius increases total contact length in the third deformation zone.

According to the data presented in Figure 46, using tools with a 3 times smaller cutting-edge radius can decrease the flank temperature by 26%. However, based on simulation results, the temperature on the rake face is not affected significantly by the cutting-edge radius.

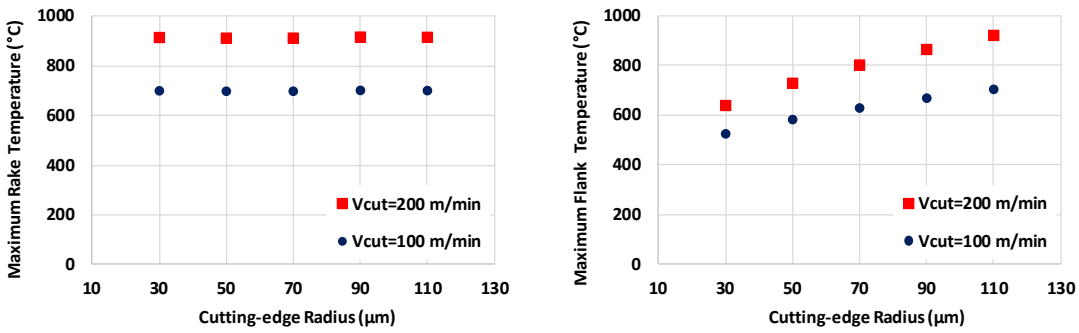

(a) (b)

Figure 46. Effect of cutting-edge radius on maximum temperature at the (a) rake, and (b) flank faces for $\alpha = 5°, \lambda = 7°,\ f = 0.1\ mm/rev$, $i = 11°$, $r_n = 1\ mm$, uncoated carbide tool with AISI1050

5. SUGGESTIONS FOR FUTURE WORKS

- This study considered a dry orthogonal cutting operation. However, the effect of coolants such as different cutting fluids, cryogenic coolants, and high-pressure coolants on the cutting temperature can be included in the model.
- The developed model considers the steady-state condition. However, using the analytical solutions for the transient conditions, it can be applied to different cutting operations such as broaching, drilling and milling processes.
- The surface integrity of a machined workpiece, which becomes more critical in the reliable production of sensitive components, is strongly related to the heat generation at the third deformation zone. High temperatures during the cutting process, especially flank temperature, can result in deformation of subsurface grain, subsurface microstructure alteration and residual stress. The model developed in this study can also be used to analyze surface integrity related problems in machining operations.
- The thermal properties of the tool and workpiece are considered constant and independent from the temperature. However, it is well-known that these properties are affected by the material temperature. Therefore, in the future studies, defining a temperature-dependent thermal properties may increase the accuracy of the model.
- Nowadays, coatings are widely used on cutting tools in the metal cutting industry. The reason is their superior wear resistance and thermal barrier effect. Tool coatings prevent direct contact between the workpiece and the tool substrate which can affect the cutting temperature and machining performance in comparison to uncoated tools. The proposed model in this study, can also be enhanced to evaluate the effect of different coatings on the cutting temperature.

6. CONCLUSION

In this study, a thermomechanical dual-zone analytical model was developed for the prediction of temperature distribution in the cutting tool, considering the effect of cutting-edge radius and the third deformation zone. The dual-zone model was used for heat flux calculations along the rake and flank faces where Johnson-Cook constitutive model represented the material behavior. The temperature was determined analytically at the tool-chip and tool-workpiece boundaries, and the temperature distribution inside the tool was calculated using the Finite Difference Method. The convection boundary condition was applied to the free surfaces of the tool, and room temperature was applied to the surfaces far from the cutting area. Experiments were performed to verify the model predictions, and a good agreement was observed between the model predictions and the test results.

The following is the summary of the outputs:

- For the first time in the literature a 3D model is developed which considers the effect of primary, second, and third deformation zones, complex friction condition on the tool-chip and tool-workpiece interfaces, cutting-edge radius and convection boundary condition. Moreover, the model is capable of predicting the temperature in a worn tool in orthogonal cutting, oblique cutting and turning operation. Therefore, a comprehensive model is developed and having the tool geometry and cutting parameters as the inputs, the temperature distribution at any point in the cutting tool can be calculated. In addition, the model is considerably faster than numerical methods, which can calculate the temperature distribution within a range of minutes.
- A 2D model was developed for the prediction of temperature in the cutting tool in orthogonal cutting condition, whereas for the oblique cutting and turning process a 3D model was proposed. The temperature distribution inside the tool was calculated using the Finite Difference Method. Therefore, the temperature at any point of the tool can be predicted using this model.
- The proposed model for turning process divides the uncut chip thickness into various elements. Some parameters like contact length and shear stress are calculated

separately for each element. However, some other parameters such as chip flow angle and chip velocity are assumed to be global.

- Including the third deformation zone in the temperature model of a tool can increase the accuracy of temperature calculation on rake and flank faces, which will result in more realistic simulations. Moreover, this helps to predict the maximum temperature and its location on the flank face, the temperature along the rake face, and temperature distribution inside the cutting tool and workpiece in a more accurate manner.
- The model predictions were verified by conducting an experimental study. Different sets of experiments were performed and compared to the model results for orthogonal cutting, oblique cutting, and turning process with new and worn tools.
- For the orthogonal cutting experiments, thermal camera and K-type thermocouples were used to measure the temperature in the tool. In addition, the workpiece temperature was measured with the use of K-type thermocouples attached to it. Due to the rotation of workpiece in turning operation, temperature measurement becomes challenging. A miniature standalone data acquisition system (DAS) was used which is also rotating with the workpiece. The DAS was mounted on the spindle with a special fixture and the data was recorded in this data acquisition card during the tests. The card is removed and attached to computer to gather the data after the test is finished.
- Due to the difficulty of measuring the temperature with the thermal camera in oblique cutting and turning process, measurements were done only with the embedded thermocouples in the cutting tool.
- According to the simulation results, eliminating the third deformation zone affects the temperature prediction on the flank face significantly. Not only the maximum flank temperature, but also its location on the tool changes.
- Increasing the cutting-edge radius six times while cutting Al7075 led to the increase of maximum temperature at the flank face around 15%, whereas 50% increase for AISI 1050 steel was observed.
- Based on the simulation results, the effect of cutting-edge radius on flank face temperature is more significant for smaller clearance angles. Variation of the cutting-edge radius by $90\mu m$, increases the flank face temperature by 35% and 20% for 1° and 13° clearance angles, respectively, while cutting aluminum with a carbide tool.

- By increasing the clearance angle, the maximum temperature on the flank face drops significantly. This effect is more distinct for smaller clearance angles, and by increasing the clearance angle the variation becomes slighter.
- The effect of clearance angle variation on the flank temperature is more noticeable for steel than for aluminum. For $V_c = 300\ m/min$ when changing the clearance angle between 1° and 11°, the flank face temperature was decreased 45% in steel, whereas a 20% reduction was observed for aluminum, in orthogonal cutting condition.
- The tool wear is an important issue in the machining process which can affect the produced part quality. Therefore, having a comprehensive model that can predict the temperature rise with the increase of flank wear is a necessity. The present study, includes the effect of flank wear on the cutting temperature. Based on the model predictions increasing the tool wear from 0 to $120\mu m$ the flank temperature increases for 18% when cutting Al7075.
- The effect of nose radius on the cutting temperature on rake and flank faces were investigated using the proposed model. It was observed that the temperature on both rake and flank faces decrease with the increase of nose radius. Increasing the nose radius from $0.2mm$ to $1.4mm$ the maximum temparure decreased almost 15% for rake and flank faces. The reason can be the decrease of contact area by the decrease of nose radius.

REFERENCES

[1] F. W. Taylor, *On the art of cutting metals*. American society of mechanical engineers, 1906.

[2] N. Abukhshim, P. Mativenga, and M. Sheikh, "Heat generation and temperature prediction in metal cutting: A review and implications for high speed machining," *International Journal of Machine Tools and Manufacture,* vol. 46, no. 7, pp. 782-800, 2006.

[3] Y. Altintas and A. Ber, "Manufacturing automation: metal cutting mechanics, machine tool vibrations, and CNC design," *Appl. Mech. Rev.,* vol. 54, no. 5, pp. B84-B84, 2001.

[4] J. K. Rai and P. Xirouchakis, "FEM-based prediction of workpiece transient temperature distribution and deformations during milling," *The International Journal of Advanced Manufacturing Technology,* vol. 42, no. 5-6, p. 429, 2009.

[5] M. E. Merchant, "Mechanics of the metal cutting process. I. Orthogonal cutting and a type 2 chip," *Journal of applied physics,* vol. 16, no. 5, pp. 267-275, 1945.

[6] A. O. Schmidt, "A Thermal-Balance Method and Mechancal Investigation Machinability," *Trans. ASME,* vol. 67, 1945.

[7] G. Barrow, "Review of experimental and theoretical techniques for assessing cutting temperatures," *CIRP, l 973, 22,(2), 203-2 ll,* 1974.

[8] E. M. Trent and P. K. Wright, *Metal cutting*. Butterworth-Heinemann, 2000.

[9] H. Blok, "Theoretical study of temperature rise at surfaces of actual contact under oiliness lubricating conditions," *Proc. Instn. Mech. Engrs.(General discussion on lubrication and lubricants),* vol. 2, p. 222, 1937.

[10] K. Trigger and B. Chao, "An analytical evaluation of metal-cutting temperatures," 1950: ASME.

[11] E. Loewen, "On the analysis of cutting-tool temperatures," *Trans. ASME,* vol. 76, p. 217, 1954.

[12] J. Weiner, "Shear-plane temperature distribution in orthogonal cutting," *Trans. ASME,* vol. 77, no. 8, pp. 1331-1338, 1955.

[13] G. Boothroyd, *Fundamentals of metal machining and machine tools*. Crc Press, 1988.

[14] P. Wright, S. McCormick, and T. Miller, "Effect of rake face design on cutting tool temperature distributions," 1980.

[15] P. Venuvinod and W. Lau, "Estimation of rake temperatures in free oblique cutting," *International Journal of Machine Tool Design and Research,* vol. 26, no. 1, pp. 1-14, 1986.

[16] E. M. Berliner and V. Krainov, "Analytic calculations of the temperature field and heat flows on the tool surface in metal cutting due to sliding friction," *Wear,* vol. 143, no. 2, pp. 379-395, 1991.

[17] H. T. Young and T. L. Chou, "Modelling of tool/chip interface temperature distribution in metal cutting," *International journal of mechanical sciences,* vol. 36, no. 10, pp. 931-943, 1994.

[18] R. Radulescu and S. Kapoor, "An analytical model for prediction of tool temperature fields during continuous and interrupted cutting," 1994.

[19] D. McFeron and B. Chao, "Transient interface temperatures in plain peripheral

milling," 1956: ASME.
[20] D. Stephenson, T.-C. Jen, and A. Lavine, "Cutting tool temperatures in contour turning: transient analysis and experimental verification," 1997.
[21] A. Moufki, A. Molinari, and D. Dudzinski, "Modelling of orthogonal cutting with a temperature dependent friction law," *Journal of the Mechanics and Physics of Solids,* vol. 46, no. 10, pp. 2103-2138, 1998.
[22] E. Levy, C. Tsai, and M. Groover, "Analytical investigation of the effect of tool wear on the temperature variations in a metal cutting tool," 1976.
[23] R. S. Hahn, "On the temperature developed at the shear plane in the metalcutting process," in *Journal of Applied Mechanics-Transactions of the ASME*, 1951, vol. 18, no. 3, pp. 323-323: ASME-AMER SOC MECHANICAL ENG 345 E 47TH ST, NEW YORK, NY 10017.
[24] B. Chao, "Temperature distribution at the tool-chip interface in metal cutting," *Trans. ASME*, vol. 77, p. 1107, 1955.
[25] J. C. JAEGER, "Moving sources of heat and the temperature of sliding contacts," in *Proceedings of the royal society of New South Wales*, 1942, vol. 76, pp. 203-224.
[26] R. Komanduri and Z. B. Hou, "Thermal modeling of the metal cutting process: part I—temperature rise distribution due to shear plane heat source," *International Journal of Mechanical Sciences,* vol. 42, no. 9, pp. 1715-1752, 2000.
[27] R. Komanduri and Z. B. Hou, "Thermal modeling of the metal cutting process—Part III: temperature rise distribution due to the combined effects of shear plane heat source and the tool–chip interface frictional heat source," *International Journal of Mechanical Sciences,* vol. 43, no. 1, pp. 89-107, 2001.
[28] Y. Karpat and T. Özel, "Predictive analytical and thermal modeling of orthogonal cutting process—part I: predictions of tool forces, stresses, and temperature distributions," *Journal of manufacturing science and engineering,* vol. 128, no. 2, pp. 435-444, 2006.
[29] P. Oxley and H. Young, "The Mechanics of Machining: An Analytical Approach to Assessing Machinability," *Ellis Horwood Publisher*, pp. 136-182, 1989.
[30] R. Komanduri and Z. B. Hou, "Thermal modeling of the metal cutting process—Part II: temperature rise distribution due to frictional heat source at the tool–chip interface," *International Journal of Mechanical Sciences,* vol. 43, no. 1, pp. 57-88, 2001.
[31] I. Lazoglu and C. Islam, "Modeling of 3D temperature fields for oblique machining," *CIRP Annals,* vol. 61, no. 1, pp. 127-130, 2012/01/01/ 2012.
[32] A. Rapier, "A theoretical investigation of the temperature distribution in the metal cutting process," *British Journal of Applied Physics,* vol. 5, no. 11, p. 400, 1954.
[33] D. Ulutan, I. Lazoglu, and C. Dinc, "Three-dimensional temperature predictions in machining processes using finite difference method," *Journal of Materials Processing Technology,* vol. 209, no. 2, pp. 1111-1121, 2009/01/19/ 2009.
[34] M. Stevenson, P. Wright, and J. Chow, "Further developments in applying the finite element method to the calculation of temperature distributions in machining and comparisons with experiment," *Journal of Engineering for Industry*, vol. 105, no. 3, pp. 149-154, 1983.
[35] T. El-Wardany, E. Mohammed, and M. Elbestawi, "Cutting temperature of ceramic tools in high speed machining of difficult-to-cut materials," *International Journal of Machine Tools and Manufacture,* vol. 36, no. 5, pp. 611-634, 1996.
[36] V. Ostafiev, A. Kharkevich, K. Weinert, and S. Ostafiev, "Tool heat transfer in

orthogonal metal cutting," 1999.
[37] W. Grzesik, M. Bartoszuk, and P. Nieslony, "Finite difference analysis of the thermal behaviour of coated tools in orthogonal cutting of steels," *International Journal of Machine Tools and Manufacture*, vol. 44, no. 14, pp. 1451-1462, 2004.
[38] S. Mane, S. S. Joshi, S. Karagadde, and S. G. Kapoor, "Modeling of variable friction and heat partition ratio at the chip-tool interface during orthogonal cutting of Ti-6Al-4V," *Journal of Manufacturing Processes*, vol. 55, pp. 254-267, 2020/07/01/ 2020.
[39] Y. Huang and S. Liang, "Modelling of the cutting temperature distribution under the tool flank wear effect," *Proceedings of the Institution of Mechanical Engineers, Part C: Journal of Mechanical Engineering Science*, vol. 217, no. 11, pp. 1195-1208, 2003.
[40] K.-M. Li and S. Y. Liang, "Modeling of cutting temperature in near dry machining," 2006.
[41] R. Dutt and R. Brewer, "On the theoretical determination of the temperature field in orthogonal machining," *International Journal of Production Research*, vol. 4, no. 2, pp. 91-114, 1965.
[42] A. Smith and E. Armarego, "Temperature prediction in orthogonal cutting with a finite difference approach," *CIRP Annals*, vol. 30, no. 1, pp. 9-13, 1981.
[43] I. Lazoglu and Y. Altintas, "Prediction of tool and chip temperature in continuous and interrupted machining," *International Journal of Machine Tools and Manufacture*, vol. 42, no. 9, pp. 1011-1022, 2002.
[44] A. Tay, M. Stevenson, and G. de Vahl Davis, "Using the finite element method to determine temperature distributions in orthogonal machining," *Proceedings of the institution of mechanical engineers*, vol. 188, no. 1, pp. 627-638, 1974.
[45] M. Stevenson and P. Oxley, "An experimental investigation of the influence of strain-rate and temperature on the flow stress properties of a low carbon steel using a machining test," *Proceedings of the Institution of Mechanical Engineers*, vol. 185, no. 1, pp. 741-754, 1970.
[46] A. Tay, M. Stevenson, G. de Vahl Davis, and P. Oxley, "A numerical method for calculating temperature distributions in machining, from force and shear angle measurements," *International Journal of Machine Tool Design and Research*, vol. 16, no. 4, pp. 335-349, 1976.
[47] P. Muraka, G. Barrow, and S. Hinduja, "Influence of the process variables on the temperature distribution in orthogonal machining using the finite element method," *International Journal of Mechanical Sciences*, vol. 21, no. 8, pp. 445-456, 1979.
[48] E. Usui, T. Shirakashi, and T. Kitagawa, "Analytical prediction of three dimensional cutting process—Part 3: Cutting temperature and crater wear of carbide tool," 1978.
[49] J. Tlusty and E. Orady, "Effect of thermal cycling on tool wear in milling," in *9th NAMRC Conf., Penn. State University*, 1981.
[50] B. Shi and H. Attia, "Modeling the thermal and tribological processes at the tool-chip interface in machining," *Machining science and technology*, vol. 13, no. 2, pp. 210-226, 2009.
[51] M. Attia and L. Kops, "A new approach to cutting temperature prediction considering the thermal constriction phenomenon in multi-layer coated tools," *CIRP Annals*, vol. 53, no. 1, pp. 47-52, 2004.
[52] Y. Avevor, A. Moufki, and M. Nouari, "Analysis of the frictional heat partition in

sticking-sliding contact for dry machining: an Analytical-Numerical modelling," *Procedia CIRP*, vol. 58, pp. 539-542, 2017.
[53] C. Islam, I. Lazoglu, and Y. Altintas, "A three-dimensional transient thermal model for machining," *Journal of Manufacturing Science and Engineering*, vol. 138, no. 2, p. 021003, 2016.
[54] C. Shan, X. Zhang, B. Shen, and D. Zhang, "An improved analytical model of cutting temperature in orthogonal cutting of Ti6Al4V," *Chinese Journal of Aeronautics*, vol. 32, no. 3, pp. 759-769, 2019/03/01/ 2019.
[55] C. Shan, M. Zhang, S. Zhang, and J. Dang, "Prediction of machining-induced residual stress in orthogonal cutting of Ti6Al4V," *The International Journal of Advanced Manufacturing Technology*, vol. 107, no. 5, pp. 2375-2385, 2020/03/01 2020.
[56] A. Thakare and A. Nordgren, "Experimental study and modeling of steady state temperature distributions in coated cemented carbide tools in turning," *Procedia CIRP*, vol. 31, pp. 234-239, 2015.
[57] V. Kryzhanivskyy, V. Bushlya, O. Gutnichenko, I. Petrusha, and J.-E. Ståhl, "Modelling and experimental investigation of cutting temperature when rough turning hardened tool steel with PCBN tools," *Procedia CIRP*, vol. 31, pp. 489-495, 2015.
[58] M. Putz, G. Schmidt, U. Semmler, C. Oppermann, M. Bräunig, and U. Karagüzel, "Modeling of heat fluxes during machining and their effects on thermal deformation of the cutting tool," *Procedia CIRP*, vol. 46, pp. 611-614, 2016.
[59] D. Umbrello, L. Filice, S. Rizzuti, F. Micari, and L. Settineri, "On the effectiveness of finite element simulation of orthogonal cutting with particular reference to temperature prediction," *Journal of Materials Processing Technology*, vol. 189, no. 1-3, pp. 284-291, 2007.
[60] M. B. da Silva and J. Wallbank, "Cutting temperature: prediction and measurement methods—a review," *Journal of materials processing technology*, vol. 88, no. 1-3, pp. 195-202, 1999.
[61] M. Davies, T. Ueda, R. M'saoubi, B. Mullany, and A. Cooke, "On the measurement of temperature in material removal processes," *CIRP Annals-Manufacturing Technology*, vol. 56, no. 2, pp. 581-604, 2007.
[62] W. Grzesik, "Experimental investigation of the cutting temperature when turning with coated indexable inserts," *International journal of machine tools and manufacture*, vol. 39, no. 3, pp. 355-369, 1999.
[63] I. Korkut, M. Boy, I. Karacan, and U. Seker, "Investigation of chip-back temperature during machining depending on cutting parameters," *Materials & design*, vol. 28, no. 8, pp. 2329-2335, 2007.
[64] F. Klocke, S. Gierlings, M. Brockmann, and D. Veselovac, "Force-based temperature modeling for surface integrity prediction in broaching nickel-based alloys," *Procedia CIRP*, vol. 13, pp. 314-319, 2014.
[65] S. Gierlings and M. Brockmann, "Analytical Model Approach for Tool Temperature Prediction in Broaching Nickel-Based Alloys," in *Advanced Materials Research*, 2014, vol. 1018, pp. 99-106: Trans Tech Publ.
[66] H. Mzad, "A simple mathematical procedure to estimate heat flux in machining using measured surface temperature with infrared laser," *Case Studies in Thermal Engineering*, vol. 6, pp. 128-135, 2015.
[67] D. Soler Mallol, P. J. Arrazola Arriola, P. X. Aristimuño Osoro, M. Saez de Buruaga Echeandia, and A. Garay Araiko, "New Calibration method to measure

Rake Face Temperature of the tool during Dry Orthogonal Cutting using Thermography," 2018.
[68] B. Denkena, M.-A. Dittrich, F. Uhlich, M. Wichmann, and M. Mücke, "Process parallel simulation of workpiece temperatures using sensory workpieces," *CIRP Journal of Manufacturing Science and Technology,* vol. 21, pp. 140-149, 2018.
[69] V. Kryzhanivskyy, V. Bushlya, O. Gutnichenko, R. M'Saoubi, and J. E. Ståhl, "Heat flux in metal cutting: Experiment, model, and comparative analysis," *International Journal of Machine Tools and Manufacture,* vol. 134, pp. 81-97, 2018/11/01/ 2018.
[70] S. Huang, B. Tao, J. Li, Y. Fan, and Z. Yin, "On-line estimation of the tool-chip interface temperature field during turning using a sequential inverse method," *The International Journal of Advanced Manufacturing Technology,* vol. 97, no. 1, pp. 939-952, 2018.
[71] L. Chen, B. L. Tai, R. G. Chaudhari, X. Song, and A. J. Shih, "Machined surface temperature in hard turning," *International Journal of Machine Tools and Manufacture,* vol. 121, pp. 10-21, 2017/10/01/ 2017.
[72] D. Biermann, M. Kirschner, K. Pantke, W. Tillmann, and J. Herper, "New coating systems for temperature monitoring in turning processes," *Surface and Coatings Technology,* vol. 215, pp. 376-380, 2013/01/25/ 2013.
[73] R. M'Saoubi and H. Chandrasekaran, "Investigation of the effects of tool micro-geometry and coating on tool temperature during orthogonal turning of quenched and tempered steel," *International Journal of Machine Tools and Manufacture,* vol. 44, no. 2, pp. 213-224, 2004/02/01/ 2004.
[74] M. Harzallah, T. Pottier, R. Gilblas, Y. Landon, M. Mousseigne, and J. Senatore, "A coupled in-situ measurement of temperature and kinematic fields in Ti-6Al-4V serrated chip formation at micro-scale," *International Journal of Machine Tools and Manufacture,* vol. 130-131, pp. 20-35, 2018/08/01/ 2018.
[75] U. Karaguzel and E. Budak, "Investigating effects of milling conditions on cutting temperatures through analytical and experimental methods," *Journal of Materials Processing Technology,* vol. 262, pp. 532-540, 2018/12/01/ 2018.
[76] H.-C. Möhring, V. Kushner, M. Storchak, and T. Stehle, "Temperature calculation in cutting zones," *CIRP Annals,* vol. 67, no. 1, pp. 61-64, 2018.
[77] U. Heisel, M. Storchak, P. Eberhard, and T. Gaugele, "Experimental studies for verification of thermal effects in cutting," *Production Engineering,* vol. 5, no. 5, pp. 507-515, 2011.
[78] J. Navarro-Devia, C. Amaya, J. Caicedo, and W. Aperador, "Performance evaluation of HSS cutting tool coated with hafnium and vanadium nitride multilayers, by temperature measurement and surface inspection, on machining AISI 1020 steel," *Surface and Coatings Technology,* vol. 332, pp. 484-493, 2017.
[79] J. Saelzer, S. Berger, I. Iovkov, A. Zabel, and D. Biermann, "In-situ measurement of rake face temperatures in orthogonal cutting," *CIRP Annals,* vol. 69, no. 1, pp. 61-64, 2020/01/01/ 2020.
[80] J. Zhao, Z. Liu, B. Wang, J. Hu, and Y. Wan, "Tool coating effects on cutting temperature during metal cutting processes: Comprehensive review and future research directions," *Mechanical Systems and Signal Processing,* vol. 150, p. 107302, 2021/03/01/ 2021.
[81] J. Zhao and Z. Liu, "Influences of coating thickness on cutting temperature for dry hard turning Inconel 718 with PVD TiAlN coated carbide tools in initial tool wear stage," *Journal of Manufacturing Processes,* vol. 56, pp. 1155-1165,

2020/08/01/ 2020.
[82] J. Zhao, Z. Liu, B. Wang, Y. Hua, and Q. Wang, "Cutting temperature measurement using an improved two-color infrared thermometer in turning Inconel 718 with whisker-reinforced ceramic tools," *Ceramics International,* vol. 44, no. 15, pp. 19002-19007, 2018.
[83] G. List, G. Sutter, and A. Bouthiche, "Cutting temperature prediction in high speed machining by numerical modelling of chip formation and its dependence with crater wear," *International Journal of Machine Tools and Manufacture,* vol. 54, pp. 1-9, 2012.
[84] A. Attanasio, E. Ceretti, S. Rizzuti, D. Umbrello, and F. Micari, "3D finite element analysis of tool wear in machining," *CIRP annals,* vol. 57, no. 1, pp. 61-64, 2008.
[85] Y. Karpat and T. Özel, "Predictive analytical and thermal modeling of orthogonal cutting process—part II: effect of tool flank wear on tool forces, stresses, and temperature distributions," *Journal of manufacturing science and engineering,* vol. 128, no. 2, pp. 445-453, 2006.
[86] E. Budak, E. Ozlu, H. Bakioglu, and Z. Barzegar, "Thermo-mechanical modeling of the third deformation zone in machining for prediction of cutting forces," *CIRP Annals-Manufacturing Technology,* vol. 65, no. 1, pp. 121-124, 2016.
[87] E. Ozlu, E. Budak, and A. Molinari, "Analytical and experimental investigation of rake contact and friction behavior in metal cutting," *International Journal of Machine Tools and Manufacture,* vol. 49, no. 11, pp. 865-875, 2009.
[88] Y. Altintas and M. Weck, "Chatter stability of metal cutting and grinding," *CIRP Annals-Manufacturing Technology,* vol. 53, no. 2, pp. 619-642, 2004.
[89] E. Budak and Y. Altintas, "Prediction of milling force coefficients from orthogonal cutting data," *ASME PROD ENG DIV PUBL PED, ASME, NEW YORK, NY,(USA), 1993,* vol. 64, pp. 453-460, 1993.
[90] A. Molinari and D. Dudzinski, "Stationary shear band in high-speed machining," *CR Acad. Sci. Paris,* vol. 315, no. II, pp. 399-405, 1992.
[91] D. Dudzinski and A. Molinari, "A modelling of cutting for viscoplastic materials," *International Journal of Mechanical Sciences,* vol. 39, no. 4, pp. 369-389, 1997.
[92] E. Budak and E. Ozlu, "Development of a thermomechanical cutting process model for machining process simulations," *CIRP annals,* vol. 57, no. 1, pp. 97-100, 2008.
[93] G. I. Taylor and H. Quinney, "The latent energy remaining in a metal after cold working," *Proceedings of the Royal Society of London. Series A, Containing Papers of a Mathematical and Physical Character,* vol. 143, no. 849, pp. 307-326, 1934.
[94] E. Ozlu, A. Molinari, and E. Budak, "Two-zone analytical contact model applied to orthogonal cutting," *Machining Science and Technology,* vol. 14, no. 3, pp. 323-343, 2010.
[95] S. Kato, K. Yamaguchi, and M. Yamada, "Stress distribution at the interface between tool and chip in machining," 1972.
[96] G. Barrow, W. Graham, T. Kurimoto, and Y. Leong, "Determination of rake face stress distribution in orthogonal machining," *International Journal of Machine Tool Design and Research,* vol. 22, no. 1, pp. 75-85, 1982.
[97] E. Cakir, E. Ozlu, M. Bakkal, and E. Budak, "Investigation of temperature distribution in orthogonal cutting through dual-zone contact model on the rake face," *The International Journal of Advanced Manufacturing Technology,* vol. 96, no. 1, pp. 81-89, 2018/04/01 2018.

[98] H. R. Orlande, M. N. Özişik, M. J. Colaço, and R. M. Cotta, *Finite difference methods in heat transfer*. CRC press, 2017.
[99] E. Budak and E. Ozlu, "Development of a thermomechanical cutting process model for machining process simulations," *CIRP Annals-Manufacturing Technology*, vol. 57, no. 1, pp. 97-100, 2008.
[100] E. Ozlu, "Analytical modeling of cutting process mechanics and dynamics for simulation of industrial machining operations," 2008.
[101] E. Özlü, E. Budak, and A. Molinari, "Thermomechanical modeling of orthogonal cutting including the effect of stick-slide regions on the rake face," 2007.